

Glass Transition and Dynamics of Suspended Charged Particles

Inaugural-Dissertation

zur Erlangung des Doktorgrades der
Mathematisch-Naturwissenschaftlichen Fakultät der
Heinrich-Heine-Universität Düsseldorf

vorgelegt von

Anoosheh Yazdi

aus Shahrood, Iran

Düsseldorf, August 2015

aus dem Institut für Theoretische Physik II: Weiche Materie
der Heinrich-Heine-Universität Düsseldorf

Gedruckt mit der Genehmigung der
Mathematisch-Naturwissenschaftlichen Fakultät der
Heinrich-Heine-Universität Düsseldorf

Referent: PD Dr. Alexei Ivlev
Korreferent: Prof. Dr. Hartmut Löwen

Tag der mündlichen Prüfung: 30.10.2015

Publications

- *Glass-transition properties of Yukawa potentials: From charged point particles to hard spheres*

Anoosheh Yazdi, Alexei Ivlev, Sergey Khrapak, Hubertus Thomas, Gregor E. Morfill, Hartmut Löwen, Adam Wysocki, and Matthias Sperl

Phys. Rev. E **89**, 063105 (2014)

The results in this paper are presented in *Chapter 2*.

- *Glass transition of charged particles in two-dimensional confinement*

Anoosheh Yazdi, Marco Heinen, Alexei Ivlev, Hartmut Löwen, and Matthias Sperl

Phys. Rev. E **91**, 052301 (2015)

The results in this paper are presented in *Chapter 3*.

Abstract

In this thesis we investigate the glass transition and dynamic properties of suspended mesoscopic charged particles in equilibrium and nonequilibrium conditions.

The glass transition curves of a single and double Yukawa potential model system in 3D are obtained using mode-coupling theory. In the potential parameters plane the glass transition curves are found to be parallel to the melting curves and follow similar analytical formulas. The glass transition properties of the Yukawa model system change between two limits; the one-component plasma and the hard sphere limit. It is shown that in the limit of one-component plasma the nonergodicity parameter approaches zero in the small wave number region with a quadratic behavior.

The glass transition of a two-dimensional confinement of charged particles is studied by mode-coupling theory considering two models of the interaction potentials; the Yukawa interaction, and the Kompaneets potential. The Yukawa interaction can model the system when the charged particles are levitating in an isotropic bath of ions. However it frequently occurs that in complex plasma, the charged particles are levitating atop an electrode which causes the ions to stream downwards. The downstream of the ions is focused by the charged particles attraction. This causes anisotropic distribution of the ions which gives rise to the Kompaneets potential interaction. We calculate and compare the mode coupling predictions for both systems in an experimentally relevant parameter region. It is shown that in the one-component plasma limit in 2D, the nonergodicity parameter approaches zero with a linear behavior in the small wave number regime.

Simulations have shown that the structure factor of a jammed state of monodisperse packing, approaches zero with a linear behavior. In contrast to the simulations, the liquid state theory predicts that the structure factor of the same system approaches a non-zero value with a quadratic behavior in the small wave number region for any value of the packing fraction. We use a long range potential γ/r^2 to successfully introduce the linear behavior of the structure factor observed in the simulation into the liquid state theory.

We consider a system in which energy is pumped into the Brownian particles causing negative values of friction. This can occur for example in complex plasma through the absorption of the ions by the dust particles. Starting from a Langevin equation with a Rayleigh type velocity dependent friction, the time evolution operators are developed which in case of noninteracting particles leads to a non-Gaussian velocity distribution. It is shown that for a constant effective temperature the higher the noise strength, the lower the probability of finding the active particle in the system. Using the Mori-Zwanzig formalism and the mode coupling approximation the equation of motion for the density auto-correlation function is derived. The integration through transients approach is used to derive a relation between the structure factor in the stationary state considering the interacting forces, and the conventional equilibrium static structure factor.

Zusammenfassung

In dieser Doktorarbeit untersuchen wir den Glasübergang und dynamische Eigenschaften suspendierter mesoskopischer geladener Teilchen sowohl unter Gleichgewichts- als auch unter Nichtgleichgewichtsbedingungen.

Die Glasübergangskurven sowohl für ein Single-Yukawa Potential als auch für ein Double-Yukawa Potential Modellsystem in drei Dimensionen werden mit Hilfe der Modenkopplungstheorie bestimmt. Es stellt sich heraus, dass die Glasübergangskurven innerhalb der Parameterebene parallel zu den jeweiligen Schmelzkurven liegen und ähnlichen analytischen Formeln folgen. Die Eigenschaften des Glasübergangs des Yukawa Modellsystems variieren zwischen zwei Grenzfällen: Dem Grenzfall des Einkomponenten-Plasmas und dem Grenzfall harter Kugeln. Es wird gezeigt, dass sich der Nicht-Ergodizitäts-Parameter im Grenzfall des Einkomponenten-Plasmas im Bereich kleiner Wellenzahlen quadratisch Null annähert.

Der Glasübergang eines auf zwei Dimensionen eingeschränkten Systems geladener Teilchen wird mit Hilfe der Modenkopplungstheorie unter Berücksichtigung zweier verschiedener Modelle des Wechselwirkungspotentials untersucht: Des Yukawa Potentials und des Kompaneets Potentials. Das Yukawa Potential eignet sich zur Modellierung eines Systems innerhalb eines isotropischen Ionenbades levitierter geladener Teilchen. Andererseits werden die geladenen Teilchen in komplexem Plasma häufig oberhalb einer Elektrode levitiert, was dazu führt, dass die Ionen abwärts strömen. Dieser abwärts gerichtete Ionenstrom wird dabei durch die Anziehung der geladenen Teilchen fokussiert, was zu einer anisotropen Verteilung der Ionen führt, die wiederum zu einem Kompaneets Wechselwirkungspotential führt. Wir berechnen und vergleichen die Voraussagen der Modenkopplungstheorie für beide Modelle innerhalb eines aus experimenteller Sicht relevanten Parameterbereiches. Es wird gezeigt, dass sich der Nicht-Ergodizitäts-Parameter im Grenzfall des Einkomponenten-Plasmas im Bereich kleiner Wellenzahlen linear Null annähert.

Simulationen haben gezeigt, dass der Strukturfaktor innerhalb eines monodispersen, dicht gepackten (jammed) Systems sich linear einem Wert von Null annähert. Im Gegensatz dazu sagt die Ornstein-Zernike Gleichung voraus, dass sich der Strukturfaktor desselben Systems für alle Packungsdichten im Bereich kleiner Wellenzahlen dem Wert von Null quadratisch annähert. Wir benutzen das langreichweitige Potential γ/r^2 , um das in Simulationen beobachtete lineare Verhalten des Strukturfaktors in analytischen Berechnungen erfolgreich zu reproduzieren.

Wir betrachten ein System Brownscher Teilchen, in das Energie so hineingepumpt wird, dass negative Reibungen auftreten. Diese können z.B. in komplexem Plasma durch die Absorption von Ionen durch Staubpartikel auftreten. Beginnend von einer Langevin Gleichung mit einer Rayleigh-artigen geschwindigkeitsabhängigen Reibung werden Zeitentwicklungsoperatoren hergeleitet, was im Falle nicht wechselwirkender Teilchen zur einer nicht-gaußschen Geschwindigkeitsverteilung führt. Es wird gezeigt, dass bei einer konstanten effektiven Temperatur die Wahrscheinlichkeit, ein aktives Teilchen im System aufzufinden umso geringer ist, je höher die Stärke des Rauschens ist. Mit Hilfe des Mori-Zwanzig Formalismus und der Modenkopplungsnäherung wird die Bewegungsgleichung für die Dichteautokorrelationsfunktion hergeleitet. Der Integration Through Transients (ITT) Ansatz wird benutzt um eine Relation zwischen dem Strukturfaktor im stationären Zustand unter

Berücksichtigung der Wechselwirkungskräfte einerseits sowie dem konventionellen statischen Strukturfaktor im Gleichgewicht andererseits herzuleiten.

Contents

1. Introduction	3
1.1. Glass Transition	3
1.2. Complex Plasma and Charged Colloids	4
1.3. Charged Particles in Confinement	5
1.4. Long Range Potentials and Jammed State Structure Factor	7
1.5. Non-Equilibrium Brownian Motion	8
1.6. Mode-Coupling Theory	9
1.7. Integration Through Transients	11
2. Glass Transition of Yukawa Systems in Three Dimensions	13
2.1. Yukawa Model	13
2.2. Methods	15
2.2.1. Mode-Coupling Glass Transition	15
2.2.2. Structure Factor	18
2.3. Results	20
2.3.1. Transition Curve	20
2.3.2. Glass Form Factors	23
2.3.3. Small q Behavior of the Glass Form Factor	26
2.3.4. Hard-Sphere Limit	30
2.3.5. Localization Length	31
2.4. Double Yukawa Potential	35
2.4.1. Glass Transition	35
2.4.2. Localization Length	37
3. Glass Transition of Charged Particles in Two-Dimensional Confinement	41
3.1. Yukawa Monolayer	41
3.2. Kompaneets Monolayer	42
3.3. Structure Factor and Mode-Coupling Theory	47
3.4. Results	51
3.4.1. Glass Transition Diagrams	51
3.4.2. Potentials and Structure Factors at the Transitions	54

3.4.3. A Fallacious Re-entrant State Sequence	56
3.4.4. Nonergodicity Parameters	58
4. Modification of a Liquid State Structure Factor to Create a Jammed State Structure Factor	64
4.1. Small Wave Number Dependence of the Structure Factors of the Long Range $1/r^n$ Potentials	65
4.2. The Effects of an Additional $1/r^2$ Potential	67
4.3. A Random Phase Approximation	69
4.4. Conclusion and Outlook	73
5. Dynamics of Brownian Particles with Velocity-Dependent Friction	75
5.1. Nonlinear Langevin Equation	75
5.2. Time Evolution Operators	76
5.3. Distribution Function	78
5.3.1. Rayleigh-Type Model of Friction	79
5.3.2. Distribution Function and Effective Temperature in Case of Rayleigh-Type Model of Friction	80
5.3.3. Probability of Finding Particles with Negative Friction (Active Particles)	84
5.4. Definition of the Averages	86
5.5. Mori-Zwanzig Formalism	88
5.6. Mode-Coupling Approximation	92
5.7. Equation of Motion for Density Auto-Correlation Function	96
5.8. Kernel Projection on Density-Current and Current-Current Pairs	99
5.9. Integration Through Transients (ITT)	104
6. Summary and Conclusion	108
A. Derivation of the Yukawa Potential	111
B. Fourier Transform Integral of $1/r^{n-\epsilon}$ in 3D	113
C. Normalization Constant and Different Moments of the Velocity Distribution	114
D. Ω_{22} for Normal Brownian Motion	116
E. Mori-Zwanzig Formalism	118
Bibliography	127

Chapter 1

Introduction

1.1. Glass Transition

By cooling a liquid sufficiently fast, it is possible to avoid crystallization [1]. When the temperature of the undercooled liquid reaches the glass transition temperature T_g , it behaves like a solid material on the experimental time scale. At T_g , the shear viscosity of the system reaches 10^{13} Poise and the relaxation time (the time needed for a system to reach an equilibrium condition after a disturbance) becomes of the order of 100 seconds. When $T \leq T_g$, the resulting material is called a glass. Although a complete definition of the glass does not exist yet, this experimental definition is widely used. The value of T_g depends on the cooling rate [2], however its dependence on the cooling rate is small. When the temperature is near T_g , dramatic changes happen in the enthalpy, viscosity [3] and the relaxation time of the liquid. The dynamic behavior slows down near T_g and basically the system crosses over to an arrested state, even though the structural changes are smooth. The temperature range within which these changes happens, is a small range therefore the term transition is used. Whether the glass transition is a purely dynamical transition or it has thermodynamical origins is still a matter of debate.

Different theories have been developed to explain the glassy systems and their dynamical properties. Some of these are the energy landscape picture [3, 4], mode coupling theory [5, 6] and random first order transition theory [7, 8]. Many literature reviews investigate the strength and weaknesses of the theories of the glass transition [9–11].

Mode coupling theory (MCT) results in an ideal glass transition, which in contrast

to observation, is independent of cooling rate and does not depend on the experimental time scale. The MCT glass transition temperature is at $T_c > T_g$. Mode coupling theory predicts rather accurately the two step relaxations in the scattering function or so called β and α -relaxations. These relaxations consist of two power law decays and an stretched exponential decay which can be fitted by a Kohlrausch function. The Kohlrausch function which is also called the stretched exponential, can be written as $F = A \exp(-(t/\tau)^\beta)$ [6]. The consistency of the scattering functions with experiments and simulations has been demonstrated [12–14].

1.2. Complex Plasma and Charged Colloids

Complex plasma consists of charged microparticles (dusts) embedded in a weakly ionized gas (plasma). The dust particles collect their charge from the surrounding plasma. Because the electron thermal velocity is much larger than the ion's thermal velocity, the flux (flow rate per unit area) of the electrons on the surface of the dust particles, is much larger than the flux of the ions. Therefore the amount of negative charges on the dust particles is larger than the positive ones which causes the dust particles to have negative charge [15]. The dust particles are of the size of one micron and are individually traceable optically. This is a reason that complex plasma can be used as a model system.

Charged colloids or charged stabilized suspensions consist of highly charged mesoscopic particles suspended in a liquid solvent. The microscopic counterions exist as a part of solvent [16]. The difference between ionic liquids such as a molten salt and charged colloids is that in the ionic liquids the cations and the anions have comparable sizes, however in charged colloids the macroions are mesoscopic while the counterions are of microscopic size [17]. Despite their differences both charged colloids and the ionic liquids can be treated by liquid state theory, since in general the phase behavior of colloids is very much similar to atomic systems [18].

Both complex plasma and charged colloids can be used as a model systems to study the dynamics of liquids. What makes charged colloids and complex plasma different is the surrounding fluid, which is a liquid in case of colloids and a gas in case of dusty plasma. The surrounding fluid being much denser in colloids makes the interaction ranges much shorter. In charged colloids the interaction range is usually comparable to the particle sizes. Therefore, charged colloids usually are modeled by a hard sphere potential which models the excluded volume of the particle, plus a tail which

describes the charge interactions. In complex plasma, the interaction range is much larger than the particle sizes hence an approximation of pointlike particles is valid. Another effect which a surrounding fluid has is the friction force which it imposes on the particles. Since in colloids the surrounding fluid is denser, the damping time scale is much shorter. The dynamics of colloids is basically considered as overdamped. The damping time scale of the complex plasma is larger than colloids, therefore the motion is considered Brownian on much larger time scales [15]. The accessibility of the undamped short time regime in complex plasma allows better modeling of the different dynamic regimes of conventional liquids [15]. The repulsive screened Coulomb (Yukawa) potential is the potential which is used to model the interactions in both complex plasma and colloids. While in charged colloids the hard core plus a Yukawa tail is mostly considered [19], in complex plasma the Yukawa potential between point particles is more relevant. Investigating the behavior and dynamics of the mesoscopic particles usually is done in a coarse grained way which means the effect of the surrounding fluid only enters the calculation through the effect it has on the interactions between the mesoscopic particles.

Mode-coupling theory has been also used to investigate the glass transition of binary charged hard sphere systems [20, 21], and charged hard spheres in front of a homogeneous neutralizing background [22, 23]. They have found a glassy state at low densities due to long range Coulomb interactions. They found that there exist two sorts of glassy states in the charged hard sphere system, one originating from the hard core potential which is the excluded volume effect and happens at high densities; the other one, originating from the Coulomb potential at low densities.

In chapter 2, we use mode coupling theory to investigate the glass transition properties of a Yukawa model system which consists of point particles in three dimensions interacting via Yukawa pair interactions. We also discuss the effect of the long range interactions on the small wave number region of the nonergodicity parameters. Since the long time dynamics and glass transition properties are the same for both Newtonian and Brownian dynamics [24], the calculations are applicable to both complex plasma and charged colloids.

1.3. Charged Particles in Confinement

A two dimensional configuration of charged particles can be observed in many cases e.g. colloidal particles confined between two plates [25, 26] or in complex plasma

when dust particles levitate above and parallel to the electrode [27].

In complex plasma, the Yukawa interaction model has been used widely to describe the interaction between particles [15, 28, 29]. The Yukawa interaction can describe the effective pair-potential between charged particles rather accurately around the mean interparticle distance [30, 31]. It is the isotropic Boltzmann distribution of electron and ions which give rise to the Yukawa model in two dimensions. However in laboratory experiments of charged particles in two dimensional confinement, the distribution of ions is anisotropic in three dimensions. Therefore, the Yukawa model is not justified. In the common case of dusty plasma experiments in a radio frequency chamber, the dust particles levitate as a two dimensional surface formed above the electrode in the sheath region [29]. In that region because of the large value of the electric field, the distribution of the ions is highly anisotropic. The ions are attracted by the electrode and form a current downwards which is focused due the attraction between the dust particles and the ions and forms a cone like shape. A kinetic theory of the ion distributions and effective dust grain interactions is appropriate in this case, and has been studied by different groups of researchers, under different assumptions for the plasma parameters [31–39]. The theory is based on the solution of the kinetic equation for the distribution of ions moving in the electrostatic field in the sheath region. In the kinetic equation, the ion collision operator describes the collision between the ions and the neutral particles in the plasma. According to different experimental parameters, such as radio frequency discharge power and pressure, different approximations are used for building the ion collision operator.

Among these kinetic models, the one published by Kompaneets *et al.* [31] is based on a reasonable assumption of a mobility-limited ion drift in the sheath field, as opposed to rather unrealistic inertia-limited motion [28]. The resulting three-parametric potential from the Kompaneets model is anisotropic in three dimensions (3D). For charged particles confined to 2D, it exhibits an algebraically long-ranged r^{-3} in-plane decay. This model is expected to provide a realistic description of interactions in ground-based dusty plasma laboratory experiments [40].

The dimensional dependence of the mode-coupling theory has been discussed in Ref. [41]. They have shown that the $d = 2$ results are qualitatively in agreement with simulations. Lang *et al.* [42–44] have developed the mode-coupling theory of glass transition and glassy dynamics in planar confinements (quasi two dimensional case). Planar is the confinement between two parallel walls with narrow separation. They have shown that the MCT of the planar confinement converges to the two

dimensional MCT for small separations of the walls.

In chapter 3 we use the two dimensional mode coupling theory [41] to acquire the glass transition points of dust particles in a two dimensional layer, interacting via the Yukawa potential. We also calculate the transition points for a 2D layer of dust particles interacting via the Kompaneets potential. We obtain qualitatively similar liquid-glass transition curves for monolayers with Yukawa-like and Kompaneets-like pair potentials. We find that the glass transition in a 2D complex plasma experiment will show a re-entrant liquid-glass-liquid state sequence if one decides to assume a Yukawa like potential between the particles. But this apparent re-entrant phenomenon is an artifact which arises as a result of trying to describe the interaction by a Yukawa potential which best fits the Kompaneets potential in the distance range around the mean geometrical distance. When one assumes the more realistic Kompaneets potential this re-entrant sequence disappears. In the end, we compare the nonergodicity parameter of the Yukawa and Kompaneets monolayer.

1.4. Long Range Potentials and Jammed State Structure Factor

In the packing of identical particles in the vicinity of the jammed state, the structure factor behaves differently than what the conventional liquid state theory predicts (by liquid state theory we mean different closures and approximations [17] which exists for solving the Ornstein-Zernike Integral equation to obtain the structure factor). It was shown by simulations which contain a large number of particles, that in the nearly jammed states with hard sphere interactions [45], repulsive short range harmonic potential interactions [46], or other more realistic potential interactions [47, 48], the structure factor displays a linear behavior at the small wave numbers and approaches a very small number or possibly zero. The fact that in the jammed state the structure factor behaves like $S(k) \propto k$, has been termed hyperuniformity [47]. This is different from what is obtained using the conventional ways of calculating the structure factor in liquid state theories. For short range potentials, such as hard or harmonic soft spheres, the liquid state theory predicts a structure factor with the behavior $S(k) \simeq S(0) + \alpha k^2$ at small wave number k . The finite intercept $S(0)$, represents a finite compressibility in the system. From liquid state theories point of view, the structure factor behaves the same in liquid all the way to the glassy or jammed state. This is in contrast to the simulations which suggest that linear

behavior at small wave numbers emerges at the packing fractions in the vicinity of the jamming. It is argued by Nixon *et al.* [49], that the linear behavior in the structure factor is equivalent to the total correlation function $h(r) \propto r^{-4}$ where $h(r) = g(r) - 1$. Also, liquid state theories predict an structure factor which although has a behavior $\propto k^2$ at $k \rightarrow 0$, it approaches zero for the very long range Coulomb potential. This may arise the thought that it can be possible to reproduce the jammed state structure factor, using a long range potential inside the frame work of the liquid state theories.

In chapter 4, we use a long range potential, to modify the structure factor acquired from hypernetted chain closure [17] to create a jammed state structure factor. We show that introducing an additional long range potential $\propto r^{-2}$ to the harmonic short range potential can produce the linear behavior in the structure factor inside the frame work of the liquid state theories.

1.5. Non-Equilibrium Brownian Motion

Brownian motion can be described by a Langevin equation [50, 51], where it is considered that the gain of energy by stochastic forces is compensated by the energy loss because of dissipation (due to a positive friction). In the usual case of Brownian motion, the fluctuation-dissipation theory holds and the motion of the Brownian particle is actually passive. Positive friction describes a passive motion. In complex plasma the dust particles can absorb the ions due to the electrostatic forces. The absorption of the ions by the dust particles in a specific parameter regime can cause unbalanced momentum transfer to the dust grains. In a two dimensional Coulomb plasma this can be described by a negative friction coefficient for slow dust particles [52]. Negative friction means pumping of the energy to the Brownian particles. This behavior is also visible in active or self propelled particles. The collective behavior and dynamics of the active particles, be it bacteria, cells or complex plasma, in the dense regime can be a matter of interest [53, 54]. One way to account for an internal propulsion mechanism which pump some energy into the Brownian particle, is to introduce a velocity dependent friction into the Langevin equation [55]. It is shown by theoretical arguments that dense active systems can probably undergo a glass transition [56].

Farage and Brader [57], recently studied the glass transition of active particles in the framework of the mode coupling theory. They started from the Smoluchowski

equation considering the rotational diffusion and the coupling between rotational and translational motion. They have approximated, a single particle motion subjected only to rotational diffusion and self propulsion, by a random walk motion. They found that the glass transition will be shifted towards higher packing fractions by increasing the activity. Glassy dynamics of active particles is also studied by Szamel *et al.* [58] within MCT. They start from the Ornstein-Uhlenbeck process, modeling the self propulsion as an internal driving force and they find that by increasing activity the long time dynamics first accelerates and then slows down. They obtain the steady state correlations from simulation.

In chapter 5, we study the mode coupling equations for the case of velocity dependent friction. We start from the according nonlinear Langevin equation. A Rayleigh type equation is used to model the velocity dependent friction. The solution of the corresponding Fokker-Planck equation for non-interacting particles is used as the velocity steady state distribution function. The total distribution function is assumed as the multiplication of the velocity distribution and the Gaussian position distribution. We use the Liouville operators and the mode coupling approximations to obtain the equation of motions.

1.6. Mode-Coupling Theory

Mode coupling theory provides a time evolution equation for the density auto-correlation function. The density auto-correlation function can be written as

$$\phi_q(t) = \frac{\langle \rho_q^*(t) \rho_q \rangle}{NS_q}, \quad (1.1)$$

where S_q is the static structure factor, $\rho_q = \sum_k \exp(i\mathbf{q} \cdot \mathbf{r}_k)$ is the Fourier transform of the density $\rho(\mathbf{r}) = \sum_k \delta(\mathbf{r} - \mathbf{r}_k)$, and the brackets are the canonical averages. The canonical average for a phase variable A is defined as $\langle A(\mathbf{\Gamma}) \rangle = \int f(\mathbf{\Gamma}) A(\mathbf{\Gamma}) d\mathbf{\Gamma}$, where f is the distribution function and $\mathbf{\Gamma}$ is the set of phase space coordinates. At time zero, $\langle \rho_q^*(t=0) \rho_q \rangle$ is equal to NS_q , where N is the number of particles.

The density ρ_q is coupled with the Fourier transformed density current $\mathbf{j}_q = \sum_k \mathbf{v}_k \exp(i\mathbf{q} \cdot \mathbf{r}_k)$, through the continuity equation

$$\frac{d\rho_q}{dt} = i\mathbf{q} \cdot \mathbf{j}_q. \quad (1.2)$$

The continuity equation is a time evolution equation for the dynamical variable ρ_q . In general one can calculate the time evolution operator for all the dynamical variables of a specific system using Liouville operators [59]. The Mori-Zwanzig projection formalism [60, 61] is applied to the two dynamical variables ρ_q and the longitudinal current j_q^L , which is the \mathbf{j}_q element in the direction of the \mathbf{q} , to separate the fluctuating forces. The resulting equation for the density auto-correlation function is written as

$$\partial_t^2 \phi_q(t) + \Omega_q^2 \phi_q(t) + \int_0^t \partial_{t'} \phi_q(t') M_q(t-t') dt' = 0, \quad (1.3)$$

where $\Omega_q^2 = q^2 k_B T / S_q$. The expression $M_q(t)$ is called memory kernel. M_q is again projected on the product $\rho_k \rho_p$ where the first mode coupling approximation is used to produce the kernel $M_q^{\text{mct}} = \Omega_q^2 m_q^{\text{mct}}$. $M_q(t)$ is approximated to consist of a white noise term plus M_q^{mct} , thus $M_q(t) = \nu_q \delta(t) + \Omega_q^2 m_q^{\text{mct}}(t)$. Therefore Eq. (1.3) is written as

$$\partial_t^2 \phi_q(t) + \nu_q \partial_t \phi_q(t) + \Omega_q^2 \phi_q(t) + \Omega_q^2 \int_0^t \partial_{t'} \phi_q(t') m_q^{\text{mct}}(t-t') dt' = 0. \quad (1.4)$$

where m_q^{mct} is the MCT kernel

$$m_q^{\text{mct}}(t) = \mathcal{F}_q(\phi(t)). \quad (1.5)$$

The equation (1.4) can be solved using the initial condition $\phi_q(0) = 1$ and $\partial_t \phi_q(0) = 0$. The solution of the equation is a correlation function with the value between 1 and zero. The long time limit of the density auto-correlation function, $\lim_{t \rightarrow \infty} \phi_q(t) = f_q$, is called the glass form factor or the nonergodicity parameter. If the density correlation function stays non-zero in the long time limit $f_q > 0$, the dynamic is arrested and glassy. If eventually $f_q = 0$, the state is still liquid. From Eq. (1.4), (1.5) and $\lim_{t \rightarrow \infty} \phi_q(t) = f_q$ one has

$$f_q + \lim_{t \rightarrow \infty} \int_0^t \partial_{t'} \phi_q(t') \mathcal{F}_q(\phi(t-t')) dt' = 0, \quad (1.6)$$

and therefore

$$f_q + \mathcal{F}_q(f) [f_q - 1] = 0. \quad (1.7)$$

This is the equation which can be solved to obtain the glass transition temperature T_c or, in case of the hard sphere system, the glass transition packing fraction φ_c .

The mode coupling theory can also be applied to colloids where the motion is Brownian and overdamped. In that case, Eq. (1.4) turns into

$$\tau_q \partial_t \phi_q(t) + \phi_q(t) + \int_0^t \partial_\nu \phi_q(t') m_q^{\text{mct}}(t-t') dt' = 0. \quad (1.8)$$

Here the fluctuation dissipation relation $D_0 = k_B T / \nu_q$, is used. D_0 is the diffusion coefficient and $\tau_q = S_q / D_0 q^2$. When $m_q^{\text{mct}}(t) = 0$, one obtains $\phi_q(t) = \exp(-t/\tau_q)$. This means the auto-correlation function has an exponential decay like in a normal liquid above the melting temperature T_m . It was shown by Fuchs [62] and Szamel *et al.* [24], that the asymptotic prediction of MCT do not change for Brownian dynamics. MCT predicts the same transition temperature for molecular dynamics described by Eq. (1.4) and Brownian dynamics. It is also shown by simulation that apart from β relaxation the long time α relaxation of the correlation function and the form factor is the same for both Newtonian and Brownian dynamics [63].

Mode coupling equations are also developed for a tagged particle motion quite similar to the collective equations with a differently formulated MCT kernel [5, 6].

Later Fuchs and Cates have developed a mode-coupling approach to explore the nonlinear rheology of colloidal fluids and glasses under steady shear [64, 65]. It has been found in [65] that shear advection of density fluctuations accelerates the loss of memory. Chong and Kim developed a non-equilibrium mode-coupling theory for a uniformly sheared system [66] starting from thermostated Sllod equations [59]. The time dependent distribution function is calculated using the Liouville operator based on the Sllod equations. Later Suzuki and Hayakawa [67] used the same starting point, applied an isothermal condition, and resolved the contradiction between [65] and [66]. Kranz *et al.* [68, 69] have developed a mode-coupling approach for granular fluid (dissipative hard spheres) starting from a Liouville operator containing collision and driving terms. They find that with increasing dissipation, the glass transition shifts to higher densities.

1.7. Integration Through Transients

As we mentioned, a mode-coupling approach is developed by Fuchs and Cates to explore the nonlinear rheology of colloidal fluids and glasses under steady shear

[64, 65]. The starting point is the Smoluchowski equation

$$\begin{aligned}\partial_t \Psi &= \Omega \Psi, \\ \Omega &= \sum_i \boldsymbol{\partial}_i \cdot (\boldsymbol{\partial}_i - \mathbf{F}_i - \boldsymbol{\kappa} \mathbf{r}_i)\end{aligned}\quad (1.9)$$

which is an equation for the time evolution of the distribution function Ψ . The Smoluchowski operator only involves the position coordinates of the Brownian particles since on the Smoluchowski time scale the momentum coordinates already have relaxed to equilibrium. The $\boldsymbol{\kappa}$ is the shear rate tensor $\kappa_{ij} = \dot{\gamma} \delta_{ix} \delta_{iy}$ and $\dot{\gamma}$ is the shear rate. The vanishing shear rate $\dot{\gamma} = 0$, corresponds to the equilibrium state where $\Omega_e \Psi_e = 0$. At time $t = 0$, a constant shear rate $\dot{\gamma}$ is switched on. Therefore, the time dependence of the Smoluchowski operator can be written as

$$\Omega(\Gamma, t) = \begin{cases} \Omega_e(\Gamma) = \sum_i \boldsymbol{\partial}_i \cdot (\boldsymbol{\partial}_i - \mathbf{F}_i), & t \leq 0 \\ \Omega(\Gamma) = \sum_i \boldsymbol{\partial}_i \cdot (\boldsymbol{\partial}_i - \mathbf{F}_i - \boldsymbol{\kappa} \mathbf{r}_i). & t > 0 \end{cases}\quad (1.10)$$

When $t \geq 0$, $\Psi(\Gamma, t) = \exp(\Omega(\Gamma)t) \Psi_e(\Gamma)$ where $\exp(\Omega(\Gamma)t) = 1 + \int_0^t dt' \exp(\Omega(\Gamma)t') \Omega$. For $t \rightarrow \infty$ the distribution converges to the stationary distribution $\Psi_s(\Gamma)$. Therefore

$$\Psi_s(\Gamma) = \Psi_e(\Gamma) + \int_0^\infty dt e^{\Omega t} \Omega \Psi_e(\Gamma).\quad (1.11)$$

Using Eq. (1.11), the stationary state average of an arbitrary function $A(\Gamma)$ can be written as

$$\int d\Gamma \Psi_s(\Gamma) A(\Gamma) = \int d\Gamma \Psi_e(\Gamma) A(\Gamma) + \int_0^\infty dt \int d\Gamma A(\Gamma) e^{\Omega t} \Omega \Psi_e(\Gamma).\quad (1.12)$$

This mechanism called integration through transients (ITT) is used by Fuchs and Cates [65] to obtain the stationary state correlation functions. The point of using ITT is that the stationary state distribution Ψ_s cannot be obtained directly from solving the Smoluchowski equation. In section 5.9 we use ITT to obtain a relation between the static structure factor in non-equilibrium condition and the conventional equilibrium structure factor.

Chapter 2

Glass Transition of Yukawa Systems in Three Dimensions

This chapter follows the publication Yazdi *et al.* [70].

2.1. Yukawa Model

If a point like negatively charged particle, is immersed in an ionized background consisting of electrons and ions, the potential around the particle can be written as screened Coulomb (Yukawa) potential [71]

$$\phi(r) = \frac{Q}{4\pi\epsilon r} \exp\left(-\frac{r}{\lambda}\right), \quad (2.1)$$

where r is the distance from the particle, ϵ is the permittivity of the medium and λ is the screening length. The screening is due the fact that ions and electrons shield the test charge potential which reduces the potential around the test charge with the decay constant $1/\lambda$. The Yukawa potential is derived solving the Poisson equation when assuming Boltzmann distribution of ions and electrons [72, 73], for the derivation, see Appendix A.

Considering N , the number of charged particles instead of one test charge, the interest is focused on the pair interaction potential energy of the particles. Thus we multiply the $\phi(r)$ in Eq. (2.1) by Q and make it dimensionless by dividing it by $k_B T$. We also make the distance dimensionless by dividing r by the mean interparticle distance. The mean interparticle distance in three dimensions is $1/\sqrt{n^3}$ where n is

the number density of the particles. Therefore the Yukawa interparticle potential energy is written as

$$\frac{U(x)}{k_{\text{B}}T} = \frac{\Gamma}{x} \exp(-\kappa x), \quad (2.2)$$

where x is the distance in the unit of average interparticle distance, $x = r\sqrt[3]{n}$. The Yukawa potential can be characterized by two parameters κ and Γ . $\kappa = 1/(\lambda\sqrt[3]{n})$ is the inverse of the screening length λ in the unit of average interparticle distance. The coupling parameter or interaction strength is $\Gamma = Q^2\sqrt[3]{n}/(4\pi\epsilon k_{\text{B}}T)$. In this chapter whenever we refer to the Yukawa potential (energy) we mean Eq. (2.2).

In a system of particles interacting via the Yukawa potential, when the potential energy dominates the kinetic energy of particles ($\Gamma \gtrsim 1$), the system is called strongly coupled and therefore the main research interest is shifted from the gas phase to the statistical mechanics of the liquid and solid state [15, 74]. The Yukawa potential has been used to model charged colloids [75, 76] and the complex plasma [15]. In colloids usually one consider a hard-sphere potential and a Yukawa potential outside the hard core [77]. Unlike typically in colloids, the interaction range and the mean interparticle distances in complex plasma are much larger than the particle sizes, hence an approximation of point-like particles is appropriate. We also consider the vacuum permittivity $\epsilon = \epsilon_0$ since in complex plasma this is usually the case. In the limit of vanishing screening parameter, $\kappa = 0$, one recovers the one-component-plasma (OCP), which is the simplest model that exhibits characteristics of charged systems [17]. In this limit, the Yukawa potential tends to the Coulombic pair interactions

$$\frac{U(x)}{k_{\text{B}}T} = \frac{\Gamma}{x}. \quad (2.3)$$

We consider a model system of point particles in three dimensions interacting with Yukawa potential (Eq. (2.2)). We use mode coupling theory [6], to investigate the glass transition properties of the Yukawa model system.

2.2. Methods

2.2.1. Mode-Coupling Glass Transition

Within MCT the glass transition is defined via the nonergodicity parameter f_q , which is the long time limit of the density autocorrelation function $\phi_q(t)$

$$f_q = \lim_{t \rightarrow \infty} \phi_q(t). \quad (2.4)$$

Inside the liquid $\phi_q(t)$ decays to zero resulting in vanishing f_q . On the other hand in the glassy state the density auto-correlation function remains finite therefore $f_q > 0$ [5, 6]. It is also common to name the f_q the glass form factor or Debye-Waller factor. The nonergodicity parameter is a solution of the equation

$$\frac{f_q}{1 - f_q} = \mathcal{F}_q(f), \quad (2.5)$$

where \mathcal{F}_q is the memory kernel. In a hard-sphere system (HSS) in three dimensions the memory kernel can be written as [5, 41]

$$\begin{aligned} \mathcal{F}_{q'}^{\text{HSS}}(f) &= \frac{nS_{q'}}{32\pi^2 q'^5} \int_0^\infty dk' \int_{|k'-q'|}^{k'+q'} dp' k' p' S_{p'} S_{k'} \\ &\times [c_{k'}(q'^2 + k'^2 - p'^2) + c_p(q'^2 - k'^2 + p'^2)]^2 f_{k'} f_{p'}. \end{aligned} \quad (2.6)$$

Here we used the prime symbol to differentiate between the hard sphere and the Yukawa case which we explain later. $S_{q'}$ is the static structure factor which is related to the Fourier transformed direct correlation function $c_{q'}$, via $S_{q'} = 1/(1 - nc_{q'})$. Thus the only input to the Eq. (2.5) is the static structure factor. In the hard-sphere system the dimension of the wave number q' , is the inverse length $[q'] = L^{-1}$. Also $[S_{q'}] = 1$, $[c_{q'}] = L^3$ and $[f_{q'}] = 1$. Therefore the dimension of $\mathcal{F}_{q'}^{\text{HSS}}$ is given as

$$[\mathcal{F}_{q'}^{\text{HSS}}] = [n]L^3 = 1. \quad (2.7)$$

This means that, $\mathcal{F}_{q'}^{\text{HSS}}$ is a dimensionless quantity. In our Yukawa model system, we have defined the distance in the unit of a length scale $1/\sqrt[3]{n}$, thus the dimension of wave number is

$$[q] = \frac{1}{L[\sqrt[3]{n}]} = 1. \quad (2.8)$$

The memory kernel can be written as

$$\begin{aligned} \mathcal{F}_q(f) &= \frac{S_q}{32\pi^2 q^5} \int_0^\infty dk \int_{|k-q|}^{k+q} dp kp S_p S_k \\ &\times [c_k(q^2 + k^2 - p^2) + c_p(q^2 - k^2 + p^2)]^2 f_k f_p, \end{aligned} \quad (2.9)$$

which is different from Eq. (2.6) by the fact that the number density does not appear explicitly behind the integrals. Here $S_q = 1/(1 - c_q)$ and $[c_q] = 1$, $[S_q] = 1$, $[f_q] = 1$ therefore $[\mathcal{F}_q] = 1$. The closed form of the memory kernel is

$$\mathcal{F}_q(f) = \frac{1}{16\pi^3} \int d^3k \frac{S_q S_k S_p}{q^4} (\mathbf{q} \cdot \mathbf{k} c_k + \mathbf{q} \cdot \mathbf{p} c_p)^2 f_k f_p, \quad (2.10)$$

where $\mathbf{p} = \mathbf{q} - \mathbf{k}$. One can discretize Eq. (2.9), on a equidistant grid using the middle point Riemann sum. We choose to do the discretization over 100 points with the step size $\Delta = 0.4$. $q = \Delta \hat{q}$, $k = \Delta \hat{k}$ and $p = \Delta \hat{p}$ where $\hat{q}, \hat{k}, \hat{p} = 1/2, 3/2, 5/2, \dots, 199/2$. The minimum value of $q, k, p_{\min} = 0.2$ and the cut off value $q, k, p_{\max} = 39.8$ [78], therefore

$$\mathcal{F}_q(f) = \frac{S_q \Delta^3}{32\pi^2 \hat{q}^5} \sum_{\hat{k}, \hat{p}} S_k S_p [c_k(\hat{q}^2 + \hat{k}^2 - \hat{p}^2) + c_p(\hat{q}^2 - \hat{k}^2 + \hat{p}^2)]^2 f_k f_p. \quad (2.11)$$

Here the sum over \hat{p} has the restriction that $|\hat{q} - \hat{k}| + 1/2 \leq \hat{p} \leq \hat{q} + \hat{k} + 1/2$ due to the integral limits in Eq. (2.9). Later we will use the same discretization to discretize Eq. (2.19). Using the discretized kernel in Eq. (2.11) we can solve Eq. (2.5) to obtain the glass transition point and the non-ergodicity parameter at the transition. Eq. (2.5) can be solved iteratively [78]

$$f_q^{(n+1)} / (1 - f_q^{(n+1)}) = \mathcal{F}_q(f^{(n)}), \quad (2.12)$$

starting from $f_q^{(0)} = 1$. This means we feed $f_q^{(0)} = 1$ to the discretized kernel in Eq. (2.11) and obtain the $\mathcal{F}_q^{(0)}$. From $\mathcal{F}_q^{(0)}$ we calculate the $f_q^{(1)}$ through Eq. (2.12) and use it as an input to the discretized kernel again. We continue this procedure until $|f_{q=3.8}^{(n+1)} - f_{q=3.8}^{(n)}| < \epsilon$, with $\epsilon = 10^{-9}$. The value $q = 3.8$ is just an arbitrary grid point, and in principle the f_q converges for all arbitrary chosen grid points values smaller than the q cutoff. The only inputs to the kernel which depend on our potential are S_q and c_q . Depending on which structure factor we feed to the discretized kernel, the f_q which we obtain from the iteration process can be zero, showing us that we have liquid, or $f_q > 0$ showing us that we have a glassy state. For calculating the discretized memory kernel we reduce the computational effort

by using the Bengtzelius trick explained in [79].

One other quantity which we will calculate is the localization length r_s^c . It is defined as

$$r_s^c{}^2 = \lim_{t \rightarrow \infty} \frac{\delta r^2(t)}{6}, \quad (2.13)$$

where $\delta r^2(t)$ is the mean squared displacement. At the transition density or temperature a tagged particle will be able to move a distance equal to the localization length before it is hindered by its neighboring particles. The localization length can also be obtained using the relation [80]

$$r_s^c{}^2 = \frac{1}{\mathcal{F}_{MSD}(f, f^s)}, \quad (2.14)$$

where f_s is the Lamb-Mössbauer factor $f_q^s = \lim_{t \rightarrow \infty} \phi_q^s(t)$, the long-time limit of the tagged particle autocorrelation function $\phi_q^s(t)$, and [80]

$$\mathcal{F}_{MSD} = \frac{1}{6\pi^2} \int_0^\infty S_q c_q^{s2} q^4 f_q f_q^s dq. \quad (2.15)$$

In this equation again the number density n is canceled out since the dimension of the wave number $[q]$ is one and also $[c_q^s] = 1$. Since the tagged particle is one of the liquid particles $c_q^s = c_q$. One can discretize Eq. (2.15) as

$$\mathcal{F}_{MSD} = \frac{\Delta^5}{6\pi^2} \sum_{\hat{q}} S_q c_q^{s2} \hat{q}^4 f_q f_q^s, \quad (2.16)$$

again we used the middle point Riemann sum with 100 points where the step size $\Delta = 0.4$, $q = \Delta \hat{q}$ and $\hat{q} = 1/2, 3/2, 5/2, \dots, 199/2$. $q_{\min} = 0.2$ and the cut off value $q_{\max} = 39.8$.

The Lamb-Mössbauer factor f_q^s is calculated in MCT according to [80]

$$\frac{f_q^s}{1 - f_q^s} = \mathcal{F}_q^s[f, f^s], \quad (2.17)$$

where $\mathcal{F}_q^s[f, f^s]$ is the tagged particle memory kernel which is written as

$$\mathcal{F}_q^s[f, f^s] = \frac{1}{8\pi^2 q^4} \int d^3k S_k(\mathbf{q} \cdot \mathbf{k})^2 c_k^2 f_k f_p^s \quad (2.18)$$

or equivalently in bipolar coordinates

$$\mathcal{F}_q^s[f, f^s] = \frac{1}{16\pi^2 q^5} \int_0^\infty dk \int_{|k-q|}^{k+q} dp \, kp \, S_k [c_k^s(q^2 + k^2 - p^2)]^2 f_k f_p^s. \quad (2.19)$$

This, using the same grid as in Eq. (2.11), \mathcal{F}_q^s can be discretized as

$$\mathcal{F}_q^s = \frac{\Delta^3}{16\pi^2 \hat{q}^5} \sum_{\hat{k}, \hat{p}} \hat{k} \hat{p} \, S_k [c_k^s(\hat{q}^2 + \hat{k}^2 - \hat{p}^2)]^2 f_k f_p^s. \quad (2.20)$$

Eq. (2.17) is solved iteratively starting from $f_p^{s(0)} = 1$ via $f_q^{s(n+1)}/(1 - f_q^{s(n+1)}) = \mathcal{F}_q^s[f, f^{s(n)}]$. The iteration process is the same as we explained for f_q in Eq. (2.12). In the tagged particle discretized kernel we need to input the f_q which we have calculated from Eq. (2.12) therefore when $f_q = 0$ we have $f_q^s = 0$.

2.2.2. Structure Factor

As we can observe in Eq. (2.9) and (2.19) the input to the MCT equations are the structure factor S_q and the Fourier transformed direct correlation functions c_q . These two functions are related via the Ornstein-Zernike equation

$$\gamma_q = \frac{c_q^2}{1 - c_q}, \quad (2.21)$$

where the spatial Fourier transform of γ_q is $\gamma(x) = h(x) - c(x)$ and $h(x)$ is the total correlation function. The Fourier transform of the total correlation function, h_q , is related to the structure factor through $S_q = 1 + h_q$. The Ornstein-Zernike equation is not solvable by itself and we need to choose a closure for the equation. It was found earlier that the hypernetted chain closure (HNC) approximation captures various structural features for repulsive potentials, especially also for the OCP (one-component plasma)[81]. Therefore the HNC closure is used

$$c(x) = \exp[-U(x)/(k_B T) + \gamma(x)] - \gamma(x) - 1. \quad (2.22)$$

Eq. (2.21) and Eq. (2.22) are solved by iteration using the mixing method [17] in order to ensure convergence. Which means in every iteration step the result of the current step for $c(x)$, is mixed with some percentage of the result of the last step.

The iteration is done n times from an initial guess, $c^{(0)}(x)$

$$\left[\int_0^R |c^{(n+1)}(x) - c^{(n)}(x)|^2 dx \right]^{1/2} < \delta, \quad (2.23)$$

with $\delta = 10^{-5}$, where R is the cut-off length of $c(x)$. We employ $R = 47.1239$ and a mesh of size $M = 2396$ points. Consequently, the resolution (step size) in real and Fourier space is $\Delta x = R/M = 0.0197$ and $\Delta q = \pi/R = 0.0667$, respectively. An orthogonality-preserving algorithm is used for the numerical calculation of Fourier transforms [82]. To calculate the structure factors for Yukawa potentials with particular κ and a range of Γ s: we begin the computation of $c(x)$ at a small coupling parameter Γ . Then we successively increase Γ . In each step we use the outcome as an initial guess for the subsequent calculation with higher Γ values [70]¹. For the smallest Γ we use the initial guess of $c^{(0)}(x) = -U(x)/(k_B T)$. After obtaining the structure factor over the aforementioned Fourier spaced grid, we use interpolation to have the structure factor over the same grid points which we have in the MCT discretized kernels. The MCT kernel is discretized over 100 points where the step size is $\Delta = 0.4$, $q = \Delta \hat{q}$ and $\hat{q} = 1/2, 3/2, 5/2, \dots, 199/2$.

In section 2.3.2 we compare the glass transition points of a Yukawa system calculated with the HNC structure factor and the glass transition points of a Yukawa system with the Percus-Yevick (PY) structure factor [83]. The reason for this comparison is that for high Yukawa parameter values, the potential becomes very stiff and resembles a hard sphere potential and in the hard sphere system the PY approximation is known to be more accurate [17]. The PY closure can be written as

$$c(x) = (1 + \gamma(x)) (\exp[-U(x)/(k_B T)] - 1), \quad (2.24)$$

where $U(x)$ is the interaction potential. Except the closure form which is different, the procedures and numerical values employed to obtain the PY structure factor are the same as for the HNC which we explained. In PY we start the $c(x)$ iteration for the low Γ with the first initial guess $c^{(0)}(x) = \exp[-U(x)/(k_B T)] - 1$.

¹The structure factor code which I used was first written by A. Wysocki.

2.3. Results

2.3.1. Transition Curve

Any Yukawa potential can be determined by two parameters: Potential strength Γ and the screening parameter κ . For every potential associated with the pair (κ, Γ) we can calculate the structure factor S_q within HNC approximation according to the procedure explained in section 2.2.2. The structure factor is an input to the memory kernel in Eq. (2.11). Using the discretized memory kernel we solve Eq. (2.12) iteratively. If the resulting f_q is zero we are in the liquid state and if $f_q > 0$ we are in the glassy state. For every particular κ value, we check the f_q of several values of Γ . In every step if we have a glass ($f_q > 0$) we choose a lower Γ and if we have a liquid ($f_q = 0$) we choose a higher Γ value to approach the transition point. For every κ value the lower most Γ in the parameter plane which result in a non-zero f_q value, identifies a glass transition point. In Fig. 2.1 we have shown the glass transition points for a wide range of screening parameters.

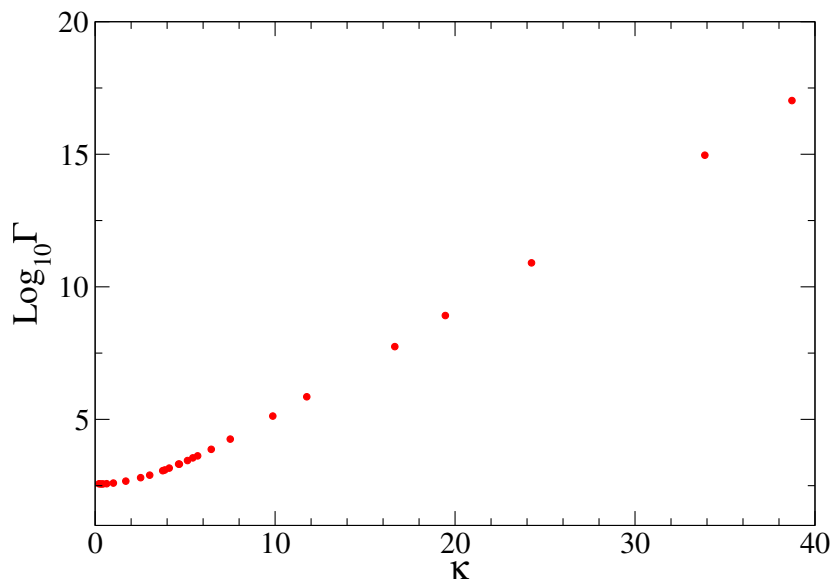


Figure 2.1.: Glass transition points of the Yukawa model system calculated within MCT and HNC approximation in the potential parameters plane (κ, Γ) .

One can observe that with increasing κ the transition Γ values increase which indicates that when the screening length λ of the potential decreases, the particles should be more charged or the temperature should be lower for the transition to happen. Fig. 2.2 shows the transition points along with the melting curve of the similar system for comparison. The melting line shows the transition from an ordered solid to

a disordered liquid and follows the analytical formula $\Gamma(\kappa) = 106 e^\kappa / (1 + \kappa + \kappa^2/2)$ which is proposed by [84, 85]. The analytical formula is in very good agreement with the simulation data of Ref. [86] for $\kappa \lesssim 8$. One should note that when one considers the Wigner-Seitz radius $\sqrt[3]{3/4\pi n}$ as the unit of length instead of $1/\sqrt[3]{n}$ the constant number in the $\Gamma(\kappa) = 106 e^\kappa / (1 + \kappa + \kappa^2/2)$ changes from 106 to $\simeq 172$. The formula is derived by [84] based on the Lindemann [87] type argument: the melting happens when the mean squared displacement of the particles exceeds a certain fraction of the average particles distance. They consider the mean square displacement of the particles in a one dimensional Yukawa lattice to be inverse proportional to their oscillation frequency [72] taking to account only the nearest neighbors and use the Lindemann rule to obtain the analytical formula. We can observe in Fig. 2.2 that the evolution of the glass transition points seems to be parallel with the melting curve. Here we use a similar argument to [84], to explain the resembling behavior of the glass transition and the melting curve in the κ and Γ parameter plane.

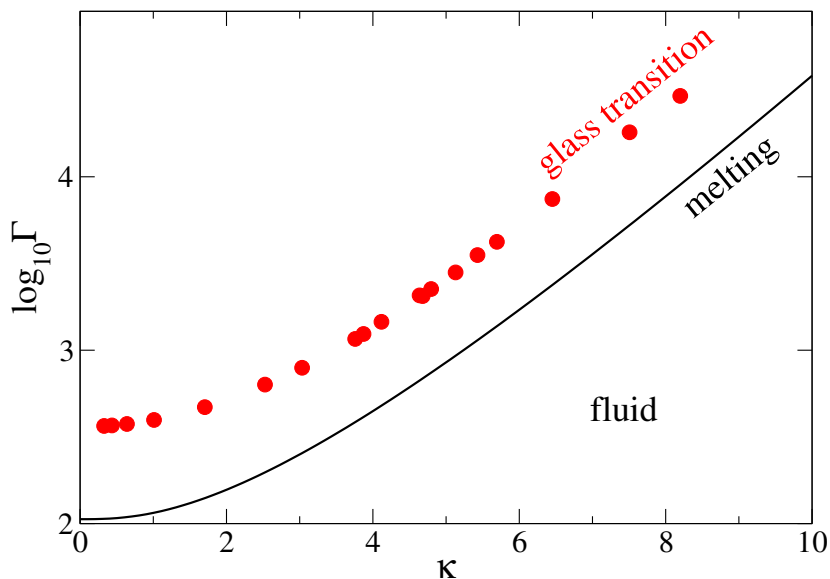


Figure 2.2.: Comparison between glass transition and the melting curve of the Yukawa model system. Filled circles show the MCT-HNC glass transition points. The solid curve is the melting curve from [84].

In general the only input to the MCT equations is the structure factor. Therefore if we want to find a relation for the qualitative behavior of the MCT transition curve we have to look at the structure factor. We use the quantity $\psi(x)$ named the potential of mean force [17, 88]

$$\psi(x) = -k_B T \ln g(x), \quad (2.25)$$

where $g(x)$ is the pair distribution function and related to the structure factor

through the Fourier transform

$$S_q = 1 + \int d^3x e^{i\mathbf{q}\cdot\mathbf{x}} (g(x) - 1). \quad (2.26)$$

If we assume two arbitrary particles in the system, particle 1 and 2, $\psi(x_{12})$ can be interpreted as the reversible work for a process in which particle 1 and 2 are brought to the relative separation x_{12} , from an initial infinite separation. From Eq. (2.25)

$$\psi(x_{12}) = -k_B T \left[\ln \int d\mathbf{x}_3 \cdots d\mathbf{x}_n e^{-\frac{U_T(\{\mathbf{x}^N\})}{k_B T}} + C \right], \quad (2.27)$$

where U_T is the total potential energy originating from all particles. Taking a derivative of the potential of the mean force leads to

$$\frac{\partial \psi(x_{12})}{\partial \mathbf{x}_1} = \frac{\int d\mathbf{x}_3 \cdots d\mathbf{x}_n \left(\frac{\partial U_T}{\partial \mathbf{x}_1} \right) e^{-\frac{U_T(\{\mathbf{x}^N\})}{k_B T}}}{\int d\mathbf{x}_3 \cdots d\mathbf{x}_n e^{-\frac{U_T(\{\mathbf{x}^N\})}{k_B T}}}. \quad (2.28)$$

This quantity shows the amount of force on particle 1, averaged over the position of the other particles 3, 4, \dots , where particle 1 and 2 are kept fixed at \mathbf{x}_1 and \mathbf{x}_2 . Now if we assume that particle 2 remains fixed while particle 1 changes its position by a small value $d\mathbf{x}_1$, we can use Eq. (2.28) to observe the change in the potential of mean force $\Delta\psi = \frac{\partial \psi(x_{12})}{\partial \mathbf{x}_1} \cdot d\mathbf{x}_1$. We assume that the total interaction potential consist of the sum of pair interactions only, $U_T = \sum_i U$. When the distance between particle 1 and any other particle is x_{1i} , the relative change of interparticle distance between particle 1 and particle i can be written as $dx = d\mathbf{x}_1 \cdot (\mathbf{x}_1 - \mathbf{x}_i)$. We show the average over the position of the particles 3, 4, \dots by $\langle \cdots \rangle_i$. Therefore from Eq. (2.28) we have

$$\Delta\psi = \left\langle \frac{\sum_i U(x_{1i} + dx)}{k_B T} - \frac{\sum_i U(x_{1i})}{k_B T} \right\rangle_i. \quad (2.29)$$

The change in ψ is equivalent to the sum of the changes in the pairwise interactions between all the particles in the system and particle 1 average over the positions of the other particles.

The pairwise interactions are in the form of Yukawa potentials. Using the Taylor expansion we can write

$$\begin{aligned} \left\langle \frac{U(x_{1i} + dx)}{k_B T} - \frac{U(x_{1i})}{k_B T} \right\rangle_i &= - \left\langle \frac{1 + \kappa x_{1i}}{x_{1i}^2} \Gamma e^{-\kappa x_{1i}} dx \right\rangle_i \\ &+ \left\langle \frac{2 + 2\kappa x_{1i} + \kappa^2 x_{1i}^2}{2x_{1i}^3} \Gamma e^{-\kappa x_{1i}} dx^2 \right\rangle_i + \dots \end{aligned} \quad (2.30)$$

Due to symmetry the first term on the right hand side of Eq. (2.30) will be canceled. In a strongly coupled Yukawa system, the interactions between the particles are dominated by those at mean interparticle distances [89], or $x \approx 1$. The change in the potential of the mean force is then approximately proportional to the second term in Eq. (2.30)

$$\Delta\psi \propto \Gamma e^{-\kappa}(1 + \kappa + \kappa^2/2). \quad (2.31)$$

At the glass transition every particle 1 can change its position inside the cage until it is hindered by neighboring particles (localization length). In the hard-sphere system the force on the particle in that regime (ballistic regime) is zero. Here the force on the particle is related to $\Delta\psi$. If the average particle in an average cage experiences the same forces along the line of glass transition, $\Delta\psi$ can be assumed approximately constant. So from Eq. (2.31)

$$\Gamma \propto \frac{e^\kappa}{1 + \kappa + \kappa^2/2}. \quad (2.32)$$

Therefore we expect that the glass transition points can be fitted by the same relation as in the melting line but the constant which change the proportionality in Eq. (2.32) to equality remains to be calculated by mode coupling theory.

Now we go back to our MCT-HNC result. Fig. 2.3 shows that the glass transition can be described by the function

$$\Gamma^c(\kappa) = \Gamma_{\text{OCP}}^c e^\kappa (1 + \kappa + \kappa^2/2)^{-1}, \quad (2.33)$$

where $\Gamma_{\text{OCP}}^c = 366$, is the transition potential strength at $\kappa = 0.33$. We do not calculate the transition point exactly in the limit of $\kappa = 0$ since obtaining a converging solution of both HNC and MCT in this limit is difficult.

One should also have in mind that in a hard sphere system the MCT and structure factor approximation leads to a transition point that should be shifted by 10% to match the experimental result [6, 90]. So here also we expect some deviation from the experiment but the qualitative predictions should be reliable.

2.3.2. Glass Form Factors

As we mentioned in section 2.2.1, we can obtain the form factor from solving Eq. (2.12). The critical form factor f_q^c , is the form factor at the glass transition

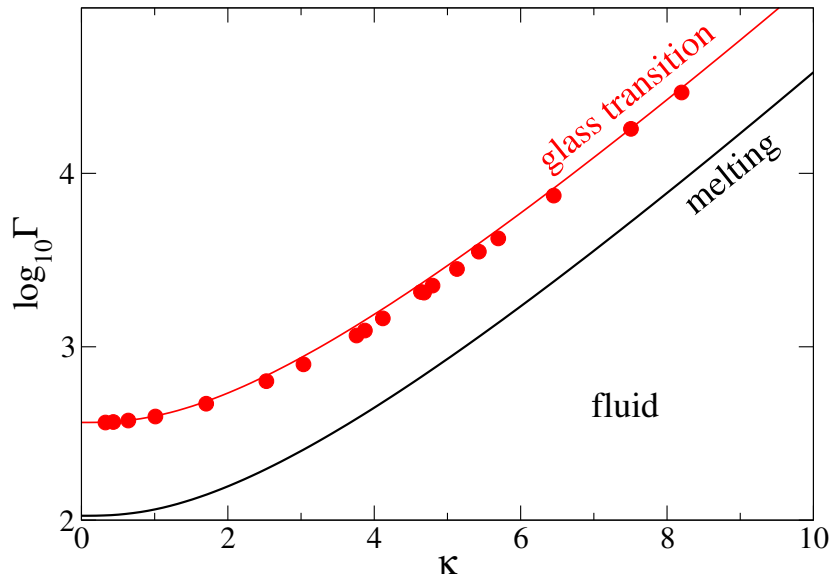


Figure 2.3.: The solid red curve shows the analytical formula in Eq. (2.33). The filled circles are the MCT-HNC transition points from Fig. 2.2 and the solid black curve shows the melting curve from [84].

point. Fig. 2.4 displays the critical form factors f_q^c of the selected Yukawa transition points which are shown in the inset. The red squares exhibit the form factor of the transition point with $\kappa = 0.33$ and $\Gamma = 366$. The first peak value at $q \simeq 2\pi$ shows that the long time limit of the density autocorrelation function has a maximum value for the wave length equal to the mean interparticle distance. This means that the glass is less resistant to a density fluctuation with the wave length equal to the mean interparticle distance and if an initial density fluctuation with that wave length is assumed it will remain in the system. This property indicates the cage effect [6]. As it is visible in the figure 2.4, the first peak height of the f_q is the nearly the same for all the transition points.

One can observe in figure 2.4 that at the OCP limit, the small q part of the form factor approaches zero while larger κ values result in a finite value of f_q in the small q region. We will return to this point in section 2.3.3.

Now we want to compare the f_q of the Yukawa system with a hard sphere system (HSS). In a hard sphere system the Percus-Yevick (PY) structure factor is known to be more accurate than the HNC [17]. In case of HSS, the PY closure for the direct correlation function $c(r)$ together with the Ornstein-Zernike equation, has an analytical solution [17]. The structure factor is calculated via Fourier transforming

$g(r)$. The control parameter for the HSS is the packing fraction

$$\varphi = \frac{\pi d^3 n}{6}, \quad (2.34)$$

where d is the hard-sphere diameter and n is the number density. We obtain the f_q of the HSS via Eq. (2.12) using 300 points grid with $q_{\min} = 0.067$ and $q_{\max} = 39.933$ and $\Delta = 0.133$ for discretizing the MCT integrals. The transition packing fraction is at $\varphi_c = 0.516$. The dashed curve in Fig. (2.4) shows the MCT-PY f_q of the hard sphere system. The horizontal axis in Fig. (2.4) in case of the HSS results, is qd where q is the Fourier conjugate variable to the center-to-center distance r between the spheres. However for HSS result to be comparable with the Yukawa, it is reasonable to have the structural inputs calculated with the same closure. Thus, we calculate the structure factor of the HSS within HNC closure using the method explained in section 2.2.2, with the difference that, since the HSS potential is discontinuous we use more grid points $M = 32 \times 2396$. We again obtain the f_q of HSS from Eq. (2.12) using the HNC structural input. The MCT-HNC transition packing fraction of HSS is at $\varphi_c = 0.525$. The HSS f_q using HNC structure factor is shown in Fig. (2.4) with solid curve labeled HSS-HNC. The differences between the form factors of the HSS calculated using HNC or PY is almost indistinguishable when comparing to the experiment, cf. [91], except for the small q regime. In the small q regime the experiment favors the PY result in case of the hard sphere system. One can conclude that with increasing κ and Γ the form factor of the Yukawa system resembles the form factor of a hard sphere system.

We have shown some representative Yukawa potentials at the transition, in Fig. 2.6. One can observe that when κ and Γ increases the Yukawa potential becomes quiet stiff and shorter range. We have used HNC structure factor for the whole range of the Yukawa parameter to obtain the transition points in the Yukawa system but here we want to compare our result with PY. We calculate the structure factor of the Yukawa potential for $\kappa > 10$, using PY closure in Eq. (2.24). We obtain the transition points repeating the procedure mentioned in the beginning of section 2.3.1 to obtain the Yukawa transition points this time using the PY structure factor. The result is shown in Fig. 2.5 with full triangles. It is visible that there is no qualitative difference between HNC and PY result in high (κ, Γ) regime in terms of following the formula in Eq. (2.33).

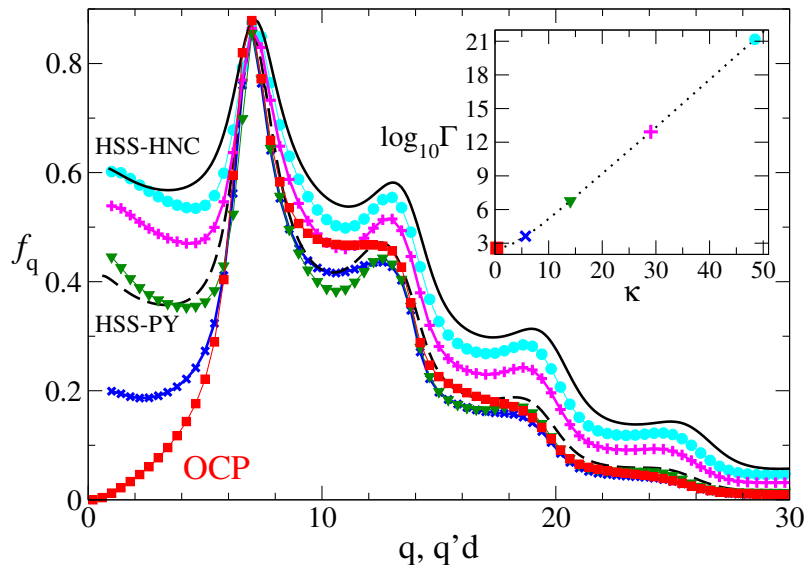


Figure 2.4.: Representative form factors at the selected transition points displayed in the inset. The solid line shows the MCT form factor of a hard sphere system with HNC approximation of the structure factor at the transition packing fraction $\varphi_c = 0.525$ where the dashed curve shows the form factor of the hard sphere system within MCT-PY at $\varphi_c = 0.516$.

2.3.3. Small q Behavior of the Glass Form Factor

In the OCP limit, f_q approaches zero in the small q region. This is due to the small q limit of the structure factor and vanishing compressibility. One can relate the isothermal compressibility of the Yukawa system to the structure factor as

$$k_B T \chi_T = 1 + \int [g(x) - 1] d^3x = S_{q \rightarrow 0}, \quad (2.35)$$

where χ_T is the isothermal compressibility. A similar relation is valid for the HSS [17], with the difference that in the HSS, the $S_{q \rightarrow 0}$ is a finite value resulting in a finite compressibility but in the OCP limit zero $S_{q \rightarrow 0}$, causes vanishing compressibility. The structure factor can be defined as the density response of the system to an external field [17], therefore a vanishing structure factor $S_{q \rightarrow 0} = 0$, means no matter how large the external field, the response of the system is zero. Therefore one needs to introduce an infinite external field to create a long wave length fluctuation. If one assumes an initial long wave length density fluctuation in the OCP glass, eventually, the system becomes completely uncorrelated to its initial state. This manifest itself in $f_{q \rightarrow 0} = 0$.

The structure factor in the OCP limit is $\propto q^2$ in the small q region. We explain

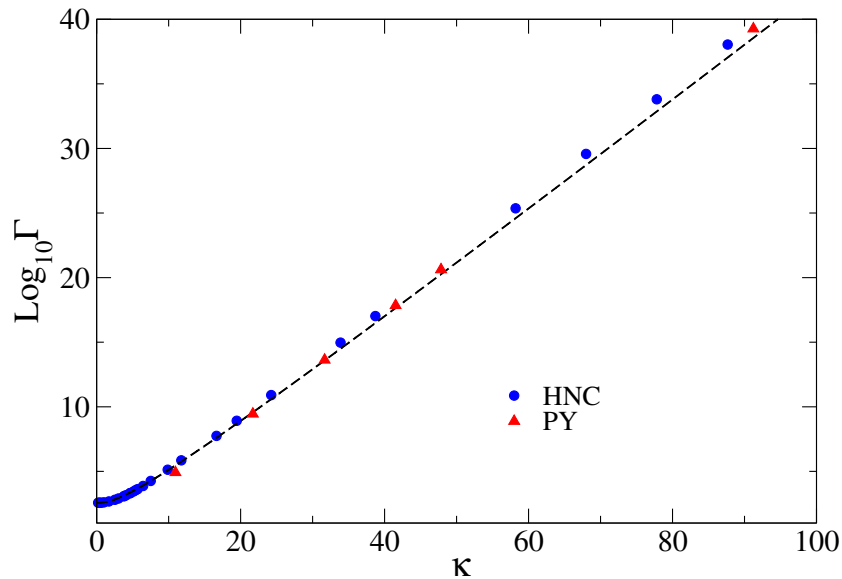


Figure 2.5.: Comparison between the transition values for large values of the parameters κ and Γ with structural input calculated within HNC (filled blue circles) and Percus-Yevick (red triangles) approximation. Equation (2.33) is shown as a dashed curve.

the reason as follows: The direct correlation function, can be written as $c(x) \simeq -U(x)/k_B T$ [17] in the large x regime. Therefore in the small q regime the behavior of c_q , is defined by the Fourier transform of the potential

$$c_q \simeq -U(q)/k_B T. \quad (2.36)$$

In three dimensions the Fourier transform of an arbitrary function $\omega(r)$ can be written as [6]

$$\Omega(k) = \frac{4\pi}{k} \int_0^\infty x\omega(x)\text{sink}x dx, \quad (2.37)$$

therefore for the Coulombic potential $U(x)/k_B T = \Gamma/x$ in the OCP limit

$$\begin{aligned} \frac{U(q)}{k_B T} &= \frac{4\pi}{q} \int_0^\infty \text{sin}qx \, dx \\ &= \lim_{\varepsilon \rightarrow 0} \frac{4\pi}{q} \text{Im} \left(\int_0^\infty \exp(iqx - \varepsilon x) \, dx \right) \\ &= \frac{4\pi\Gamma}{q^2}. \end{aligned} \quad (2.38)$$

Using the Ornstein-Zernike equation

$$S_{q \rightarrow 0} = \frac{1}{1 - c_{q \rightarrow 0}}, \quad (2.39)$$

we obtain

$$S_{q \rightarrow 0} = \frac{q^2}{4\pi\Gamma}. \quad (2.40)$$

In principle one can separate the direct correlation function into two parts: The short range regular part c_q^R and the long range singular part c_q^S . At $q \rightarrow 0$ the singular part $c_q^S = -U(q)/k_B T$ and therefore as it is derived in [92]

$$S_q = \frac{q^2}{4\pi\Gamma} + \frac{q^4}{(4\pi\Gamma)^2} [c_0^R - 1] + \mathcal{O}(q^6). \quad (2.41)$$

For obtaining the small q behavior of f_q , we first start with Eq. (2.10) which can be also written as

$$\mathcal{F}_q(f) = \frac{1}{8\pi^3} \int d^3k V(\mathbf{q}, \mathbf{k}, \mathbf{p}) f_k f_p, \quad (2.42)$$

where

$$V(\mathbf{q}, \mathbf{k}, \mathbf{p}) = \frac{1}{2} \frac{S_q S_k S_p}{q^4} [\mathbf{q} \cdot \mathbf{k} c_k + \mathbf{q} \cdot \mathbf{p} c_p]^2 \delta(\mathbf{q} - \mathbf{k} - \mathbf{p}). \quad (2.43)$$

The delta function leads to $\mathbf{p} = \mathbf{k} - \mathbf{q}$. We can apply that to the vertices

$$V(\mathbf{q}, \mathbf{k}, \mathbf{p}) = \frac{1}{2} \frac{S_q S_k S_p}{q^4} [\mathbf{q} \cdot \mathbf{k} c_k + \mathbf{q} \cdot (\mathbf{q} - \mathbf{k}) c_{|\mathbf{q}-\mathbf{k}|}]^2. \quad (2.44)$$

We follow the method mentioned in [41]. We name the angle between \mathbf{q} and \mathbf{k} , θ so we can Taylor expand $c_p = c_{|\mathbf{q}-\mathbf{k}|}$ as

$$c_{|\mathbf{q}-\mathbf{k}|} = c_{|\mathbf{k}|} + \left(\mathbf{q} \cdot \vec{\nabla} \right) \Big|_{-\mathbf{k}} c_{|\mathbf{k}|} + \frac{1}{2} \left(\mathbf{q} \cdot \vec{\nabla} \right)^2 \Big|_{-\mathbf{k}} c_{|\mathbf{k}|} + \frac{1}{6} \left(\mathbf{q} \cdot \vec{\nabla} \right)^3 \Big|_{-\mathbf{k}} c_{|\mathbf{k}|} + \dots \quad (2.45)$$

where $\mathbf{q} \cdot \vec{\nabla} = \mathbf{q} \cdot \hat{\mathbf{p}} \frac{\partial}{\partial p}$, which in the small q limit is equal to $-q \cos \theta \frac{\partial}{\partial k}$. Also $c_{|\mathbf{k}|} = c_k$, therefore

$$c_{|\mathbf{q}-\mathbf{k}|} = c_k - c'_k q \cos \theta + \frac{1}{2} q^2 \cos^2 \theta c''_k - \frac{1}{6} q^3 \cos^3 \theta c'''_k. \quad (2.46)$$

where we have neglected the higher order terms. Substitution of Eq. (2.46) in

Eq. (2.44) leads to

$$V(\mathbf{q}, \mathbf{k}, \mathbf{p}) \simeq \frac{1}{2} \frac{S_q S_k S_p}{q^4} \left[\underbrace{q^2 (c_k + k c'_k \cos^2 \theta)}_a + \underbrace{q^3 (-c'_k \cos \theta - \frac{1}{2} k \cos^3 \theta c''_k)}_b + \underbrace{q^4 (\frac{1}{2} \cos^2 \theta c''_k + \frac{1}{6} k \cos^4 \theta c'''_k)}_c \right]^2. \quad (2.47)$$

We remind ourselves that this is the integrand of the integral in Eq. (2.42). For obtaining different orders of q in \mathcal{F}_q , we first keep the S_q outside the integral. Later we talk about the dependence of S_q on q .

We start with calculating the term in \mathcal{F}_q which is only proportional to S_q and does not have any other q dependency. For that we should choose the term a^2 from $[a + b + c]^2 = a^2 + b^2 + c^2 + 2ab + 2bc + 2ac$ in Eq. (2.47). We replace the a^2 term inside Eq. (2.42) knowing that $d^3k = 2\pi k^2 dk \sin \theta d\theta$ or $d^3k = 2\pi k^2 dk d(\cos \theta)$

$$\begin{aligned} \mathcal{F}_{S_q}(f) &= \frac{2\pi S_q}{16\pi^3} \int_0^\infty dk k^2 S_k^2 f_k^2 \int_{-1}^1 \frac{q^4}{q^4} (c_k^2 + 2k c_k c'_k \cos^2 \theta + k^2 c_k'^2 \cos^4 \theta) d(\cos \theta) \\ &= \frac{S_q}{4\pi^2} \int_0^\infty dk k^2 S_k^2 \left(c_k^2 + \frac{2}{3} k c_k c'_k + \frac{1}{5} k^2 c_k'^2 \right) f_k^2. \end{aligned} \quad (2.48)$$

For obtaining the \mathcal{F}_q terms which are proportional to $q S_q$, we have to replace the $2bc$ term from Eq. (2.47) inside Eq. (2.42). This contains the integration $\int_{-1}^1 d(\cos \theta)$, of only odd powers of $\cos \theta$ which results in zero.

For the term proportional to the $q^2 S_q$ we place the b^2 and $2ac$ from Eq. (2.47) in Eq. (2.42). Hence

$$\begin{aligned} \mathcal{F}_{q^2 S_q}(f) &= \frac{S_q q^2}{8\pi^2} \int_0^\infty dk k^2 S_k^2 f_k^2 \int_{-1}^1 (c_k'^2 \cos^2 \theta + \frac{1}{4} k^2 c_k'' \cos^6 \theta + k c_k' c_k'' \cos^4 \theta \\ &\quad + c_k c_k'' \cos^2 \theta + \frac{1}{3} k c_k c_k''' \cos^4 \theta + k c_k' c_k'' \cos^4 \theta + \frac{1}{3} k^2 c_k' c_k''' \cos^6 \theta) d(\cos \theta) \\ &= \frac{q^2 S_q}{4\pi^2} \int_0^\infty dk k^2 S_k^2 \left(\frac{1}{3} c_k'^2 + \frac{1}{28} k^2 c_k''^2 + \frac{2}{5} k c_k' c_k'' + \frac{1}{3} c_k c_k'' \right. \\ &\quad \left. + \frac{1}{15} k c_k c_k''' + \frac{1}{21} k^2 c_k' c_k''' \right) f_k^2. \end{aligned} \quad (2.49)$$

In summary the small q dependence of \mathcal{F}_q can be written as

$$\mathcal{F}_q(f) = \alpha S_q + \beta q^2 S_q + \mathcal{O}(q^3), \quad (2.50)$$

where [41]

$$\alpha = \frac{1}{4\pi^2} \int_0^\infty dk k^2 S_k^2 \left(c_k^2 + \frac{2}{3} k c_k c_k' + \frac{1}{5} k^2 c_k'^2 \right) f_k^2, \quad (2.51)$$

and from Eq. (3.37)

$$\begin{aligned} \beta = \frac{1}{4\pi^2} \int_0^\infty dk k^2 S_k^2 & \left(\frac{1}{3} c_k'^2 + \frac{1}{28} k^2 c_k''^2 + \frac{2}{5} k c_k' c_k'' \right. \\ & \left. + \frac{1}{3} c_k c_k'' + \frac{1}{15} k c_k c_k''' + \frac{1}{21} k^2 c_k' c_k''' \right) f_k^2. \end{aligned} \quad (2.52)$$

From Eq. (2.50) and Eq. (2.41) we get

$$\mathcal{F}_q = q^2 \frac{\alpha}{4\pi\Gamma} + q^4 \left[\frac{\beta}{4\pi\Gamma} + \frac{\alpha}{(4\pi\Gamma)^2} (c^R(0) - 1) \right] + \mathcal{O}(q^6). \quad (2.53)$$

In the OCP limit when $q \rightarrow 0$, \mathcal{F}_q approaches zero with leading order q^2 dependency.

From Eq. (2.5),

$$f_q = \frac{\mathcal{F}_q}{1 + \mathcal{F}_q}, \quad (2.54)$$

therefore the f_q has the same behavior as \mathcal{F}_q at vanishing q in the OCP limit.

We leave the OCP limit now, and increase the screening parameter κ . Looking back to the Fig. (2.4), the f_q of the Yukawa system for non vanishing screening, $\kappa > 0$, has a non zero intercept. This is due to that the singular part of the direct correlation function $c_q^S = -U(q)/k_B T = \frac{4\pi\Gamma}{q^2 + \kappa^2}$ in case of $q \rightarrow 0$ and $\kappa > 0$ stays finite therefore the structure factor and the compressibility will not approach zero. At increasingly high value of κ and Γ the small q limit of f_q approaches the values which correspond to the HSS.

2.3.4. Hard-Sphere Limit

In the high κ and Γ values at the transition, the Yukawa system behaves like a HSS. A hard sphere potential is defined as $U(r)/k_B T = 0$ when the inter-particle distance is greater than the diameter of the spheres, $r > d$, and $U(r)/k_B T = \infty$ when $r < d$.

Therefore it is possible to resemble a hard sphere system potential with

$$\frac{U_{\text{HS}}}{k_{\text{B}}T} = \frac{e^{-\kappa(r-d)}}{r} \quad \text{for large } \kappa. \quad (2.55)$$

Which has the same property of being zero when $r > d$ and being very large when $r < d$. We can write the Yukawa potential at the transition in the form of Eq. (2.55) when $\Gamma = \exp(\kappa d_{\text{eff}})$, therefore

$$d_{\text{eff}}^c = \frac{\ln \Gamma^c}{\kappa}. \quad (2.56)$$

Using Eq. (2.34), we can also define an effective packing fraction

$$\varphi_{\text{eff}}^c = \frac{\pi}{6} \left(\frac{\ln \Gamma^c}{\kappa} \right)^3, \quad (2.57)$$

where we have considered the unit of length as $n^{-1/3}$. Thus the density n does not appear in the formula. One can derive the same effective diameter and packing fraction simply assuming $U(d_{\text{eff}})/k_{\text{B}}T = \Gamma \exp(-\kappa d_{\text{eff}})/d_{\text{eff}} \sim 1$ in the Yukawa potential. We have shown some representative Yukawa potentials at the transition, in Fig. 2.6. One can observe that at $(\kappa, \Gamma) = (1.01, 396)$ the potential is quite soft and the effective diameter is greater than 4. In contrast, when $(\kappa, \Gamma) = (38.71, 1.06 \times 10^{17})$ the potential is quite hard, basically the same as a hard sphere potential with the effective diameter nearly equal to 1. We have shown the effective hard-sphere packing fractions and diameters of the Yukawa glass transition points in Fig. 2.7. For small- κ values the effective packing fraction is larger than unity since the effective spheres overlap and the potential is soft. At large κ values, $\kappa \gtrsim 30$, the effective packing fraction approaches the critical packing fraction of the hard sphere system calculated within the HNC approximation of the structure factor.

2.3.5. Localization Length

We use Eq. (2.14) and (2.16) to numerically obtain the localization length r_s^c of the Yukawa system along the transition curve. The input to those equations is f_q^s which we calculate through Eq. (2.17) and (2.20) using the already obtained f_q . The result is shown in figure 2.8. In the OCP limit the localization length is 0.07 and it increases with increasing κ . At $\kappa \simeq 10$ the localization length reaches its maximum value. Towards the HSS limit the localization decreases again approaching the hard sphere localization length. The MCT localization length of HSS within HNC is

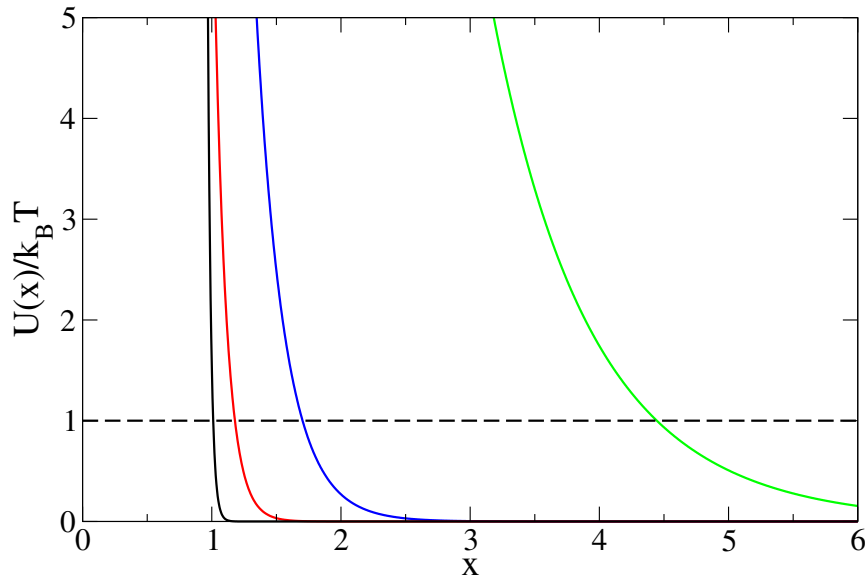


Figure 2.6.: Representative Yukawa potentials corresponding to the glass-transition points shown in Fig. 2.1. The potentials from right to left correspond to $(\kappa, \Gamma) = (1.01, 396)$, $(3.87, 1240)$, $(9.87, 1.34 \times 10^5)$, and $(38.71, 1.06 \times 10^{17})$.

$r_s^c/d = 0.0634$. The origin of maximum in the localization length is the interplay between growing screening (which weakens influence of far neighbors and therefore causes r_s^c to increase) and growing stiffness of the next-neighbor interactions (which causes r_s^c to decrease) [93]. In Fig. 2.9 we show a sketch of three states of the interactions for the central particle in green. Basically all blue particles shown in the figure have the same potential field around, as the green one. The dimensions of the particles are negligible in comparison to the average interparticle distance $l = 1/\sqrt[3]{n}$. From top to bottom, we are increasing κ along the transition curve. In the upper most panel the effective diameter (dashed circle) is much greater than l and even particles farther away than the first neighbors can interact effectively with the green particle. Decreasing the effective diameter (equivalent to increasing κ) weakens the influence of the far away neighbors and therefore causes an increase in the localization length. In the middle panel the effective diameter is nearly equal to l and the green particle only interacts with the close neighbors (the surrounding particles). Any further increase of κ , will not cause a pronounced change in the effective diameter but will make the interaction potential much stiffer (as it is shown in the lowest panel), therefore the localization length decreases again.

Also, as we see in Fig. 2.8 the overall changes of localization length along the transition curve is rather small. So our earlier assumption in section 2.3.1, that the average particle in an average cage experiences the same forces along the line of glass transition, is valid.

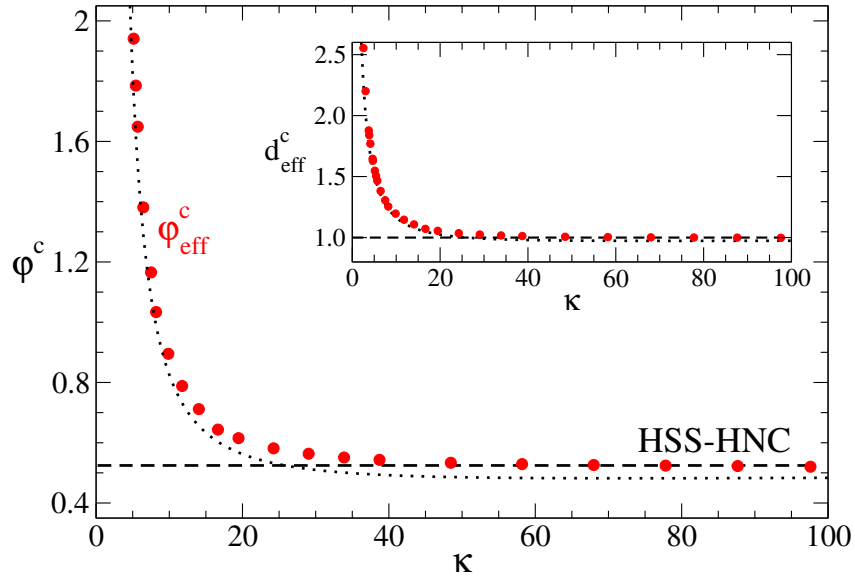


Figure 2.7.: Effective packing fraction and diameters for the Yukawa transition points shown in Fig. 2.1. The filled red circles show the effective packing fraction and effective diameters (inset) for the Yukawa glass transition points. The horizontal dashed line shows the HSS-HNC limit of $\varphi_{\text{HSS}}^c = 0.525$. The dotted line in both the figure and the inset represents the formula in Eq. (2.33).

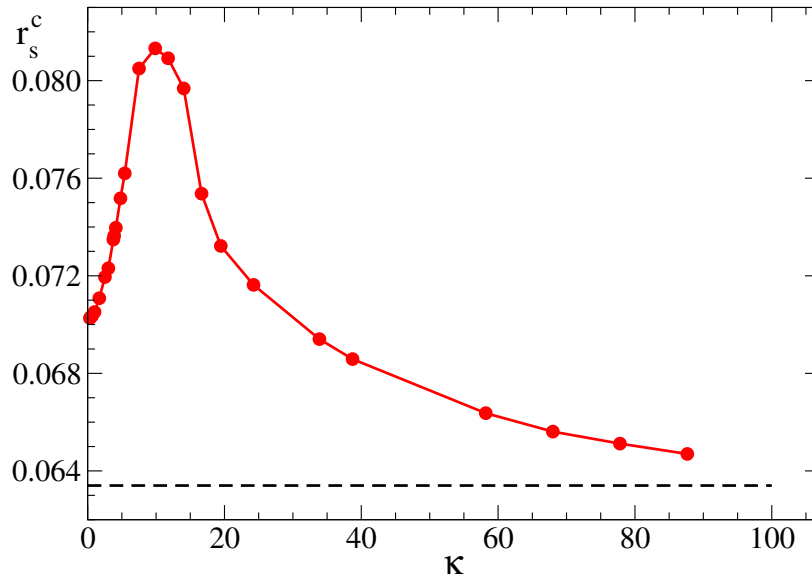


Figure 2.8.: Localization length of a Yukawa system. The horizontal dashed line shows the HSS localization length calculated within HNC-MCT approximation.

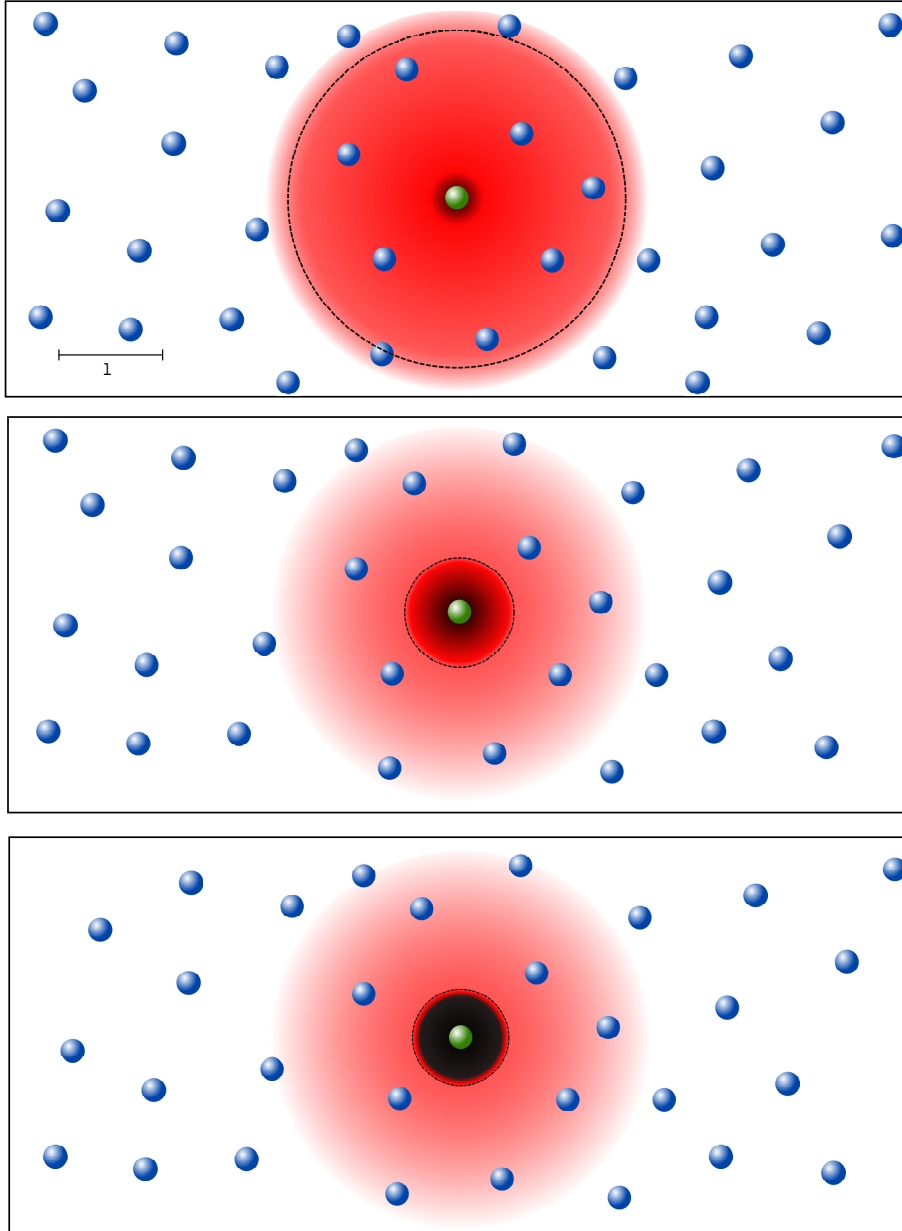


Figure 2.9.: Sketch of three state of the Yukawa interactions. The color code black-red-white show the strength of the interactions from high to low. All the particles are equivalent but for clarity we have shown the interaction field only around the central particle in green. The diameter of the dashed circle in all three panels shows the effective diameter in Eq. (2.56). $l = 1/\sqrt[3]{n}$ is the average interparticle distance. From top to bottom the screening parameter κ is increasing along the transition.

2.4. Double Yukawa Potential

Complex plasma consist of negatively charged dust particles immersed in a plasma background of electrons and ions. In an equilibrium situation these electrons and ions follow a Boltzmann distribution. When perturbations in the plasma potential are small, one can assume a linearized Boltzmann distribution of electrons and ions. From solving the Poisson equation in that case one obtains the Yukawa potential in Eq. (2.2) with $\kappa^2 = e^2 n_0 (1/T_i + 1/T_e) / (k_B T \epsilon_0)$ [72]. n_0 is the density of ions and electrons at $U = 0$, T_i is the temperature of the ions and T_e is the temperature of electrons. However there can be some mechanisms in plasmas which can cause deviations from the Boltzmann distribution for ions and electrons [94, 95], therefore the potential around the test charge also deviate from a single Yukawa potential. In [73], Khrapak *et al.* have taken into account plasma production and loss in a highly collisional plasma. Electron impact ionization causes the plasma production, where recombination of the plasma particles and their diffusion to the boundaries causes plasma losses. They have shown that the interaction potential in that case can be written in terms of the sum of two Yukawa potentials with different parameters as

$$\frac{U(x)}{k_B T} = \frac{\Gamma}{x} [\exp(-\kappa x) + \epsilon \exp(-\alpha \kappa x)] , \quad (2.58)$$

where ϵ and $\alpha < 1$ show the relative strength and screening parameter of the second longer range potential. When $\epsilon = 0$, we recover the single Yukawa potential in Eq. (2.2). We now use mode-coupling theory and the hypernetted chain closure approximation explained in section 2.2, to calculate the glass transition points in the κ and Γ plane for different α and ϵ .

2.4.1. Glass Transition

Using the HNC approximation of the structure factor, we obtain the glass transition points (κ, Γ) via MCT for the double Yukawa potential in Eq. (2.58). The procedure of obtaining (κ^c, Γ^c) of the transition is the same as the procedure for the single Yukawa potential which is explained in section 2.3.1. We have shown the transition points for $\alpha = 0.125$ and $\epsilon = 0.2$ (diamonds) in Fig. 2.10. For comparison, we show also the glass transition points for the single Yukawa potential ($\epsilon = 0$) with filled circles. One can observe that the double Yukawa transition curve follow the same behavior as the single Yukawa until $\kappa \simeq 5$.

Afterwards the double Yukawa curve separates from the single Yukawa. We scale the single Yukawa transition points by

$$\Gamma' = \Gamma/\epsilon, \quad \kappa' = \kappa/\alpha. \quad (2.59)$$

The scaled single Yukawa transition points is shown in Fig. 2.10 by empty circles. Scaling the describing function (2.33), which we repeat here as

$$\Gamma_1^c(\kappa) = \frac{\Gamma_{\text{OCP}}^c e^\kappa}{(1 + \kappa + \kappa^2/2)}, \quad (2.60)$$

according to Eq. (2.59), leads to

$$\Gamma_2^c(\kappa) = \frac{\Gamma_{\text{OCP}}^c e^{\alpha\kappa}}{\epsilon(1 + \alpha\kappa + \alpha^2\kappa^2/2)}. \quad (2.61)$$

$\Gamma_2^c(\kappa)$ is shown in Fig. 2.10 as a dashed curve. From the figure, one can perceive that the doubled Yukawa transition points follow the same behavior as the single Yukawa until $\kappa \simeq 5$, then it cross overs to the scaled single Yukawa. For $\kappa \gtrsim 8$, the doubled Yukawa transition points trace the scaled single Yukawa transition closely. Therefore we can predict that, the double Yukawa transition curve should overall follow the interpolation

$$\frac{1}{\Gamma^c(\kappa)} = \frac{1}{\Gamma_1^c(\kappa)} + \frac{1}{\Gamma_2^c(\kappa)} \quad (2.62)$$

or

$$\Gamma^c(\kappa)/\Gamma_{\text{OCP}}^c = [e^{-\kappa}(1 + \kappa + \kappa^2/2) + \epsilon e^{-\kappa\alpha}(1 + \kappa\alpha + \kappa^2\alpha^2/2)]^{-1}. \quad (2.63)$$

We have shown the analytical formula Eq. (2.63), in Fig. 2.11, by the green solid line. The function can describe the double Yukawa transition curve rather accurately.

In Fig. 2.12 we have shown the analytical function in Eq. (2.63) for the transition points calculated via MCT-HNC for $\alpha = 0.125$ and both $\epsilon = 0.2$, $\epsilon = 0.01$. The analytical function fits both $\epsilon = 0.2$ and $\epsilon = 0.01$ double Yukawas. The smaller is the ϵ , the double Yukawa transition crossovers from the single Yukawa to the scaled single Yukawa at a larger κ value. The scaled single Yukawas are shown with dotted and dashed curves for $\epsilon = 0.01$ and $\epsilon = 0.2$ respectively.

In Fig. 2.13 we have plotted the single Yukawa transition function and the scaled single Yukawa functions, Eq. (2.61), for different values of ϵ and $\alpha = 0.125$. The double Yukawa transition points, e.g. for $\epsilon = 0.2$ follows closely the single Yukawa

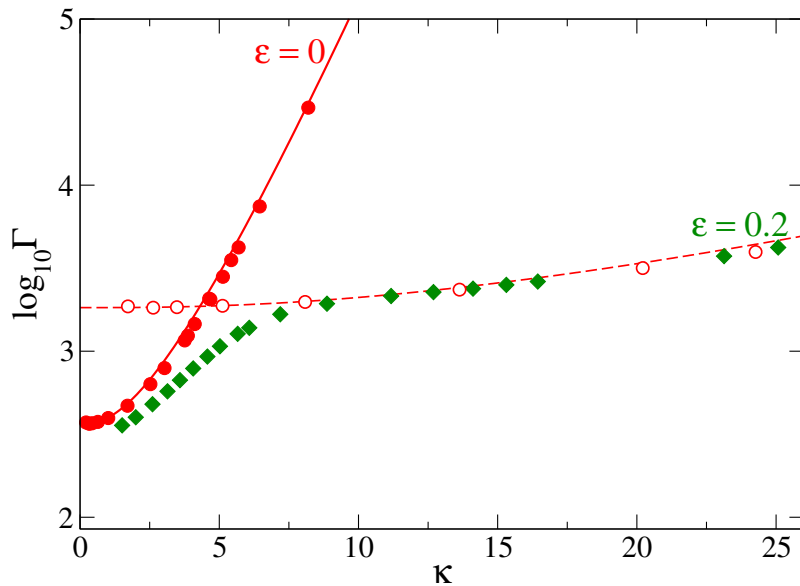


Figure 2.10.: Mode-coupling glass transition of the double Yukawa system for $\alpha = 0.125$ and $\epsilon = 0.2$ (diamonds). The filled circles show the single Yukawa ($\epsilon = 0$) transition points and the solid curve is the function in Eq. (2.33). The dashed curve demonstrate the scaled Yukawa function in Eq. (2.61). The open circles represent the scaled single Yukawa transition points via equation (2.59).

function until at the crossover point, where it changes its behavior to follow the scaled single Yukawa curve.

We show the intersection points of the single Yukawa function and the scaled single Yukawa for $\alpha = 0.125$ and $\alpha = 0.25$ each for different values of ϵ in Fig. 2.14. We can observe that for larger α , intersection happens later in terms of κ and Γ . This difference is more visible in the smaller values of ϵ , $\epsilon < 0.2$.

2.4.2. Localization Length

In Fig. 2.15 we have shown the double Yukawa localization length for $\alpha = 0.125$ and $\epsilon = 0.2$. We also have plotted the single Yukawa localization length, which we have explained before in section 2.3.1, again for comparison. The scaled single Yukawa localization lengths are shown by empty circles where we have scaled the κ values according to Eq. (2.59). One can observe that for small κ values, the double Yukawa localization lengths follow the single Yukawa curve. At $\kappa \gtrsim 5$, the values start to follow the scaled curve. The maximum is reached at $\kappa \approx 80$.

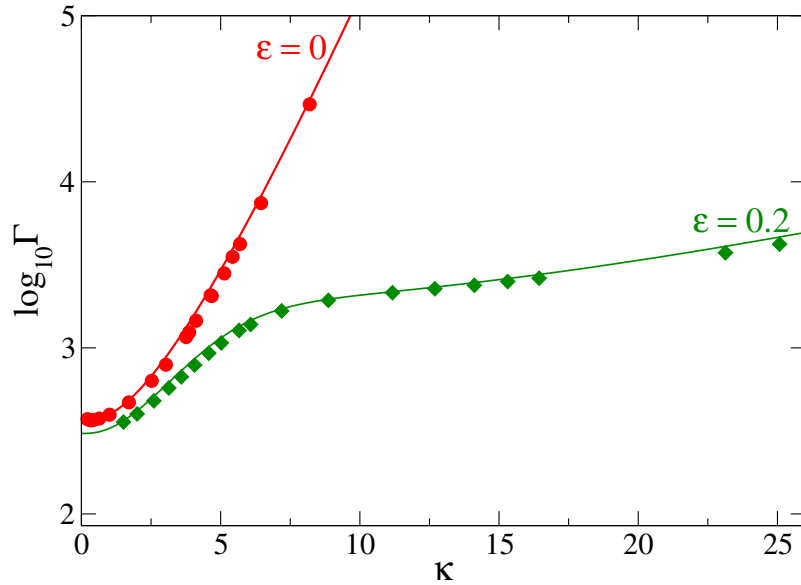


Figure 2.11.: Glass transition of the double Yukawa system for $\alpha = 0.125$ and $\epsilon = 0.2$ (diamonds). The solid green curve demonstrate the function in Eq. (2.63). The filled circles show the single Yukawa ($\epsilon = 0$) transition points and the solid red curve is the function in Eq. (2.33).

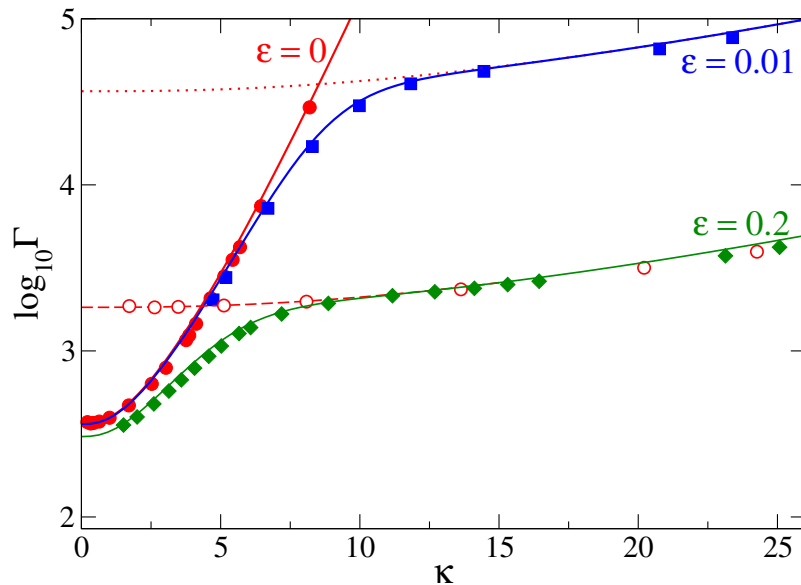


Figure 2.12.: Glass transition diagram for double Yukawa potentials with $\alpha = 0.125$, $\epsilon = 0.2$ (diamonds) and 0.01 (squares). The single Yukawa data (filled circles) is shown together with the analytical description by Eq. (2.33) (solid curve labeled $\epsilon = 0$). The single Yukawa points are scaled according to Eq. (2.59) for $\epsilon = 0.2$, and shown by open circles. Dotted and dashed curves represent Eq. (2.61) for $\epsilon = 0.01$ and $\epsilon = 0.2$, respectively. The solid curves labeled $\epsilon = 0.01$ and $\epsilon = 0.2$, respectively, show the solution of Eq. (2.63).

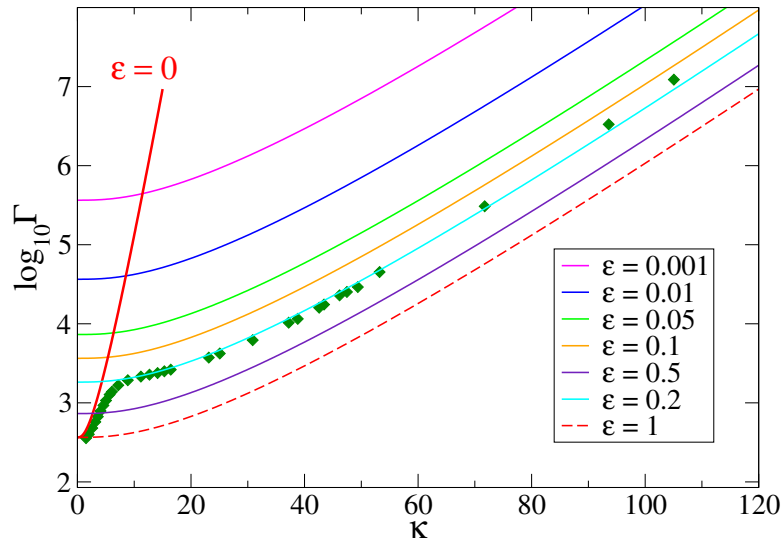


Figure 2.13.: Intersections of the single Yukawa analytical function Eq. (2.33), with the scaled single Yukawa Eq. (2.61), for $\alpha = 0.125$ and different values of ϵ . The single Yukawa analytical function is shown by the red solid curve labeled with $\epsilon = 0$. The mode coupling glass transition points of the double Yukawa system for $\alpha = 0.125$ and $\epsilon = 0.2$ are shown with diamonds.

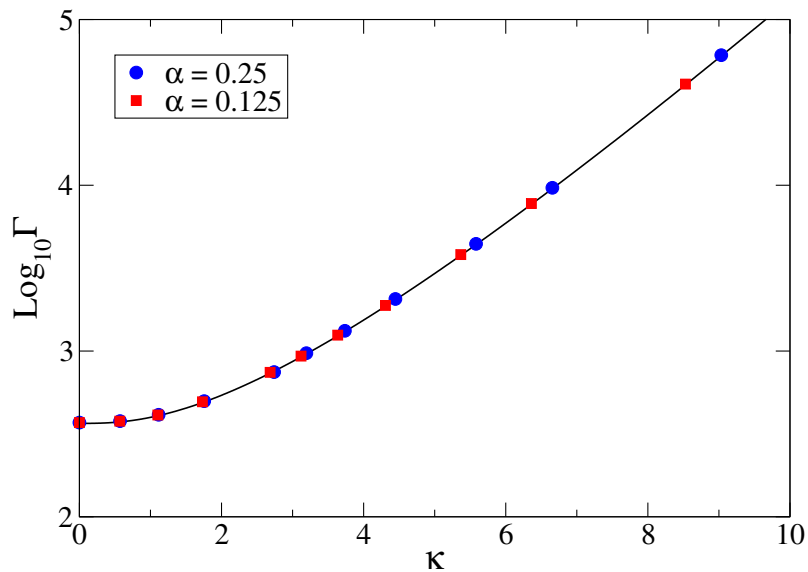


Figure 2.14.: The intersection points of the single Yukawa analytical function Eq. (2.33), with the scaled single Yukawa Eq. (2.61), for $\alpha = 0.125$ (filled squares) and $\alpha = 0.25$ (filled circles) each for $\epsilon = 1, 0.98, 0.9, 0.75, 0.5, 0.4, 0.3, 0.2, 0.1, 0.05, 0.01$ from left to right of the figure.

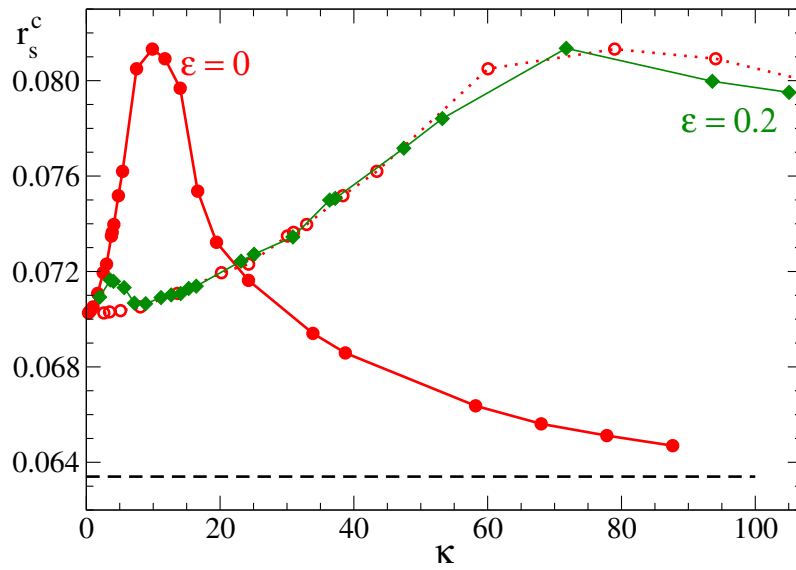


Figure 2.15.: Localization length of the double Yukawa system with $\alpha = 0.125$ and $\epsilon = 0.2$ shown with diamonds. The filled circles show the localization length of a single Yukawa system while the open circles exhibit the scaled single Yukawa localization lengths. The horizontal dashed line represents the HSS localization length calculated within HNC-MCT approximation.

Chapter 3

Glass Transition of Charged Particles in Two-Dimensional Confinement

This chapter is written based on Yazdi *et al.* [96]. The structure factors are produced by M. Heinen's program [97].

3.1. Yukawa Monolayer

As we have mentioned in the introduction, in complex plasma, the charged particles (dusts) which are embedded in the plasma (a mixture of ions and electrons and neutrals), can form a two dimensional layer [98]. The surrounding ions inside the plasma are distributed in a three dimensional volume (see Fig. 3.1). In an equilibrium situation and only when ions follow the Boltzmann distribution the potential at the distance r from a dust particle can be written as screened Coulomb or Yukawa potential

$$\Phi(r) = \frac{Q}{4\pi\epsilon_0 r} \exp(-r/\lambda_Y). \quad (3.1)$$

λ_Y is the screening length and Q is the charge of the dust particle. When dust particles are levitating in the form of a two dimensional layer, some phenomena can effect the measurements of the potential, e.g. ion depletion due to the absorption of particles on the probe surface [99]. Consideration of these phenomena leads to a potential which can be mapped to the Yukawa form with an effective charge Q_Y , which is less than the dust particle charge.

Since we need to use the pair interaction potential energy instead of the single particle potential in the future equations we multiply Eq. (3.1) with the Q_Y . To obtain a dimensionless quantity, we scale the pair interaction potential energy by $k_B T$, where k_B is the Boltzmann constant and T is the absolute temperature. Scaling the pair interaction potential energy by $k_B T$ also represents the ratio of the potential energy to the average kinetic energy. We assume the average interparticle distance $1/\sqrt{n}$ as the unit of length, where n is the number density of the dust particles. Applying all these to Eq. (3.1) we can write the dimensionless Yukawa potential energy as, cf. Eq. (2.2)

$$\frac{U_Y(x)}{k_B T} = \Gamma_Y \frac{\exp(-\kappa_Y x)}{x}, \quad (3.2)$$

where x is the dimensionless center to center distance of the dust particles, $x = r\sqrt{n}$. κ_Y is the screening parameter defined as the inverse of the dimensionless screening length $\kappa_Y = 1/(\lambda_Y\sqrt{n})$, and Γ_Y is the coupling parameter which quantifies the potential energy strength $\Gamma_Y = Q_Y^2\sqrt{n}/(4\pi\epsilon_0 k_B T)$. The two parameters κ_Y , Γ_Y characterize a Yukawa system.

In charged colloids, the two dimensional Yukawa potential has been used to describe the interaction between charge stabilized colloids confined between two parallel charged plates [100] or to a low angle wedge geometry [101].

Over this chapter we consider a model system of point particles in a two-dimensional plane interacting via Eq. (3.2) as a Yukawa monolayer. The plasma background enters our model only through its effect on the interaction potential (energy).

3.2. Kompaneets Monolayer

Complex plasma experiments consist of dust particles which levitate in a plasma background. There exist an external electrical field originating from the electrodes at the top and bottom of the plasma chamber, cf. [28, 30, 102]. In case of a radio frequency discharge in a weakly ionized low pressure plasma the dust particles levitating in the plasma acquire a large amount of negative charge and therefore they experience a high amount of electrostatic repulsion due to the external field. The high repulsion force will be balanced by gravity near the lower electrode thus the

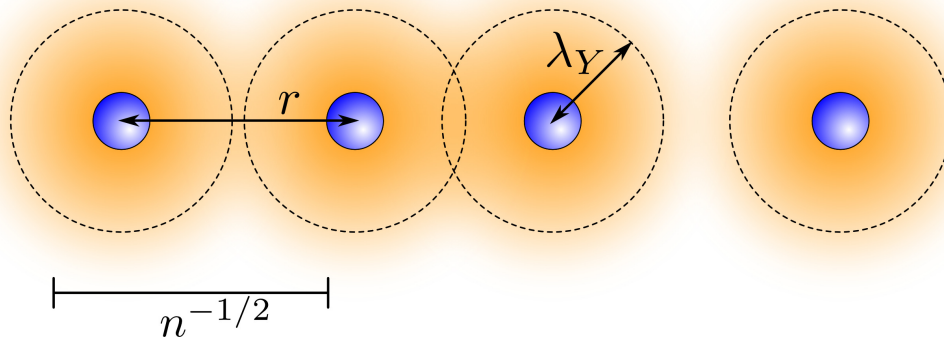


Figure 3.1.: Edge-on schematic of a Yukawa monolayer. Charged particles (filled circles) are confined to a plane, while oppositely charged ions are free to move in the surrounding, unbounded 3D space. The mean ion density is color-coded. Typical in-plane nearest neighbor distances are similar to the mean geometric distance $n^{-1/2}$, and of the same order of magnitude as the Yukawa screening length λ_Y . Particle separations greatly exceed the particle diameter. The effective particle interactions are quantified by the two dimensionless parameters Γ_Y and $\kappa_Y = 1/(\lambda_Y\sqrt{n})$. This figure is produced by M. Heinen and taken from [96].

dust particle form a two dimensional layer at the sheath region. Figure 3.2 demonstrates an schematic view of the complex (dusty) plasma monolayer in the sheath region. In the sheath region the ions inside the plasma do not follow the Boltzmann distribution because of the highly non equilibrium situation. The repulsion between the dust particles and the ions, also the absorption of the ions by the lower electrode result in downstream focusing (cone like shape cf. [103, 104]) of ions. Therefore the pair interaction potential between the dust particles is anisotropic in 3D. The ion drift in the sheath region and deviating from the Boltzmann distribution is the source of different screening of the dust particles and consequently there exist a different pair interaction potential between the dust particles than a simple Yukawa interaction.

Kompaneets *et al.* [31] have derived an exhaustive model for obtaining the potential around the dust particles in the aforementioned situation. In [31], it is assumed that a test charge Q is immersed in a weakly ionized plasma. The potential of the test charge is due to the sum of the existing external field \mathbf{E}_0 and the plasma field where the latter is the solution of the Poisson equation. The ion density is also an input to the Poisson equation. The ion distribution function is obtained from a steady state kinetic equation which relates the ion-neutral mean free path l and the plasma electric field to the ion distribution function. A mobility limited ion drift is assumed which means that there exist a balance between acceleration of the ions in

the electric field and their collision to the neutrals. The plasma field is only due to the interaction with the test charge thus faraway from the test charge there exist only \mathbf{E}_0 and the considered temperature of the ions is field induced $T = eE_0l$ (The ions do not respond to the time variation of the electric field). The electron density is assumed to be homogeneous and not influenced by the test charge therefore the electrons do not play a role in screening. Basically when electron temperature is much higher than ion temperature $T_e \gg T_i$ the screening is only due to the ions. The complete derivation and assumption can be found in [31]. The Kompaneets potential around the dust particle in 3D (z is the perpendicular distance from the dust monolayer and r is the in-plane distance from the dust particle) in SI units is written as

$$\phi(r, z) = \frac{2Q_K}{4\pi^2\epsilon_0 l} \operatorname{Re} \int_0^\infty dt \frac{\exp[it(z/l)]}{1 + (l/\lambda_K)^2 Y(t)} K_0 \left(\frac{r}{l} \sqrt{\frac{t^2 + (l/\lambda_K)^2 X(t)}{1 + (l/\lambda_K)^2 Y(t)}} \right) \quad (3.3)$$

where K_0 is the zeroth order modified Bessel function of the second kind and l is the ion-neutral mean free path which shows the free path between two successive collision of an ion and a neutral gas particles. The functions $X(t)$ and $Y(t)$ are defined as

$$\begin{aligned} X(t) &= 1 - \sqrt{1 + it}, \\ Y(t) &= \frac{2\sqrt{1 + it}}{it} \int_0^1 \frac{d\alpha}{[1 + it(1 - \alpha^2)]^2} - \frac{1}{it(1 + it)}. \end{aligned} \quad (3.4)$$

What we are interested in is the pair interactions between particles, so the potential should be multiplied by Q_K to obtain the pair potential (energy). For having the in-plane part of the potential we consider $z = 0$. We normalize the potential (energy) by $k_B T$. We also normalize the distance r , by the mean interparticle distance in two dimensions $1/\sqrt{n}$ where n is the number density. Therefore $x = r\sqrt{n}$. We define a collision parameter as $\zeta = \lambda_K/l$ where $\lambda_K = \sqrt{\epsilon E_0 l / (e^2 n_i)}$ is a field-induced screening length. Therefore, the in-plane Kompaneets potential (energy) is defined as

$$\frac{U_K(x)}{k_B T} = \Gamma_K \frac{2\zeta\kappa_K}{\pi} \operatorname{Re} \int_0^\infty \frac{dt}{1 + \zeta^{-2} Y(t)} K_0 \left(x\zeta\kappa_K \sqrt{\frac{t^2 + \zeta^{-2} X(t)}{1 + \zeta^{-2} Y(t)}} \right), \quad (3.5)$$

where $\Gamma_K = Q_K^2 \sqrt{n} / (4\pi\epsilon k_B T)$ quantifies the interaction strength in terms of the effective charge Q_K and functions $X(t)$ and $Y(t)$ are defined in Eq. (3.4).

When $\zeta \rightarrow \infty$ the Kompaneets potential has the form

$$\lim_{\zeta \rightarrow \infty} \frac{U_K(x)}{k_B T} = \Gamma_K \frac{2\zeta\kappa_K}{\pi} \operatorname{Re} \int_0^\infty dt K_0(x\zeta\kappa_K t). \quad (3.6)$$

Due to the Bessel function normalization $1 = \frac{2}{\pi} \int_0^\infty K_0(y) dy$ [105] one concludes

$$\lim_{\zeta \rightarrow \infty} \frac{U_K(x)}{k_B T} = \frac{\Gamma_K}{x}. \quad (3.7)$$

Therefore, for every distance x when $\zeta \rightarrow \infty$ the Kompaneets potential would reduce to the Coulomb potential. The $\zeta \rightarrow \infty$ limit is due to the very small value of n_i or l or the very large value of E_0 . The same thing happens when $\kappa_K \rightarrow 0$ and ζ and is a finite number larger than zero. In that case $\zeta \gg \kappa_K$ and Eq. (3.7) holds again. The other case that Eq. (3.7) can hold is at very small separation when $x \rightarrow 0$ and ζ is a finite number larger than zero, therefore $\zeta \gg x$. In general one can write

$$\zeta \gg x\kappa_K : \quad \frac{U_K(x)}{k_B T} \rightarrow \frac{\Gamma_K}{x}. \quad (3.8)$$

For large particle separations and finite values of ζ , the Kompaneets potential reduces to its in-plane asymptotic form [96]

$$\left. \frac{U_K(x)}{k_B T} \right|_{x \rightarrow \infty} = \frac{\Gamma_K}{6\sqrt{2}\kappa_K^2 x^3} (60\zeta^2 - 1) + \mathcal{O}(x^{-4}). \quad (3.9)$$

The leading order asymptotic form of the anisotropic out-of-plane electrostatic potential is proportional to x^{-2} , and is given in Eq. (8) of Ref. [31] (in Gaussian units). Konopka *et al.* [30], have measured the interaction potential between two dust particles which are levitating in the sheath region for particle separation nearly equal to the mean geometrical distance ($x \approx 1$). They have shown that the interaction potential when $x \approx 1$ can be fitted by the Yukawa potential. In [31] it has been shown that the experimentally measured interaction potential can be equally well fitted by the Kompaneets potential in that region. However, the behavior of the Kompaneets and Yukawa potential is qualitatively different outside the distance range where experiments are performed. Therefore one can expect differences in collective behavior and transitions between the systems described by these two kinds of potentials.

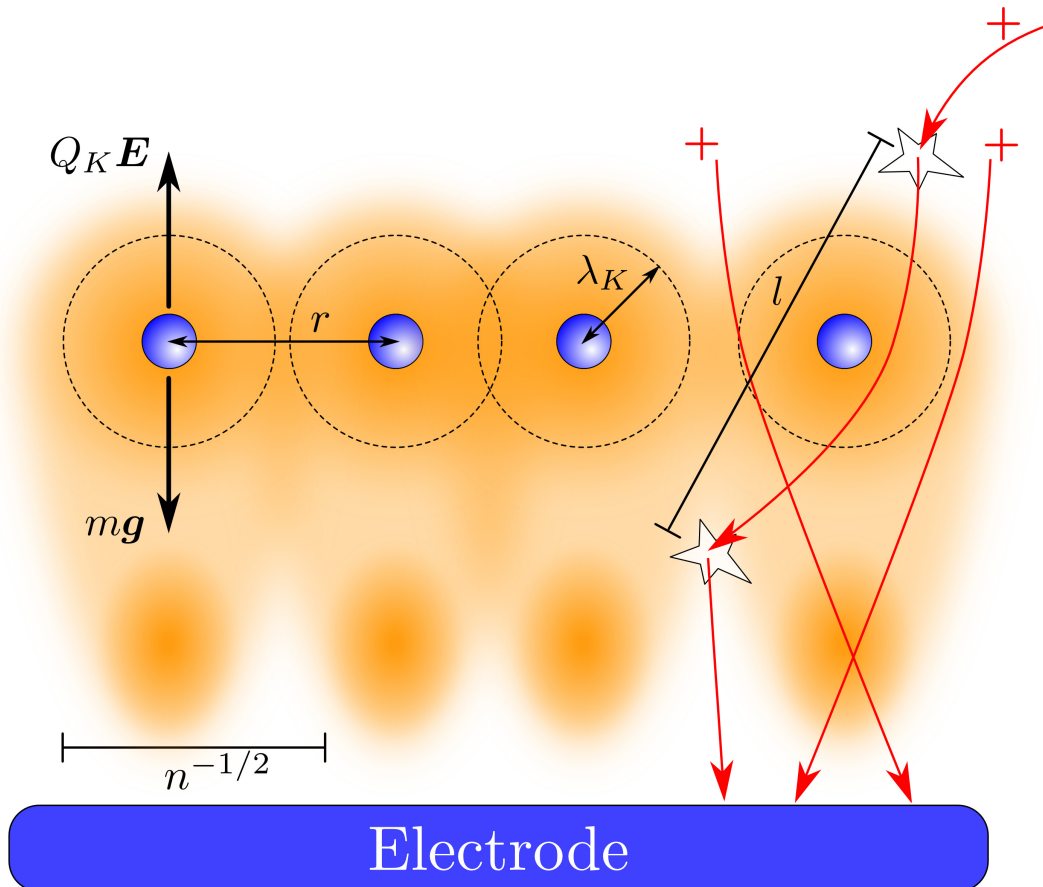


Figure 3.2.: Edge-on schematic of a dusty plasma monolayer. Negatively charged dust particles (blue filled circles) levitate in a well-defined 2D layer above an electrode in a radio frequency discharge plasma chamber, at a height where gravity is balanced by the vertical electrostatic force. The mean distribution of ions is color-coded in orange. Three characteristic ion trajectories are sketched by red arrows. Subsequent collisions between ions and neutral particles are separated on average by the ion-neutral mean free path l . Ions are focused in the downstream direction below the dust particles, giving rise to positive space-charges in the plasma wake region. The effective dust particle interactions are quantified by the three dimensionless parameters Γ_K , $\kappa_K = 1/(\lambda_K\sqrt{n})$, and $\zeta = \lambda_K/l$. This figure is produced by M. Heinen and taken from [96].

3.3. Structure Factor and Mode-Coupling Theory

We have summarized the equations we need to calculate the glass transition in three dimensions in the last chapter in section 2.2.1. The glass transition in two dimensions in mode coupling theory can be calculated via the same equations as in three dimensions

$$\frac{f_q}{1 - f_q} = \mathcal{F}_q(f), \quad (3.10)$$

with the difference that the MCT kernel in two dimensions for the hard sphere system is written as

$$\mathcal{F}_{q'}^{\text{HSS}}(f) = \frac{nS_{q'}}{8\pi^2 q'^4} \int d^2 k' S_{k'} S_{p'} (\mathbf{q}' \cdot \mathbf{k} c_{k'} + \mathbf{q}' \cdot \mathbf{p}' c_{p'})^2 f_{k'} f_{p'}, \quad (3.11)$$

with $\mathbf{p}' = \mathbf{q}' - \mathbf{k}'$. Here the difference with 3D is only the integration element. The integration element in 2D is $d^2 k / (2\pi)^2$, and in 3D is $d^3 k / (2\pi)^3$. Eq. (3.11) can be also written as

$$\begin{aligned} \mathcal{F}_{q'}^{\text{HSS}}(f) &= \frac{nS_{q'}}{8\pi^2 q'^4} \int_0^\infty dk' \int_{|k'-q'|}^{k'+q'} dp' k' p' S_{p'} S_{k'} \\ &\times \frac{[c_{k'}(q'^2 + k'^2 - p'^2) + c_p(q'^2 - k'^2 + p'^2)]^2}{[4q'^2 k'^2 - (q'^2 + k'^2 - p'^2)^2]^{1/2}} f_{k'} f_{p'}. \end{aligned} \quad (3.12)$$

In the hard-sphere system the dimension of the wave number q' , is the inverse length $[q'] = L^{-1}$. Also $[S_{q'}] = 1$, $[c_{q'}] = L^2$ and $[f_{q'}] = 1$. Therefore the dimension of $\mathcal{F}_{q'}^{\text{HSS}}$ is given as

$$[\mathcal{F}_{q'}^{\text{HSS}}] = [n]L^2 = 1. \quad (3.13)$$

This means that, $\mathcal{F}_{q'}^{\text{HSS}}$ is dimensionless. In our Yukawa or Kompaneets monolayer system, we have defined the distance in the unit of a length scale $1/\sqrt{n}$, thus the dimension of the wave number is

$$[q] = \frac{1}{L[\sqrt{n}]} = 1. \quad (3.14)$$

The memory kernel can be written as

$$\begin{aligned} \mathcal{F}_q(f) &= \frac{S_q}{8\pi^2 q^4} \int_0^\infty dk \int_{|k-q|}^{k+q} dp kp S_p S_k \\ &\times \frac{[c_k(q^2 + k^2 - p^2) + c_p(q^2 - k^2 + p^2)]^2}{[4q^2 k^2 - (q^2 + k^2 - p^2)^2]^{1/2}} f_k f_p, \end{aligned} \quad (3.15)$$

which is different from Eq. (3.12) by the fact that the number density does not appear explicitly behind the integrals. Here in Eq. (3.15), $S_q = 1/(1 - c_q)$ and $[c_q] = 1$, $[S_q] = 1$, $[f_q] = 1$ therefore $[\mathcal{F}_q] = 1$. One can discretize Eq. (3.15), on an equidistant grid using the middle point Riemann Sum. Here in the 2D system we choose to do the discretization over 200 points with the step size $\Delta = 0.2$. $q = \Delta\hat{q}$, $k = \Delta\hat{k}$ and $p = \Delta\hat{p}$ where $\hat{q}, \hat{k}, \hat{p} = 1/2, 3/2, 5/2, \dots, 399/2$. The minimum value of $q, k, p_{\min} = 0.1$ and the cut off value $q, k, p_{\max} = 39.9$ [78], therefore

$$\mathcal{F}_q(f) = \frac{S_q \Delta^2}{8\pi^2 \hat{q}^4} \sum_{\hat{k}, \hat{p}} S_k S_p \frac{\left[c_k (\hat{q}^2 + \hat{k}^2 - \hat{p}^2) + c_p (\hat{q}^2 - \hat{k}^2 + \hat{p}^2) \right]^2}{\left[4\hat{q}^2 \hat{k}^2 - (\hat{q}^2 + \hat{k}^2 - \hat{p}^2)^2 \right]^{1/2}} f_k f_p. \quad (3.16)$$

Here the sum over \hat{p} has the restriction that $|\hat{q} - \hat{k}| + 1/2 \leq \hat{p} \leq \hat{q} + \hat{k} + 1/2$ due to the integral limits in Eq. (3.15). From solving Eq. (3.10) and (3.16) together numerically we can obtain the f_q . The procedure of solving Eq. (3.10) is the same as in 3D which we have explained in section 2.2.1.

The Lamb-Mössbauer factor f_q^s is calculated in MCT with the same equation as in the 3D case,

$$\frac{f_q^s}{1 - f_q^s} = \mathcal{F}_q^s(f, f^s), \quad (3.17)$$

with the difference that the tagged particle kernel in 2D in our system can be written as [41]

$$\mathcal{F}_q^s(f, f^s) = \frac{1}{4\pi^2 q^4} \int d^2 k S_k (\mathbf{q} \cdot \mathbf{k})^2 c_k^2 f_k f_p^s. \quad (3.18)$$

with $\mathbf{p} = \mathbf{q} - \mathbf{k}$. Note that again the number density n , does not explicitly enter into Eq. (3.18), since all lengths and wave vectors are expressed in units of $1/\sqrt{n}$ and \sqrt{n} . In our notation the wave vector \mathbf{q} is the dimensionless Fourier conjugate variable to the dimensionless distance vector $\mathbf{x} = \mathbf{r}\sqrt{n}$. Eq. (3.18) can be written in bipolar coordinates

$$\mathcal{F}_q^s(f, f^s) = \frac{1}{4\pi^2 q^4} \int_0^\infty dk \int_{|k-q|}^{k+q} dp kp S_k \frac{[c_k^s (q^2 + k^2 - p^2)]^2}{[4q^2 k^2 - (q^2 + k^2 - p^2)^2]^{1/2}} f_k f_p^s. \quad (3.19)$$

This, using the same grid as in Eq. (3.16), can be discretized as

$$\mathcal{F}_q^s = \frac{\Delta^2}{4\pi^2 \hat{q}^4} \sum_{\hat{k}, \hat{p}} \hat{k} \hat{p} S_k \frac{\left[c_k^s (\hat{q}^2 + \hat{k}^2 - \hat{p}^2) \right]^2}{\left[4\hat{q}^2 \hat{k}^2 - (\hat{q}^2 + \hat{k}^2 - \hat{p}^2)^2 \right]^{1/2}} f_k f_p^s. \quad (3.20)$$

From solving Eq. (3.17) and (3.20) together numerically we can obtain the f_q^s . The procedure of solving Eq. (3.17) is the same as in 3D which we have explained in section 2.2.1.

The input to the MCT equations is the structure factor. In two dimensions the Ornstein-Zernike (OZ) equation can be written as [17]

$$\gamma(x) = \int d^2x' c(|\mathbf{x} - \mathbf{x}'|)h(x'), \quad (3.21)$$

where $h(x)$ is the total correlation function, $c(x)$ is the direct correlation function and $\gamma(x) = h(x) - c(x)$. The hypernetted-chain (HNC) closure can be written as

$$h(x) = \exp \left[-\frac{U(x)}{k_B T} + \gamma(x) \right] - 1, \quad (3.22)$$

where $U(x)$ is the interaction potential. OZ equation and HNC closure can be solved together. Replacing Eq. (3.21) in (3.24) will result in

$$\gamma(x) = \int d^2x' c(|\mathbf{x} - \mathbf{x}'|) \left(\exp \left[\gamma(x') - \frac{U(x')}{k_B T} \right] - 1 \right), \quad (3.23)$$

which is called the coupled OZ equation. This equation can be solved numerically. We use the same program written by M. Heinen to obtain the $c(x)$, $\gamma(x)$ and also S_q which is related to the the Fourier transform of total correlation function, h_q by $S_q = 1 + h_q$. The numerical procedure is described in detail in [97].

If one decides to write the HNC equation for a temperature $T' = T/2$ then the Eq. (3.24) can be written as

$$h(x) = \exp \left[-\frac{2U(x)}{k_B T} + \gamma(x) \right] - 1. \quad (3.24)$$

This is called the T/2-HNC closure. One can replace the T/2-HNC closure in the OZ equation and one has

$$\gamma(x) = \int d^2x' c(|\mathbf{x} - \mathbf{x}'|) \left(\exp \left[\gamma(x') - \frac{2U(x')}{k_B T} \right] - 1 \right). \quad (3.25)$$

Both Yukawa Eq. (3.2) and Kompaneets potential Eq. (3.5), contain of a prefactor Γ . The structure obtained from Eq. (3.25) for a Yukawa or Kompaneets potential with prefactor Γ_0 is exactly the same as the structure factor obtained from Eq. (3.23) for a Yukawa or Kompaneets potential with prefactor $\Gamma_0/2$. Therefore the structure

factors calculated via HNC closure represent the T/2-HNC structure factors with the half potential prefactor value and vice versa. For instance if we need to calculate the T/2-HNC structure factor for a Yukawa potential with $\Gamma = 300$ and $\kappa = 2$ we simply can solve the HNC closure for a Yukawa potential with $\Gamma = 600$ and $\kappa = 2$. It has been shown by [106], that the T/2-HNC matches the simulation data better than the HNC result, in their case for a binary dipole model in 2D.

Comparison between HNC, T/2-HNC and Monte Carlo simulation for Yukawa and Kompaneets potential is done by M. Heinen [96], see Fig. 3.3 and 3.4. Metropolis Monte Carlo (MC) simulations are done in the *NLT*-ensemble of constant particle number N , constant system area L^2 , and constant temperature T . A square simulation box with periodic boundary conditions in both Cartesian directions is used in the simulations, and the parameters $\Gamma_Y = 100$ and $\kappa_Y = 2.0$ for the Yukawa monolayer of $N = 10.000$ particles and $\Gamma_K = 300$, $\kappa_K = 2.0$, and $\zeta = 0.25$ for the Kompaneets monolayer of $N = 12.000$ particles, are chosen. Both simulated systems are strongly coupled equilibrium liquids not far from the crystal-liquid transition point. In the simulation, the direct particle interactions are truncated at a dimensionless cutoff radius of $x_c = r_c\sqrt{n} = 5$ in case of Yukawa interactions, and at $x_c = 12.5$ in case of Kompaneets interactions. For pair separations $x > x_c$, the pair-potential is set equal to zero in the simulations. Varying its numerical value, it is checked that the cutoff radius is large enough and does not have a significant effect on the measured quantity S_q .

From Fig. 3.3 and 3.4 we can conclude that HNC underestimates the first peak value of the structure factor of both Yukawa and Kompaneets in 2D. According to the figures these underestimation happens for both smaller κ value, e. g. $\kappa = 0.5$ and larger κ value e. g. $\kappa = 2.0$. The T/2-HNC also underestimates the first peak value in comparison to the MC simulation data. But T/2-HNC is an improvement over the HNC in predicting the first peak value of the structure factor. Since MCT is mostly concerned with the fluctuations with the wave length equal to the interparticle distances $x \approx 1$, the accuracy of MCT predictions mostly depends on the first peak values at $q \approx 2\pi$, of the structural input. T/2-HNC is far more accurate than HNC in predicting the first peak of S_q for the whole range of the small and large screening parameter κ . Therefore we decide to use the T/2-HNC structure factors for MCT calculations.

Although T/2-HNC is much better than HNC in terms of predicting the first peak value of the structure factor, it still underestimates the first peak value in comparison

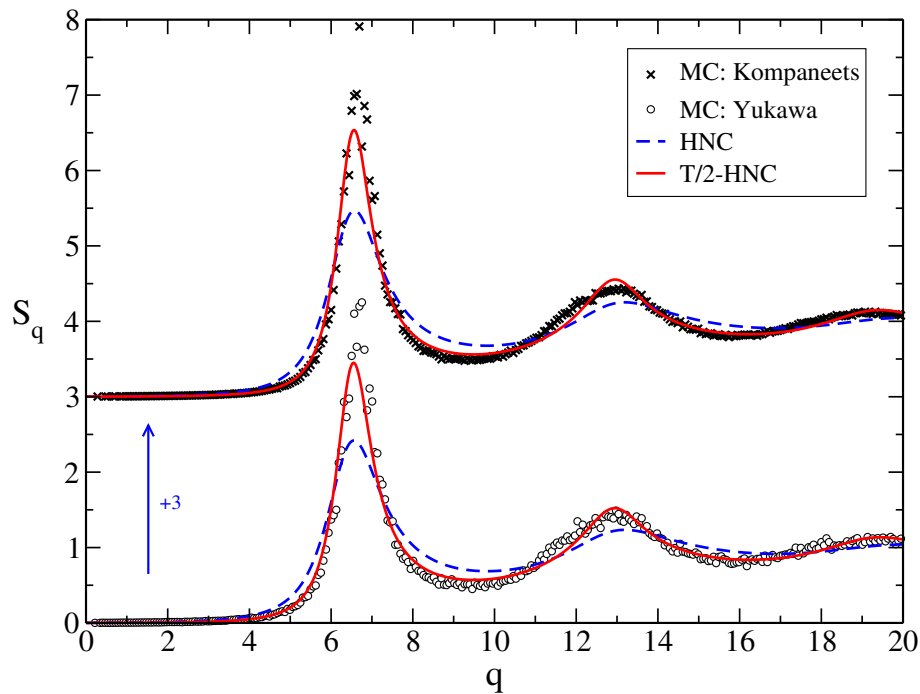


Figure 3.3.: Static structure factors for a Yukawa monolayer with $\Gamma_Y = 60$ and $\kappa_Y = 0.5$ (lower three data sets) and a Kompaneets monolayer with $\Gamma_K = 75$, $\kappa_K = 0.5$, and $\zeta = 0.25$ (upper three data sets). Crosses and circles: Monte Carlo simulation results. Blue dashed curves: HNC integral equation solution. Red solid curves: Solution of the T/2-HNC in Eq. (3.25). The Kompaneets monolayer structure factors are shifted by 3 units along the vertical axis for clarity. All data in this plot is provided by M. Heinen.

to the MC simulation result. Moreover the approximation of the structural input will be combined by the approximations inside the MCT equation later and these combined uncertainty is not easy to be calculated. Although we are aware of this uncertainty in the transition values, we expect that the transition curves behavior should be at least qualitatively correct.

3.4. Results

3.4.1. Glass Transition Diagrams

We numerically calculate the glass transition points as it is described in section 3.3 for the Yukawa monolayer and Kompaneets monolayer, using Eq. (3.10), (3.16) and the T/2-HNC structure factor. The result is shown in the κ_Y and Γ_Y plane for Yukawa monolayer and κ_K and Γ_K plane for Kompaneets monolayer in Fig. 3.5. The Kom-

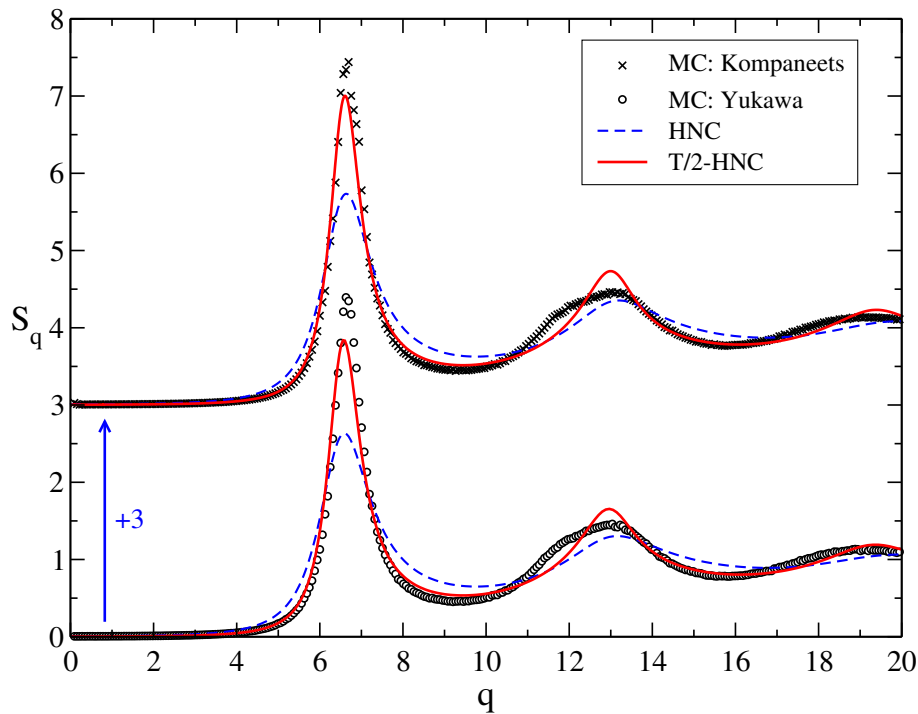


Figure 3.4.: Static structure factors for a Yukawa monolayer with $\Gamma_Y = 100$ and $\kappa_Y = 2.0$ (lower three data sets) and a Kompaneets monolayer with $\Gamma_K = 300$, $\kappa_K = 2.0$, and $\zeta = 0.25$ (upper three data sets). Crosses and circles: Monte Carlo simulation results. Blue dashed curves: HNC integral equation solution. Red solid curves: Solution of the T/2-HNC in Eq. (3.25). The Kompaneets monolayer structure factors are shifted by 3 units along the vertical axis for clarity. All data in this plot is provided by M. Heinen.

paneets transition points are shown for three different values of $\zeta = 0.25, 0.375, 0.5$. We show the Yukawa transition curve in the experimentally available range [107] of the Yukawa screening parameter $0.05 < \kappa_Y < 3$ and we choose the same range for κ_K . In the one-component-plasma (OCP) limit, which is the limit $\kappa_Y, \kappa_K \rightarrow 0$, all the glass transition curves approach the same value $\Gamma_Y = \Gamma_K = 138.5$. This value corresponds to the smallest screening parameter, $\kappa = 0.05$, which we have investigated. The fact that all the glass transition curves approach the same value in the OCP limit is due to the fact that the Yukawa and Kompaneets potentials both will reduce to the bare coulomb potential in that limit (see Eq. (3.2) and (3.8)).

While the glass transition curves are qualitatively similar for the Yukawa and the Kompaneets systems, the transition occurs at higher values of the coupling parameter in case of the Kompaneets monolayer. For decreasing values of the parameter ζ , the differences between the Yukawa and Kompaneets glass transition curves are increasing. As we discuss in the next subsection (see also Fig. 3.6), the deviation

of the Kompaneets potential from the Yukawa-like form drastically increases as ζ decreases. Here we go back to look at the complete picture which leads to Kompaneets interaction between particles; considering ions, neutrals and the external electric field E_0 which holds the point particles (dusts) against gravity. The distribution of ions is what is responsible for screening. In Figure 3.5, for a chosen value of κ e.g. $\kappa = 2.0$, a smaller ζ , corresponds to a larger value of l . For larger values of l , the ion can speed up due to the external field before a collision with a neutral. This makes the non-equilibrium condition stronger and also will result in a non-equilibrium distribution of ions, which in the end through its effect on the potential results in a higher Γ value necessary for the transition.

On the other hand, in the limit $\zeta \rightarrow \infty$, the Kompaneets potential tends to the Coulomb form (see Eq. (3.7)). Therefore for very large values of κ , the Kompaneets transition curve in the κ_K and Γ_K plane will be a straight horizontal line starting from $\Gamma_K = 138.5$.

As we discussed in the last chapter, in 3D the glass transition curve and melting curve of the Yukawa system have the same behavior in the κ and Γ plane, and are parallel to each other. Here we want to compare the Yukawa transition curve with the melting curve from [107]. Hartmann et al. [107] have shown that there exists good agreement between their simulation result for the melting transition of a 2D Yukawa layer with the function

$$\Gamma = \frac{\tilde{\Gamma}^*}{1 + f'_2 \tilde{\kappa}^2 + f'_3 \tilde{\kappa}^3 + f'_4 \tilde{\kappa}^4}, \quad (3.26)$$

where $f'_2 = 0.388$, $f'_3 = 0.138$, $f'_4 = 0.0138$ and $\tilde{\Gamma}^* = 131$. They have scaled the distance with the WignerSeitz radius $a = 1/\sqrt{\pi n}$ where n is the number density. For mapping the function in Eq. (3.26) to our κ and Γ plane, we need to take into account the different length scale, which results in $\tilde{\kappa} = \kappa/\sqrt{\pi}$. In our κ and Γ plane

$$\Gamma = \frac{\Gamma^*}{1 + f_2 \kappa^2 + f_3 \kappa^3 + f_4 \kappa^4}, \quad (3.27)$$

where $f_2 = -0.1235$, $f_3 = 0.0248$ and $f_4 = -0.0014$ and $\Gamma^* = 131/\sqrt{\pi} = 73.9$. The function in Eq. (3.27) is shown in Fig. 3.5 with the dashed curve in violet. One can notice that there exist a similarity between the T/2-HNC-MCT Yukawa monolayer glass transition and the melting curve.

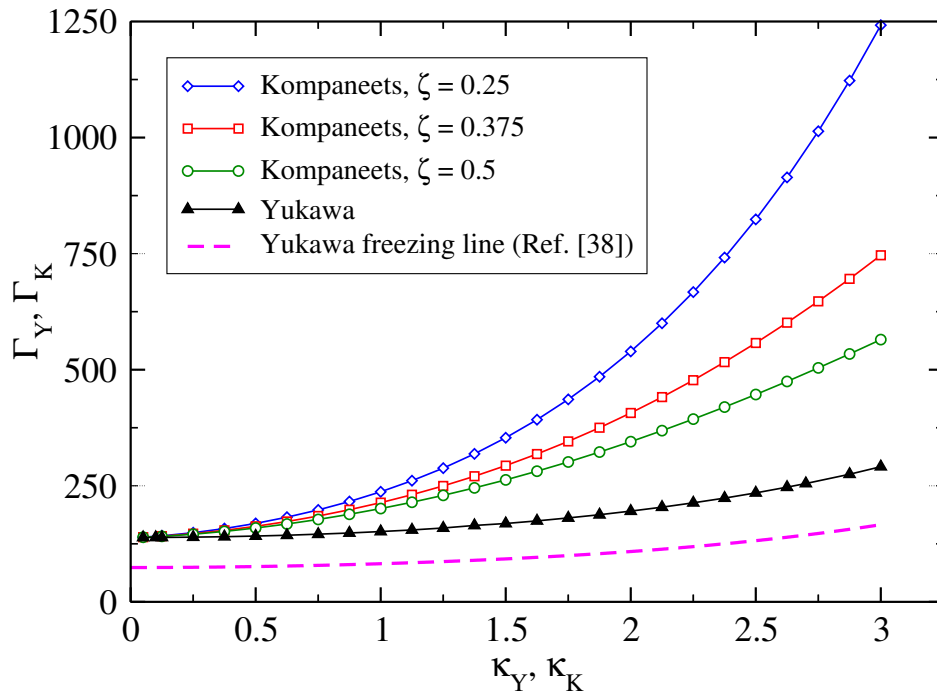


Figure 3.5.: Glass transition curves in the (κ, Γ) -plane, for the Yukawa potential (black curve with triangles) and three different Kompaneets potentials with parameters $\zeta = 0.25$ (solid curves with diamonds), $\zeta = 0.375$ (solid curve with squares) and $\zeta = 0.5$ (solid curve with circles). The dashed curve is the 2D Yukawa freezing line from Ref. [107].

3.4.2. Potentials and Structure Factors at the Transitions

The Kompaneets potentials for different values of ζ and the Yukawa monolayer potential are shown in Fig. 3.6.

The potentials are shown for $\kappa_Y = \kappa_K = 2.0$ and the glass transition Γ value which is specified in the figure caption. From Eq. (3.9) one can see that the Kompaneets potential has the $1/x^3$ asymptotic for large x . In Fig. 3.6 the vertical axis shows $xU(x)/k_B T$, which implies that the potential is multiplied by x , therefore the large x asymptotic has the behavior x^{-2} as we have shown in the figure with the dotted line. The structure factors at the transition points for $\kappa_Y = \kappa_K = 2.0$ are shown in the inset figure and one can notice that despite the differences between the potentials the structure factors coincide.

In Fig. 3.7 we have shown representative structure factors of the Yukawa monolayer along the Yukawa glass transition curve in Fig. 3.5. One can observe that along the glass transition curve the structure factors are falling on top of each other and no differences are visible. The first peak height of the structure factors varies between

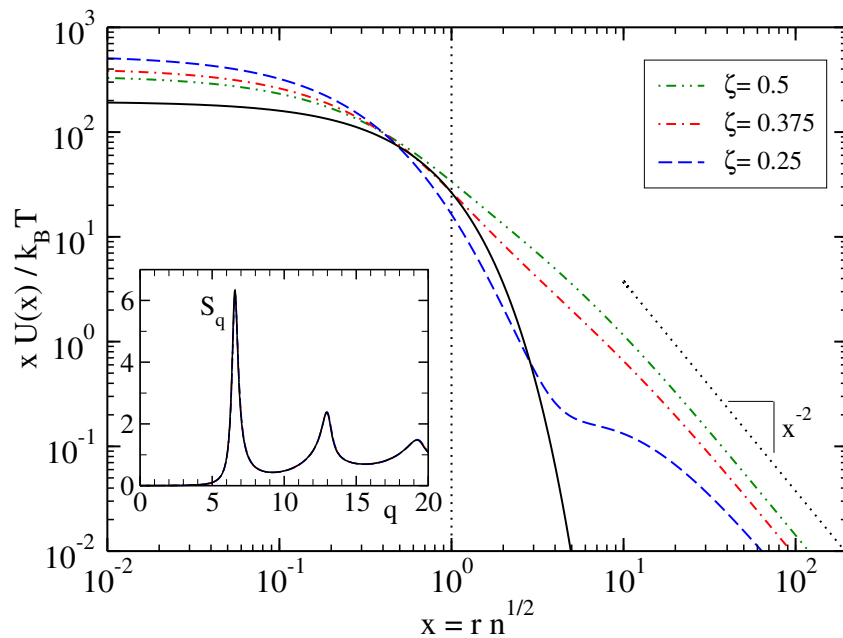


Figure 3.6.: Effective pair-potentials for $\kappa_Y = \kappa_K = 2.0$, for values of Γ_Y and Γ_K at the liquid-glass transition point. Solid curve: Yukawa potential for $\Gamma_Y = 195.4$. Dashed, dot-dashed and dot-dot-dashed curves: Kompaneets potentials for $\zeta = 0.25, 0.375$ and 0.5 , and $\Gamma_K = 539.4, 406.8$ and 345.0 , respectively. All potentials are multiplied by their argument, $x = r\sqrt{n}$, to expose the differences. The inset features the corresponding static structure factors S_q in the T/2-HNC approximation. All four functions S_q are overlapping on the scale of the inset. The principal peak heights of the structure factors are $S_q = 6.33$ for the Yukawa system, and $S_q = 6.26, 6.23$ and 6.19 for the Kompaneets systems with $\zeta = 0.5, 0.375$ and 0.25 , respectively.

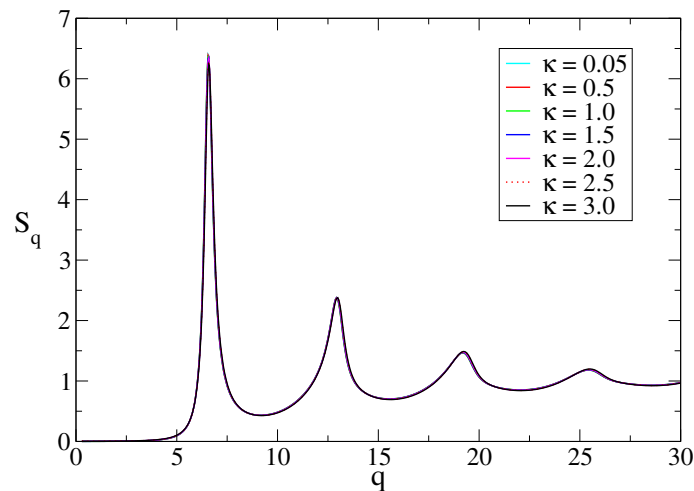


Figure 3.7.: The structure factor of the Yukawa monolayer along the glass transition curve in Fig. 3.5. The κ_Y values are specified in the legend. The correspondent Γ_Y values at the transition are $(\kappa_Y, \Gamma_Y) = (0.05, 138.7), (0.5, 141.7), (1, 151.4), (1.5, 168.7), (2, 195.4), (2.5, 234.7), (3.0, 291.1)$. The first peak height of the structures factors varies between $S_q = 6.39$ for $(\kappa_Y, \Gamma_Y) = (0.05, 138.7)$ and $S_q = 6.24$ for $(\kappa_Y, \Gamma_Y) = (3.0, 291.1)$.

$S_q = 6.39$ for $(\kappa_Y, \Gamma_Y) = (0.05, 138.7)$ and $S_q = 6.24$ for $(\kappa_Y, \Gamma_Y) = (3.0, 291.1)$ which is not sensible on the scale of our figure. This means that the MCT equations also trace the curve in the parameters plane which every transition point of that curve corresponds to the same structure factor. Mathematically speaking, the Yukawa monolayer glass transition curve in the κ and Γ plane is a locus of a transition point which has the structure factor with the exact shape shown in Fig. 3.7.

3.4.3. A Fallacious Re-entrant State Sequence

As we have mentioned in section 3.1 and 3.2, the 2D Yukawa potential is mostly a simplified model of the interactions which exist in the monolayer of charged particles experiments. For modeling the interaction the Kompaneets interaction is more realistic. In this section we explain one of the possible consequences. We show that the liquid-glass transition of a system with Kompaneets-like pair potential appears as a non-monotonic curve (corresponding to liquid-glass-liquid state re-entrance) when it is plotted in terms of the inappropriate parameters of the Yukawa potentials that represent a best fit to the actual (Kompaneets) potential around the mean geometric distance $x = r\sqrt{n} = 1$.

In Fig. 3.8 we plot the Yukawa glass transition curve that is also shown in Fig. 3.5 (black curves with triangles). The 2D Yukawa freezing line, reproduced from Ref. [107], is also shown (dashed line) to allow a better comparison to the glass transition line than on the scale of Fig. 3.5. The curve with open squares in Fig. 3.8 is generated as follows: For given values of the two Yukawa parameters κ_Y and Γ_Y , we calculate the Kompaneets potential that fits best the Yukawa potential in the distance range $0.7 < x < 3$ which is most frequently sampled by the particles [30]. The fit is conducted as follows: For given values of l and n , which yield the combination $\zeta\kappa_K \equiv (l\sqrt{n})^{-1}$ ($\simeq 0.354$ for the example shown in the figure), we tune the two remaining, independent Kompaneets parameters κ_K and Γ_K ; an optimal fit is achieved by minimizing the square deviation $\int_{0.7}^3 dx [U_Y(x) - U_K(x)]^2$ between the two potentials. We then calculate S_q for the best-fitting Kompaneets potential in the T/2-HNC scheme, and use it as the input to the MCT equations (3.10) and (3.16) for f_q . If $f_q = 0$, the system is classified as liquid, and if $f_q > 0$, it is classified to be in the glassy state. We repeat the full procedure for various Yukawa parameters κ_Y and Γ_Y , which are tuned by interval bisection, until we find for each κ_Y the smallest (critical) value of Γ_Y at which the best-fitting Kompaneets system vitrifies.

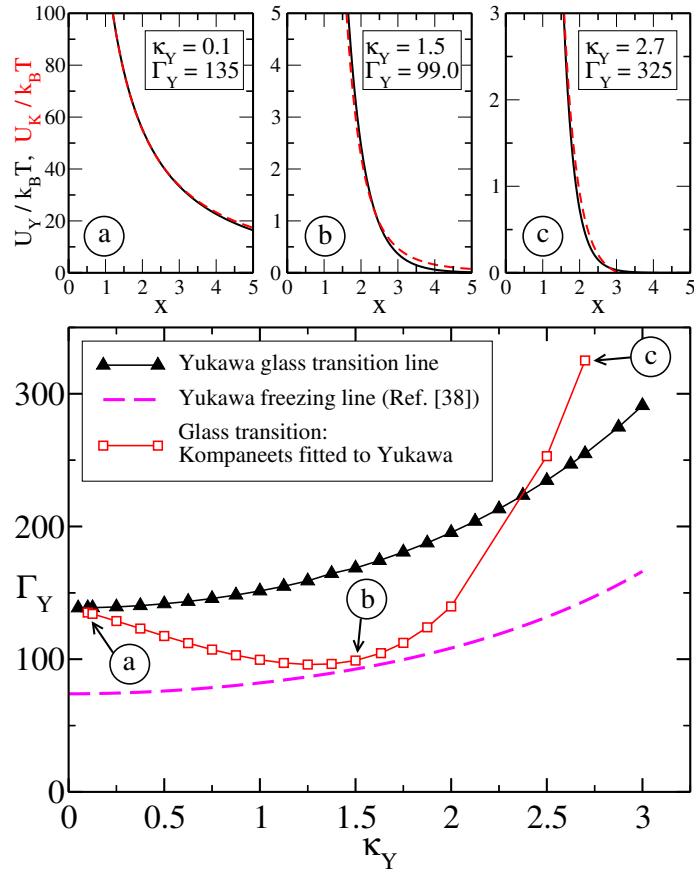


Figure 3.8.: Lower panel: Kompaneets and Yukawa glass transitions in the Yukawa parameter plane. The curve with triangles: Yukawa glass transition curve in the Yukawa screening- and coupling-parameter (κ_Y, Γ_Y)-plane. The curve with squares is the glass transition curve for Kompaneets pair-potentials which have been optimally fitted to the corresponding Yukawa potential in the region $0.7 < x < 3$, by pointwise tuning of the Kompaneets screening parameter κ_K and coupling parameter Γ_K . The parameters $l = 2.3$ mm and $n = 1.5$ mm⁻² are held fixed for the Kompaneets potential. The dashed curve is the 2D Yukawa freezing line from Ref. [107]. Upper panels (a), (b) and (c): representative Yukawa potentials and the best fitting Kompaneets potentials as described in the text, along the Kompaneets glass transition curve. The dashed curves show the best fitting Kompaneets potentials and the solid curves are the Yukawa potential interactions. Both potentials are plotted against the mean geometric distance $x = r\sqrt{n}$ [96].

Thus, the curve with open squares in Fig. 3.8 is the glass transition curve of a dusty plasma monolayer with Kompaneets-like interactions, as it would appear when plotted in terms of the dimensionless parameters κ_Y and Γ_Y of the Yukawa potentials that best fit the actual Kompaneets potential around the mean geometric distance, where the potential is directly accessible [30]. Therefore, if one observes vitrification in a dusty plasma monolayer and assumes Yukawa-like interactions in the experiment analysis, the transition behavior may be misinterpreted as a re-entrant liquid-glass-liquid state sequence, while the transition diagram in terms of the three relevant Kompaneets potential parameters does not exhibit any re-entrance (see Fig. 3.5).

3.4.4. Nonergodicity Parameters

Representative form factors (nonergodicity parameters) of Yukawa and Kompaneets monolayers at the transition are shown in Fig. 3.9. The existence of the non vanishing form factor for all the q values smaller than the cut off value in the glassy state is due to the fact that the glassy state is resilient to the rearrangement of the particles in any length scale which is required for the relaxation of the density fluctuations. Same as in the 3D case, the form factor has a maximum at $q = 2\pi$ which represents the density fluctuations with the wavelength equal to the mean interparticle distance would survive the most in the system. For relaxation of those fluctuations, rearrangements of particles in the order of the mean particle distance are needed which do not take place because of cage effect. The $q = 2\pi$ is also the wave number which corresponds to the structure factor first peak position.

In both Yukawa and Kompaneets monolayers when $\kappa \rightarrow 0$, the Coulombic potential (OCP limit) is revisited, cf. Eq. (3.2) and (3.8). In the OCP limit, as we discussed in more detail for the 3D case in section 2.3.3, zero compressibility makes it impossible to create a long wave length (small q) fluctuation in the glassy system. Therefore an assumed initial long wave length fluctuation in the glassy state relaxes back to equilibrium. This is the reason that the form factor vanishes in the OCP limit for both Kompaneets and Yukawa potential when $q \rightarrow 0$. In Fig. 3.9, it is visible that when $\kappa_Y = \kappa_K = 0.05$ the form factor is nearly approaching zero, while for $\kappa_Y = \kappa_K = 2.0$ the form factor is approaching a finite value at small q .

We showed in section 2.3.3 that the small q behavior of the f_q in the OCP limit is proportional to the small q behavior of the structure factor. The small q behavior of the structure factor can be obtained starting from the long range asymptotic of the

direct correlation function $c(x)$. In most of the closure relations for the Ornstein-Zernike equation such as HNC, the long range asymptotic of the direct correlation function is obtained from $c(x) = -U(x)/k_B T$ [17, 108]. However for the T/2-HNC one can obtain the asymptotic as follows. Taking the natural logarithm of the both side of the Eq. (3.24) and replacing $h(r) = g(r) - 1$ leads to

$$c(x) + \frac{2U(x)}{k_B T} = g(x) - \ln g(x) - 1. \quad (3.28)$$

Using the Taylor expansion of $\ln g(x)$ around $g(x) = 1$, $\ln g(x) = (g(x) - 1) - (g(x) - 1)^2/2 + \dots$, one can write Eq. (3.28) as

$$c(x) = -\frac{2U(x)}{k_B T} + \frac{h^2(x)}{2} + \dots \quad (3.29)$$

Therefore one can write the large x asymptotic of direct correlation function in T/2-HNC as

$$c(x) = -\frac{2U(x)}{k_B T}. \quad (3.30)$$

Taking the Fourier transform of Eq. (3.30) when $U(x)/k_B T = \Gamma/x$ (Coulomb potential) in 2D results in

$$c_q = -\frac{2U(q)}{k_B T} = -\frac{4\pi\Gamma}{q}. \quad (3.31)$$

Thus through $S_q = (1 - c_q)^{-1}$,

$$S_q = \frac{q}{4\pi\Gamma}. \quad (3.32)$$

Therefore, in case of the Coulomb potential the structure factor meets zero with a linear behavior at $q \rightarrow 0$. Since in that case the form factor is proportional to S_q in the small q region (see section 2.3.3), the form factor approaches zero linearly. In the 3D case, the structure factor and the f_q also approach zero in the small q region, but they approach zero with q^2 behavior.

In Fig. 3.9, we present the f_q of the Yukawa and Kompaneets when $\kappa_Y = \kappa_K = 0.05$. In that limit, the f_q of the two potentials are indistinguishable on the scale of the figure. Using Eq. (3.30) and the Fourier transform of the Yukawa potential in two dimensions we have the asymptotic of the T/2-HNC direct correlation function of the Yukawa monolayer as

$$c_q \approx -\frac{2U_Y(q)}{k_B T} = -\frac{4\pi\Gamma_Y}{\sqrt{\kappa_Y^2 + q^2}} \quad \text{for } q + q_t \gg \kappa_Y^2 + q^2. \quad (3.33)$$

that is, when both the wavenumber q and the screening parameter κ_Y are small and

within a certain ratio of each other. In Eq. (3.33), q_t is a dimensionless non-negative threshold wavenumber with a typical value of $q_t \sim 0.1$. For more information about the condition $q + q_t \gg \kappa_Y^2 + q^2$ see Ref. [96]. When $\kappa_Y \rightarrow 0$, the Eq. (3.33) reduces to (3.31). In Fig. 3.10 we have shown the T/2-HNC structure factors of the Yukawa monolayer at the transition for different κ_Y . When $\kappa_Y = 0.05$ the small q behavior of the structure factor appears approximately linear.

Here we want to calculate the small q behavior of f_q in 2D. The 2D-MCT kernel in Eq. (3.15) can be written also as

$$\mathcal{F}_q(f) = \frac{1}{4\pi^2} \int d^2k V(\mathbf{q}, \mathbf{k}, \mathbf{p}) f_k f_p, \quad (3.34)$$

where $V(\mathbf{q}, \mathbf{k}, \mathbf{p})$ is written the same as in 3D case in Eq. (2.44):

$$V(\mathbf{q}, \mathbf{k}, \mathbf{p}) = \frac{1}{2} \frac{S_q S_k S_p}{q^4} [\mathbf{q} \cdot \mathbf{k} c_k + \mathbf{q} \cdot (\mathbf{q} - \mathbf{k}) c_{|\mathbf{q}-\mathbf{k}|}]^2. \quad (3.35)$$

We follow the same method as we discussed in the 3D case to evaluate the small q behavior of $\mathcal{F}_q(f)$. We Taylor expand the $c_p = c_{|\mathbf{q}-\mathbf{k}|}$ as in Eq. (2.46) and replace the expansion in Eq. (3.35) where we end up with Eq. (2.47). For obtaining the term in $\mathcal{F}_q(f)$ which is only proportional to S_q and does not have any other q dependence, we replace the a^2 term from Eq. (2.47) in Eq. (3.34):

$$\begin{aligned} \mathcal{F}_{S_q}(f) &= \frac{S_q}{8\pi^2} \int_0^\infty dk k S_k^2 f_k^2 \int_0^{2\pi} \frac{q^4}{q^4} (c_k^2 + 2k c_k c'_k \cos^2 \theta + k^2 c_k'^2 \cos^4 \theta) d\theta \\ &= \frac{S_q}{4\pi} \int_0^\infty dk k S_k^2 \left(c_k^2 + k c_k c'_k + \frac{3}{8} k^2 c_k'^2 \right) f_k^2. \end{aligned} \quad (3.36)$$

The term which is proportional to $q S_q$ in $\mathcal{F}_q(f)$ is obtained from replacing the $2bc$ term from Eq. (2.47) inside Eq. (3.34). This term vanishes since the integrals of odd powers of the $\cos \theta$ for $\int_0^{2\pi} d\theta$, are zero.

The term which is proportional to $q^2 S_q$ is calculated from substitution of the b^2

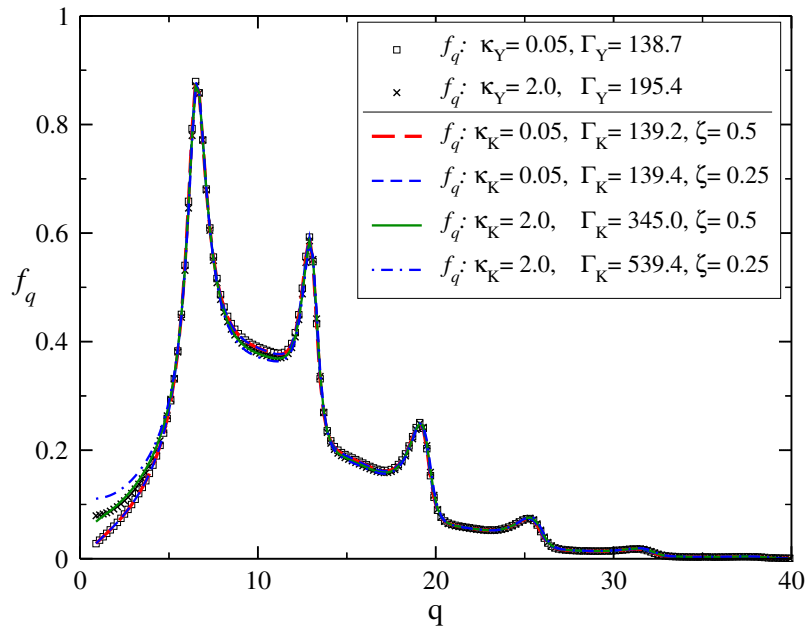


Figure 3.9.: The form factors f_q (non-monotonic functions of q) for various Yukawa monolayers (symbols) and Kompaneets monolayers (curves) at their respective MCT glass transition points, with potential parameters as indicated in the legend.

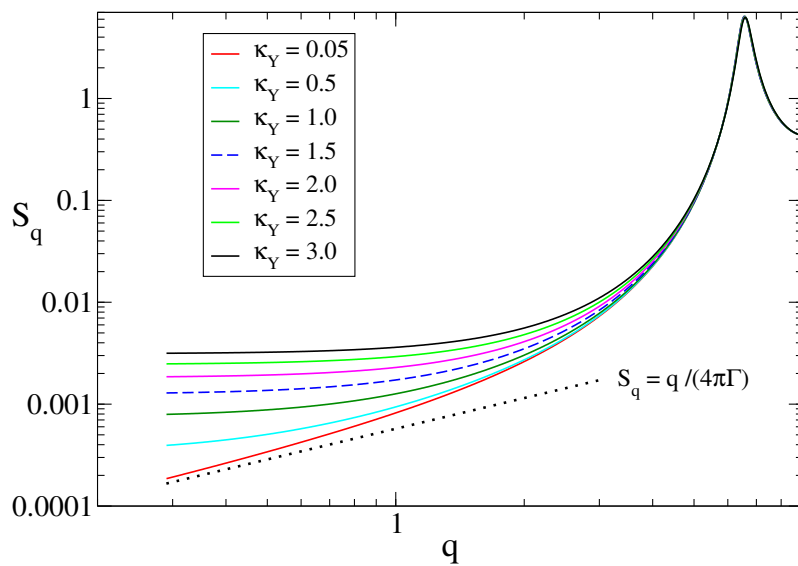


Figure 3.10.: The small q behavior of the structure factor of the Yukawa monolayer along the glass transition curve in Fig. 3.5. The κ_Y values are specified in the legend. The corresponding Γ_Y values at the transition are $(\kappa_Y, \Gamma_Y) = (0.05, 138.7), (0.5, 141.7), (1, 151.4), (1.5, 168.7), (2, 195.4), (2.5, 234.7), (3.0, 291.1)$. The dotted line in black shows how a linear dependence of q would look like, in the logarithmic scale. The dotted black line follows the relation $q/(4\pi\Gamma)$ with $\Gamma = 138.7$, which is the small q dependence of OCP-2D, if we assume the transition Γ of OCP is equal to the transition Γ of the Yukawa system with $\kappa = 0.05$.

and $2ac$ from Eq. (2.47) in Eq. (3.34):

$$\begin{aligned}
\mathcal{F}_{q^2 S_q}(f_k) &= \frac{q^2 S_q}{8\pi^2} \int_0^\infty dk k S_k^2 f_k^2 \int_0^{2\pi} (c_k'^2 \cos^2 \theta + \frac{1}{4} k^2 c_k'' \cos^6 \theta + k c_k' c_k'' \cos^4 \theta \\
&\quad + c_k c_k'' \cos^2 \theta + \frac{1}{3} k c_k c_k''' \cos^4 \theta + k c_k' c_k'' \cos^4 \theta + \frac{1}{3} k^2 c_k' c_k''' \cos^6 \theta) d(\cos \theta) \\
&= \frac{q^2 S_q}{8\pi} \int_0^\infty dk k S_k^2 \left(c_k'^2 + \frac{5}{32} k^2 c_k''^2 + \frac{3}{2} k c_k' c_k'' + c_k c_k'' + \right. \\
&\quad \left. \frac{1}{4} k c_k c_k''' + \frac{5}{24} k^2 c_k' c_k''' \right) f_k^2.
\end{aligned} \tag{3.37}$$

In summary, in the small q region in 2D

$$\mathcal{F}_q = (\alpha + \beta q^2 + \dots) S_q \tag{3.38}$$

with

$$\alpha = \frac{1}{4\pi} \int dk k S_k^2 \left(c_k^2 + k c_k c_k' + \frac{3}{8} k^2 c_k'^2 \right) f_k^2 \tag{3.39}$$

and

$$\beta = \frac{1}{8\pi} \int dk k S_k^2 \left(c_k'^2 + \frac{5}{32} k^2 c_k''^2 + \frac{3}{2} k c_k' c_k'' + c_k c_k'' + \frac{1}{4} k c_k c_k''' + \frac{5}{24} k^2 c_k' c_k''' \right) f_k^2. \tag{3.40}$$

Considering only the leading order of the approximation in Eq. (3.38), and also considering Eq. (3.33) where $S_q = (1 - c_q)^{-1}$, the small- q , small- κ_Y limiting behavior of the Yukawa monolayer form factor, is given by

$$f_q = \alpha \left[1 + \alpha + \frac{4\pi\Gamma_Y}{\sqrt{\kappa_Y^2 + q^2}} \right]^{-1} \quad \text{for } q + q_t \gg \kappa_Y^2 + q^2, \tag{3.41}$$

in the T/2-HNC approximation. For finite κ_Y , the function f_q in Eq. (3.41) assumes a positive value for $q = 0$, and increases $\propto q^2$ when $q \rightarrow 0$. Only in the OCP limit $\kappa_Y = 0$, the function f_q in Eq. (3.41) vanishes for $q = 0$, and increases initially as $\propto q$. In a broad scale, the f_q asymptotic for $\kappa_Y = 0.05$ and $\Gamma_Y = 138.7$ is almost linear.

Note here that the small- q limiting OCP form factor is qualitatively different in two and three dimensions. In 3D, the function f_q vanishes in the OCP limit $\kappa_Y = 0$ as $\propto q^2$. In 2D, it vanishes linearly.

We calculate numerically the Lamb-Mössbauer factor f_q^s , using Eq. (3.17) and (3.20) and the T/2-HNC structure factor. The f_q^s for the Yukawa monolayer at $(\kappa_Y, \Gamma_Y) = (0.05, 138, 7)$ and $(2, 195.4)$ is shown in Fig. (3.11). The f_q^s of the Kompaneets monolayer for $(\kappa_K, \Gamma_K, \zeta) = (0.05, 139.2, 0.5)$ and $(2, 345.0, 0.5)$ are also presented in Fig. (3.11). The parameter values are all at the transition. One can observe that there exists no small q suppression in the Lamb-Mössbauer factor in the OCP limit, which is expected since there exist no S_q dependence in $\mathcal{F}_q^s(f)$ (see Eq. (3.18)). In fact all the Lamb-Mössbauer factors of Kompaneets and Yukawa monolayer fall on top of each other at the transition.

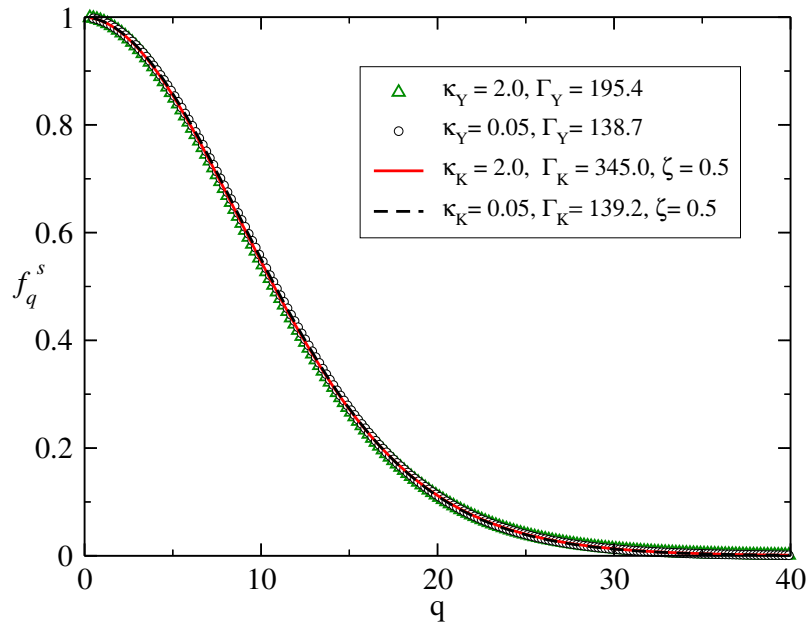


Figure 3.11.: The Lamb-Mössbauer factors f_q^s (monotonically decaying as functions of q) for various Yukawa monolayers (symbols) and Kompaneets monolayers (curves) at their respective MCT glass transition points, with potential parameters as indicated in the legend.

Chapter 4

Modification of a Liquid State Structure Factor to Create a Jammed State Structure Factor

It has been shown by large scale simulations that the long wave length behavior of the structure factor in a jammed state is suppressed [45–48] in comparison to what the liquid state theories predict [17]. In liquid state theory ¹, the static structure factor in a hard sphere or soft sphere (short range soft potential) system, is predicted to behave as $S(k) \simeq S(0) + \alpha k^2$ where $S(0)$ is proportional to the compressibility. In contrast, the simulation shows that in nearly jammed packings of hard or soft spheres [45, 46] the structure factor has a linear relation with wave number, $S(k) \propto k$ at small k and would reach a very small or possibly zero value at $k = 0$. For the large scale simulation of the jammed state, Silbert *et al.* [46] have used the harmonic short range potential of the form

$$\frac{U(r)}{k_B T} = \begin{cases} \Gamma(1-r)^2, & r \leq 1 \\ 0, & r > 1, \end{cases} \quad (4.1)$$

where 1 is the particle diameter, and Γ is a temperature dependent constant. They have found the linear relation $S(k) \propto k$ at small k for the structure factor of a jammed state. As we show later in this chapter, liquid state theory predicts the behavior $S(k) \simeq S(0) + \alpha k^2$ for the same potential Eq. (4.1). Using the effects of long range potentials, we try to modify the structure factor resulting from the liquid

¹by liquid state theory we mean different closures and approximations [17] which exist for solving the Ornstein-Zernike Integral equation to obtain the structure factor.

state theory in a way that it matches the simulation result in the small k regime.

4.1. Small Wave Number Dependence of the Structure Factors of the Long Range $1/r^n$ Potentials

One can calculate the structure factor of a system of particles interacting via the potential in Eq. (4.1) using the HNC approximation. In the simulation the jamming temperature is considered very low so the Γ should be very large. For the HNC calculation we have chosen $\Gamma = 500$. The HNC structure factors are presented in Fig. 4.1 for different values of the packing fraction. The HNC result in the small k regime is not compatible with the simulation result for the jammed system [46], since $S(k)$ approaches a constant value with k^2 behavior for every packing fraction. Here we want to find a way to reproduce the simulation results in the small k regime using liquid state theory.

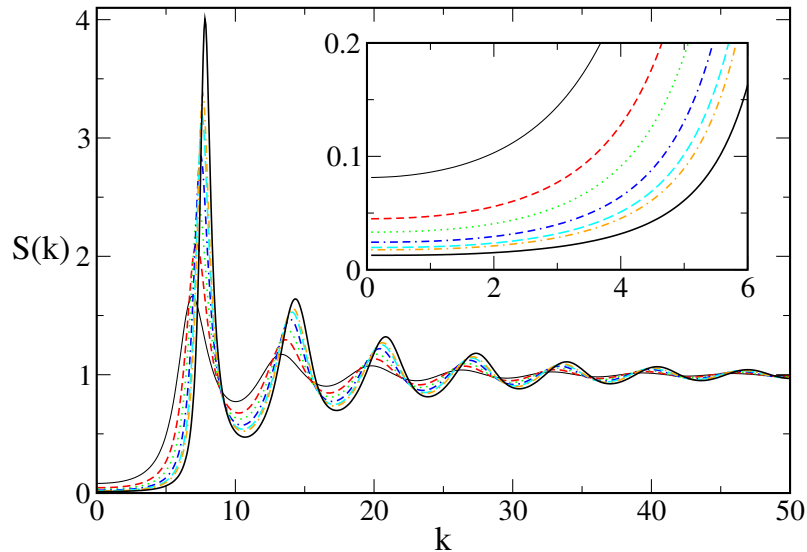


Figure 4.1.: Static structure factor $S(k)$ calculated via HNC for a monodisperse system of soft spheres with the harmonic potential in Eq. (4.1). The inset shows how the compressibility, $\chi_T \propto S(0)$, decreases with increasing φ , but with all curves following the standard: $S(k \rightarrow 0) \simeq S(0) + \alpha k^2$ form. The packing fractions are 0.4, 0.5, 0.55, 0.6, 0.633316, 0.65, 0.7 respectively from top to bottom.

As we discussed in section 2.3.3, in a Coulombic potential system which is a very long range potential, the structure factor approaches zero with the behavior $S(k) \propto k^2$ which leads to vanishing compressibility. Nixon *et al.* [49] have argued before that the behavior $S(k) \propto k$ is equivalent to a long range decay in the correlation function, $h(r) = 1/r^4$. Considering that, one may assume, longer range potentials

can have the effect of suppressing the structure factor in the small wave number regime.

In order to investigate the last assumption we consider a long range potential in the form

$$V(r) = 1/r^n. \quad (4.2)$$

The small k behavior of $c(k) \simeq -\beta V(k)$ [108] can be obtained by taking the Fourier transform of the potential. When $n = 1$ we have the familiar case of the Coulombic potential which we discussed in 2.3.3 as the OCP limit of Yukawa potential. Following Eq. (2.38) to Eq. (2.40) leads to $S(k) \simeq \frac{\beta}{4\pi} k^2$ for the $n = 1$.

When $n = 2$, using Eq. (2.37), the Fourier transform of the potential $1/r^2$ can be written as

$$V(k) = \frac{4\pi}{k} \int_0^\infty \frac{\sin kr}{r} dr. \quad (4.3)$$

The integral does not converge absolutely but has a removable pole and results in $c(k) \simeq -\beta V(k) = -2\beta\pi^2/k$. This together with Eq. (2.39) would result in linear behavior in the small k regime in the structure factor

$$S(k) \simeq \frac{k}{2\beta\pi^2}. \quad (4.4)$$

For $n = 3, 4, 5, \dots$ (when n is integer and $n > 2$) the integral $V(k) = \frac{4\pi}{k} \int_0^\infty \frac{\sin kr}{r^{n-1}} dr$ does not converge, since the Cauchy principal value of the integral is ∞ . For this case one can define a small positive non integer ϵ , and calculate the integral for the potential $1/r^{n-\epsilon}$ (see Appendix B)

$$V(k) = \frac{4\pi}{k} \int_0^\infty \frac{\sin kr}{r^{n-1-\epsilon}} dr = -4\pi \sin\left(\frac{n-2-\epsilon}{2}\pi\right) \Gamma(2-n+\epsilon) k^{n-3-\epsilon} \quad (4.5)$$

where $\Gamma(s) = \int_0^\infty \exp(-y)y^{s-1} dy$. This has been derived in a similar way in [49], but one should consider that when n is integer and $n > 2$ one cannot put $\epsilon = 0$ since the Γ function would result in ∞ . From Eq. (4.5) one has $c(k) \simeq \alpha k^{n-3-\epsilon}$ so

$$S(k) \simeq \frac{1}{1 - \alpha k^{n-3-\epsilon}} \simeq 1 + \alpha k^{n-3-\epsilon}. \quad (4.6)$$

If there exists a short range potential, $c_{sr}(r) = c(r) - c_{lr}(r)$ where $c_{lr}(k) \simeq \alpha k^{n-3-\epsilon}$ then

$$S(k) \simeq \frac{1}{1 - c_{sr}(0) - \alpha k^{n-3-\epsilon}} \simeq S(0) + \alpha k^{n-3-\epsilon}. \quad (4.7)$$

This means for $n=4$, $S(k)$ has an approximately linear behavior (not completely linear due to the fact that $\epsilon \neq 0$) in the small k domain. Also, it approaches a non-zero constant $S(0)$ at $k = 0$.

4.2. The Effects of an Additional $1/r^2$ Potential

What we can conclude from the last section is that, considering a potential $\propto 1/r^2$ prompts a structure factor which linearly approaches zero $S(k \rightarrow 0) \propto k$. For introducing the linear behavior into the HNC structure factor of the potential (4.1), we use an additional potential γ/r^2 . We propose a potential of the form

$$\begin{aligned} \frac{V(r)}{k_B T} &= \Gamma(1-r)^2 + \frac{\gamma}{r^2} & r \leq 1 \\ \frac{V(r)}{k_B T} &= \frac{\gamma}{r^2} & r > 1 \end{aligned} \quad (4.8)$$

and solve the Ornstein-Zernike equation with HNC closure numerically for this potential. For $\Gamma = 500$ and different packing fractions we have shown the structure factor for $\gamma = 1$ and $\gamma = 10$ in Figures 4.2 and 4.3 respectively. One can detect that adding the potential γ/r^2 to the harmonic potential resulted in linear behavior in small k region for all the different values of packing fractions. Comparison between the two figures also shows us that apparently the linear behavior of the structure factor lasts until higher k , when $\gamma = 10$. Another observation is that increasing γ , increases the height of the structure factor first peak for every packing fraction.

In Fig. 4.4 We have presented the HNC structure factor of the proposed potential in Eq. (4.8) for $\Gamma = 500$, packing fraction 0.64 and different values of $1 \leq \gamma \leq 12$. When γ is between 8 and 10 the structure factor is comparably consistent with simulation data for the same packing fraction taken from [46].

In a jammed state (unlike a liquid) all the particles start to correlate with each other therefore it resembles a continuum matter. In a continuum matter in three dimensions the stress resulting from a small fluctuation will propagate through the system with $1/r^2$ dependence, since a perturbation is propagating as a spherical wave with a wavefront (surface) $\propto r^2$. The energy transfer to a particle due to a stress field is proportional to the stress multiplied by the particle volume. On this ground, introducing a potential energy $= \gamma/r^2$, as an effect of the emergence of the jammed state, is logical.

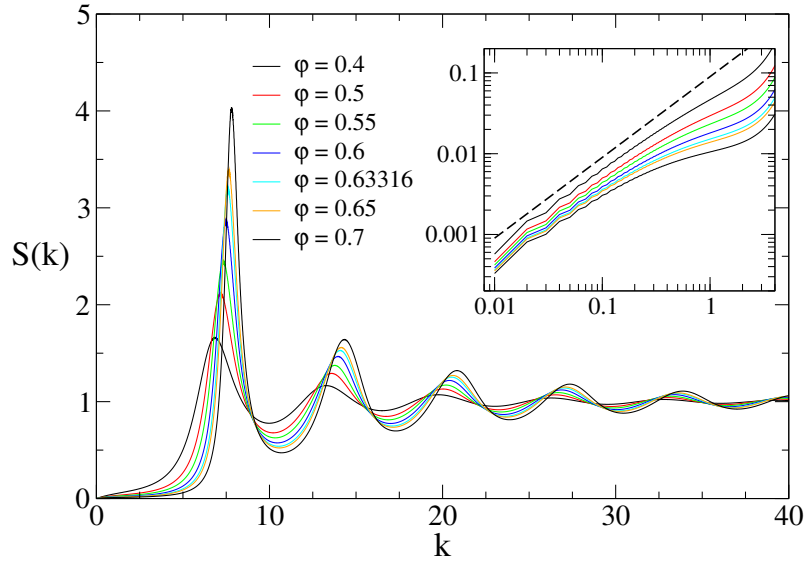


Figure 4.2.: HNC structure factor of the proposed potential in Eq. (4.8), for different values of packing fractions when $\Gamma = 500$ and $\gamma = 1$. The inset shows the $S(k)$ in the small k region. The dashed line shows a linear relation between $S(k)$ and k .

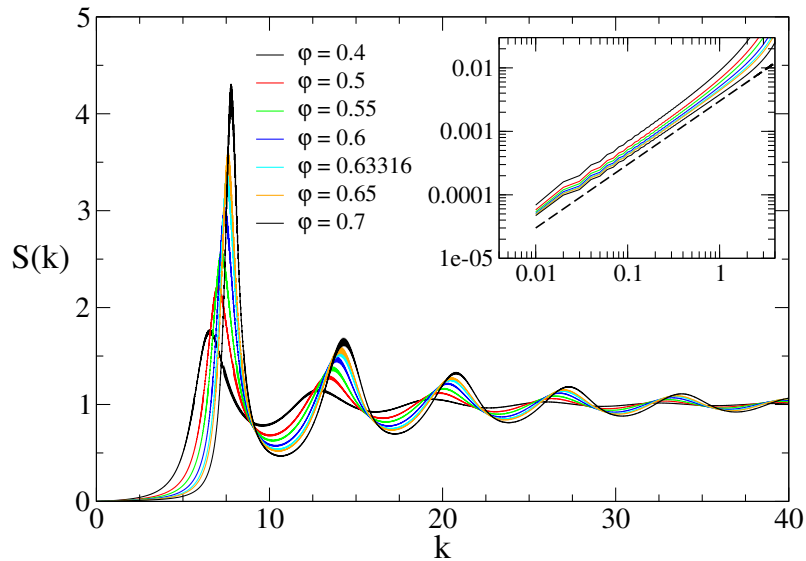


Figure 4.3.: HNC structure factor of the proposed potential in Eq. (4.8), for different values of packing fractions when $\Gamma = 500$ and $\gamma = 10$. The inset shows the $S(k)$ in the small k region. The dashed line shows a linear relation between $S(k)$ and k .

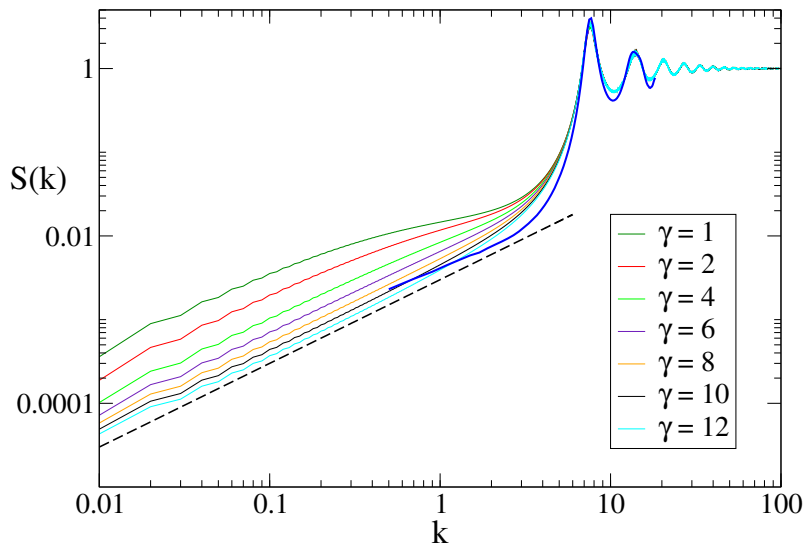


Figure 4.4.: HNC structure factor of the proposed potential in Eq. (4.8), for different values of γ , packing fraction of 0.64 and $\Gamma = 500$. The simulation data, shown in blue, is produced by L. E. Silbert [46]. The dashed line shows a linear relation between $S(k)$ and k .

4.3. A Random Phase Approximation

We can also use the γ/r^2 potential as a perturbation. We assume a system interacting via a short range potential mentioned in Eq. (4.1) (reference system) and a perturbative longer range potential $u(r)/k_B T = \gamma/r^2$. The structure factor of the whole system $S(\mathbf{k})$ is defined as a density response of the system to a weak external potential in Fourier space [17]

$$\delta n(\mathbf{k}) = -n S(\mathbf{k}) \frac{\phi(\mathbf{k})}{k_B T}, \quad (4.9)$$

where $\delta n(\mathbf{k})$ is the Fourier transform of the deviation of the particle density from its mean value $\delta n(\mathbf{r}) = n(\mathbf{r}) - n$ and $\phi(\mathbf{r})$ is a small external potential. If $\phi(\mathbf{r})$ is an external potential to the reference system plus the perturbative long range potential, the external potential $\phi_0(\mathbf{r})$ to the reference system will be [109]

$$\phi_0(\mathbf{r}) = \phi(\mathbf{r}) + \int u(\mathbf{r} - \mathbf{r}') \delta n(\mathbf{r}') d\mathbf{r}', \quad (4.10)$$

where

$$\delta n(\mathbf{k}) = -n S_0(\mathbf{k}) \frac{\phi_0(\mathbf{k})}{k_B T}. \quad (4.11)$$

$\phi_0(\mathbf{k})$ is the Fourier transform of $\phi_0(\mathbf{r})$ and $S_0(\mathbf{k})$ is the structure factor of the reference system. From Eq. (4.9), (4.11) and the Fourier transform of Eq. (4.10), $\phi_0(\mathbf{k}) = \phi(\mathbf{k}) + u(\mathbf{k})\delta n(\mathbf{k})$, one has

$$S(k) = \frac{S_0(k)}{1 + nS_0(k)\beta u(k)}, \quad (4.12)$$

where $S(k)$ is the total structure factor. We have calculated the $S_0(k)$ within HNC approximation considering Eq. (4.1) as the potential, and then used Eq. (4.12) to calculate $S(k)$. The result is shown in Fig. 4.5. For small k values, the perturbative potential $u(r) = \gamma/r^2$ with $\gamma = 8.289$ can reproduce the simulation data. But this method would fail clearly for stronger perturbations. As we expect the perturbation γ/r^2 should only rise in large r or small k regions, but in smaller r or large k having an $1/r^2$ interaction cannot be physically reasonable and creates a large amount of perturbation which affects $S(k)$ in the way that the peak values drop significantly, Fig. 4.5. Therefore we decide to limit the perturbation γ/r^2 only to small k by altering $u(k) = 2\pi^2\gamma/k$, the Fourier transform of $u(r) = \gamma/r^2$, to

$$u'(k) = 2\pi^2\gamma \frac{\exp(-ak^2)}{k}. \quad (4.13)$$

The Gaussian term distributes the $1/k$ interactions normally on k . We again use Eq. (4.12) to calculate $S(k)$, this time for $u'(k)$. The $S_0(k)$ is calculated via HNC for the reference system interacting with the potential in Eq. (4.1). The result is shown in Fig. 4.6 for different Γ and corresponding a values. In r -space, $u'(r)$ can be obtained from Fourier transforming back the $u'(k)$ in three dimensions:

$$u'(r) = \frac{\gamma}{\sqrt{a}} \frac{D_+(\frac{r}{2\sqrt{a}})}{r}, \quad (4.14)$$

where $D_+(x) = \exp(-x^2) \int_0^x \exp(y^2)dy$ is called Dawson function [110]. We plot the $u'(r)$ in Fig. 4.7. In small r region, $u'(r)$ can be fitted by a Gaussian function, where at large r it can be fitted by γ/r^2 . At small r , one can think of the energy localized in the particle-particle contact by the Gaussian term, whereas at large r , there exists the $1/r^2$ 'collective' property. The corresponding pair correlation functions $g(r)$, of the structure factors represented in Fig. 4.6, are shown in Fig. 4.8.

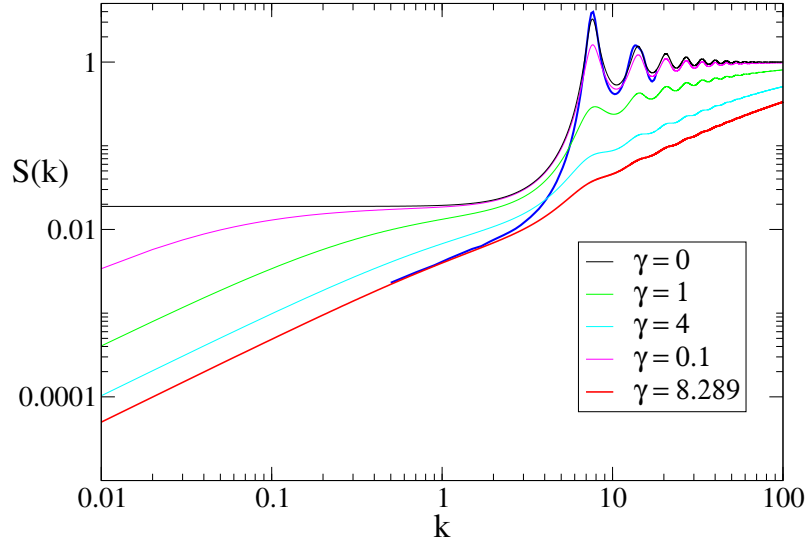


Figure 4.5.: Structure factors calculated via Eq. (4.12) for different values of γ and packing fraction of 0.64 and $\Gamma = 500$. The simulation data shown with the solid blue curve is produced by L. E. Silbert [46].

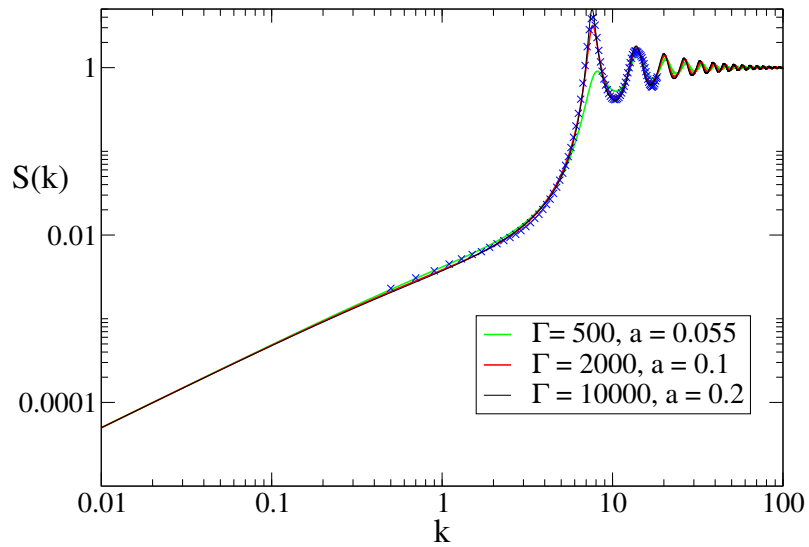


Figure 4.6.: Structure factors calculated via Eq. (4.12), taking $u'(k)$ in Eq. (4.13) as the long range potential, for different values of Γ and a . Packing fraction is taken 0.64 and $\gamma = 8.289$. The simulation data shown with \times is produced by L. E. Silbert [46].

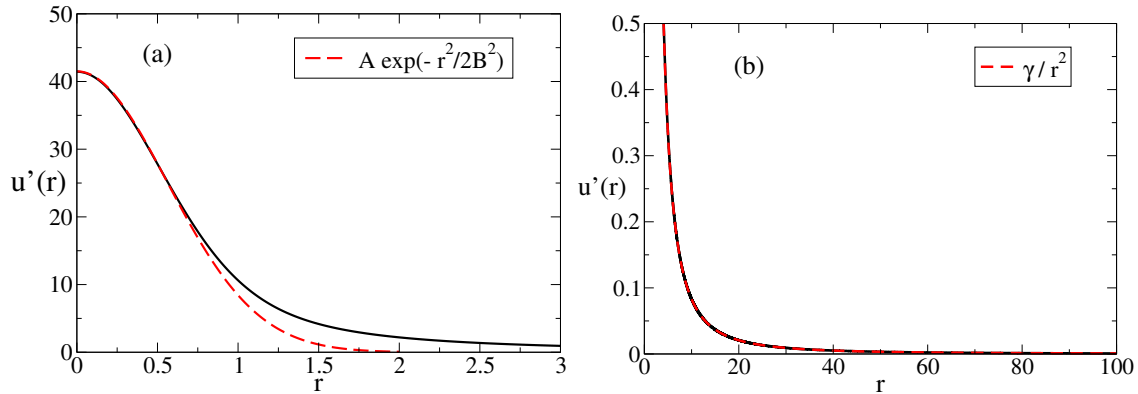


Figure 4.7.: The potential $u'(r) = \frac{\gamma}{\sqrt{a}} D_+(\frac{r}{2\sqrt{a}})/r$ with $\gamma = 8.289$ and $a = 0.1$, (a) in small r region and (b) in large r region. The potential behaves like a Gaussian, at small r , whereas at large r it behaves like $1/r^2$. The dashed red curve in (a) shows a Gaussian function of the form $A \exp(-r^2/2B^2)$ with $A = \gamma/2a$ and $B = 0.56$ which fits the potential $u'(r)$ at small r very well. The dashed red curve in (b) corresponds to the function γ/r^2 , which shows very well the behavior of the $u'(r)$ at large r .

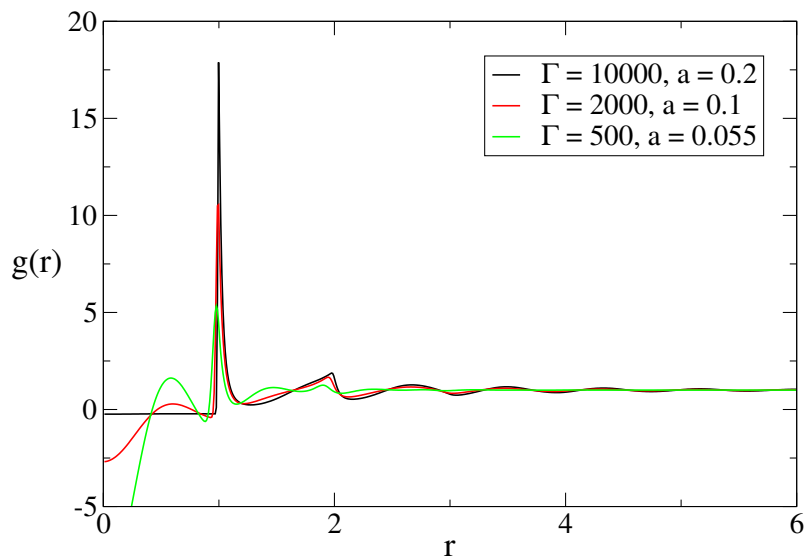


Figure 4.8.: Pair correlation functions calculated with $u'(k)$ via Eq. (4.12) for the Γ and a values presented in Fig. 4.6. Packing fraction is taken equal to 0.64 and $\gamma = 8.289$.

4.4. Conclusion and Outlook

In conclusion the HNC and other familiar closures in liquid state theory together with the Ornstein-Zernike equation produce the $S(k \rightarrow 0) \simeq S(0) + \alpha k^2$ behavior in the structure for short range hard or soft sphere potentials like Eq. (4.1). In the simulation for the same potential [46], the behavior of the structure factor is rather different at small k values $S(k \rightarrow 0) \propto k$. We used two methods to introduce the behavior $S(k \rightarrow 0) \propto k$ into the HNC results. Both of these two methods are based on using a weak long range potential (γ/r^2) to bring the linear behavior near zero, into the structural results. In the first method we have simply solved the HNC and Ornstein-Zernike equation for the sum of the short range and long range potential in Eq. (4.8). In the second method we used the localized long range potential in Eq. (4.13) and (4.14) as a perturbation to the HNC structure result of the short range potential system. Although the second method seems to be better in reproducing the small k behavior in Fig. 4.6, the first method is better for keeping the expected height of the first peak of the structure factor. One should also have in mind that in the simulation the linear behavior in structure arises as one approaches the jammed state therefore it indicates the emergence of the jammed state. In contrary when we add the long range potential γ/r^2 , it will create a linear behavior in every packing fraction, cf. Fig. 4.3. One should be able to modulate γ with the packing fraction, in a way that in the packing fractions below the jammed state $\gamma = 0$ and therefore the linear behavior vanishes.

If our assumption is true that the γ/r^2 resulting from the spherical propagation of a perturbation at the jammed state is creating the linear behavior in the structure factor, one can expect that since in two dimensions the wavefront of the propagation is a circle, the potential γ/r should create the linear behavior in 2D. The Fourier transform of the potential γ/r in 2D can be written as

$$V(k) = 2\pi \int_0^\infty dr r \frac{\gamma}{r} J_0(kr) = \frac{2\pi\gamma}{k}. \quad (4.15)$$

This result in the behavior $c(k) \simeq -2\pi\gamma\beta/k$ in the small k regime. Using the Ornstein-Zernike equation will lead to

$$S(k) \simeq \frac{k}{2\pi\gamma}. \quad (4.16)$$

Therefore, the structure factor should have a linear behavior in 2D, after introducing

the γ/r potential. In the future after checking the validity of this assumption, one should be able to establish a one to one fit between simulation result and theory for every Γ and packing fraction value in both two and three dimensions.

Chapter 5

Dynamics of Brownian Particles with Velocity-Dependent Friction

5.1. Nonlinear Langevin Equation

The motion of ordinary Brownian particles can be described by the Langevin equation [51]

$$\frac{d\mathbf{p}_i}{dt} = \mathbf{F}_i - \gamma_0 \mathbf{p}_i + \boldsymbol{\xi} R_i(t), \quad (5.1)$$

where γ_0 is a constant friction. The interaction of the Brownian particle with the solvent molecules is taken into account by a rapidly fluctuating force, $\boldsymbol{\xi} R_i(t)$ with an ensemble average equal to zero

$$\langle R_i(t) \rangle = 0. \quad (5.2)$$

The fluctuation force is a Gaussian white noise [111] which means the values that the noise can take are Gaussian distributed but uncorrelated in time

$$\langle \boldsymbol{\xi} R_i(t) \boldsymbol{\xi} R_j(t') \rangle = \xi^2 \delta_{ij} \delta(t - t'). \quad (5.3)$$

Here ξ^2 is the fluctuation strength. In Eq. (5.1), $\mathbf{F}_i = -\frac{\partial}{\partial \mathbf{r}_i} U(\{\mathbf{r}_i\})$ is the interaction force or the outcome potential force inserted on particle i from other Brownian particles. The diffusion in the velocity space is determined by the random force and defined as $D_v = \xi^2/2m^2$. So when $m = 1$ then $D_v = \xi^2/2$.

One way of describing the motion of Brownian particles with additional energy

input or so-called activity is assuming a velocity dependent friction in the Langevin equation [55]

$$\frac{d\mathbf{p}_i}{dt} = \mathbf{F}_i - \gamma(\mathbf{v}_i)\mathbf{p}_i + \boldsymbol{\xi}R_i(t). \quad (5.4)$$

The velocity dependent friction $\gamma(\mathbf{v}_i)$, allows negative values of friction in some regions in the phase space. When friction is negative, the $-\gamma(\mathbf{v}_i)\mathbf{p}_i$ force instead of dissipating the energy, pumps an additional mechanical energy into the system. The fluctuating force $\boldsymbol{\xi}R_i(t)$, follows Eq. (5.2) and (5.3).

5.2. Time Evolution Operators

For deriving the mode coupling equation of motion in case of ordinary Brownian particle, the Smoluchowski time evolution operator has been used before [24]. In the Smoluchowski or diffusive time scale the momentum coordinate of the Brownian particle has been relaxed to the equilibrium and therefore the time evolution operators involve only the position coordinates of the Brownian particles. The Smoluchowski operator also has been used for study of the shear effect on the dense colloidal suspensions [64]. Here we want to derive the time evolution operators involving both momentum \mathbf{p}_i and position \mathbf{r}_i coordinates of the Brownian particles. The Liouville equation for a phase variable $A(\boldsymbol{\Gamma}) = A(\mathbf{r}_1, \mathbf{r}_2, \dots, \mathbf{r}_N, \mathbf{p}_1, \mathbf{p}_2, \dots, \mathbf{p}_N)$ is defined as [59]

$$\frac{dA(\boldsymbol{\Gamma})}{dt} = i\mathcal{L}A(\boldsymbol{\Gamma}), \quad (5.5)$$

and for a non-equilibrium distribution f , the time evolution equation is considered as

$$\frac{\partial f(\boldsymbol{\Gamma}, t)}{\partial t} = -i\mathcal{L}^\dagger f(\boldsymbol{\Gamma}, t). \quad (5.6)$$

In these two equations $i\mathcal{L}$ and $i\mathcal{L}^\dagger$ are the time evolution operators for phase variables and distribution function, respectively. Using Eq. (5.4) we can derive the time evolution operators

$$\begin{aligned} i\mathcal{L} = \dot{\boldsymbol{\Gamma}} \cdot \frac{\partial}{\partial \boldsymbol{\Gamma}} &= \sum_i \left(\frac{\mathbf{p}_i}{m} \cdot \frac{\partial}{\partial \mathbf{r}_i} + \mathbf{F}_i \cdot \frac{\partial}{\partial \mathbf{p}_i} \right) \\ &+ \sum_i \left(\boldsymbol{\xi}R_i(t) \cdot \frac{\partial}{\partial \mathbf{p}_i} - \frac{\gamma(\mathbf{v}_i)}{m} \mathbf{p}_i \cdot \frac{\partial}{\partial \mathbf{p}_i} \right), \end{aligned} \quad (5.7)$$

and

$$\begin{aligned}
-i\mathcal{L}^\dagger &= -\dot{\Gamma} \cdot \frac{\partial}{\partial \Gamma} - \left(\frac{\partial}{\partial \Gamma} \cdot \dot{\Gamma} \right) = \sum_i \left(-\frac{\mathbf{p}_i}{m} \cdot \frac{\partial}{\partial \mathbf{r}_i} - \mathbf{F}_i \cdot \frac{\partial}{\partial \mathbf{p}_i} \right) \\
&\quad + \sum_i \left(-\boldsymbol{\xi} R_i(t) \cdot \frac{\partial}{\partial \mathbf{p}_i} + \frac{\gamma(\mathbf{v}_i)}{m} \mathbf{p}_i \cdot \frac{\partial}{\partial \mathbf{p}_i} \right) \\
&\quad + \sum_i \left(\frac{1}{m} \frac{\partial \gamma(\mathbf{v}_i)}{\partial \mathbf{p}_i} \cdot \mathbf{p}_i + \frac{\gamma(\mathbf{v}_i)}{m} \right).
\end{aligned} \tag{5.8}$$

Both time evolution operators $i\mathcal{L}$ and $i\mathcal{L}^\dagger$ contain the term $\boldsymbol{\xi} R_i(t) \cdot \frac{\partial}{\partial \mathbf{p}_i}$. Since $\boldsymbol{\xi} R_i(t)$ is an stochastic force, the time evolution, would be different for every realization. Thus we need to take an average over the noise. We follow the averaging procedure in [112]: We assume $\frac{dB(\Gamma(t))}{dt} = i\mathcal{L}_1 B(\Gamma(t)) = -\boldsymbol{\xi} R_i(t) \cdot \frac{\partial}{\partial \mathbf{p}_i} B(\Gamma(t))$ therefore

$$B(t + \Delta t) - B(t) = \int_t^{t+\Delta t} i\mathcal{L}_1 B(t_1) dt_1. \tag{5.9}$$

We substitute B from Eq. (5.9) inside itself and drop B from both side of the equation

$$\begin{aligned}
-\boldsymbol{\xi} R_i(t) \cdot \frac{\partial}{\partial \mathbf{p}_i} &= \lim_{\Delta t \rightarrow 0} \frac{1}{\Delta t} \left[\int_t^{t+\Delta t} -\boldsymbol{\xi} R_i(t_1) \cdot \frac{\partial}{\partial \mathbf{p}_i} dt_1 \right. \\
&\quad \left. + \int_t^{t+\Delta t} \int_t^{t_1} (\boldsymbol{\xi} R_i(t_1) \cdot \frac{\partial}{\partial \mathbf{p}_i})(\boldsymbol{\xi} R_i(t_2) \cdot \frac{\partial}{\partial \mathbf{p}_i}) dt_1 dt_2 \right].
\end{aligned} \tag{5.10}$$

Since the time scale of $R_i(t)$ is much shorter than the phase variables, we can choose Δt long enough that we can replace the terms inside the integrals by their averages

$$\begin{aligned}
-\boldsymbol{\xi} R_i(t) \cdot \frac{\partial}{\partial \mathbf{p}_i} &= \lim_{\Delta t \rightarrow 0} \frac{1}{\Delta t} \left[\int_t^{t+\Delta t} -\langle \boldsymbol{\xi} R_i(t_1) \cdot \frac{\partial}{\partial \mathbf{p}_i} \rangle dt_1 \right. \\
&\quad \left. + \int_t^{t+\Delta t} \int_t^{t_1} \langle (\boldsymbol{\xi} R_i(t_1) \cdot \frac{\partial}{\partial \mathbf{p}_i})(\boldsymbol{\xi} R_i(t_2) \cdot \frac{\partial}{\partial \mathbf{p}_i}) \rangle dt_1 dt_2 \right].
\end{aligned} \tag{5.11}$$

According to Eq. (5.2) the first part of the right hand side of Eq. (5.11) is zero and

$$\begin{aligned}
-\boldsymbol{\xi} R_i(t) \cdot \frac{\partial}{\partial \mathbf{p}_i} &= \lim_{\Delta t \rightarrow 0} \frac{\xi^2}{\Delta t} \left[\int_t^{t+\Delta t} \int_t^{t_1} \langle R_i(t_1) R_i(t_2) \rangle \frac{\partial^2}{\partial p_i^2} dt_1 dt_2 \right] \\
&= \lim_{\Delta t \rightarrow 0} \frac{\xi^2}{2\Delta t} \left[\int_t^{t+\Delta t} \frac{\partial^2}{\partial p_i^2} dt_1 \right] \\
&= \frac{1}{2} \xi^2 \frac{\partial^2}{\partial p_i^2},
\end{aligned} \tag{5.12}$$

where we have used the property of the Dirac delta function $\int_t^{t_1} \delta(t_1 - t_2) dt_2 = 1/2$ where $t < t_2 < t_1$. From now on we assume $m = 1$ for simplicity. Replacing Eq. (5.12), in Eq. (5.7)

$$i\mathcal{L} = \dot{\Gamma} \cdot \frac{\partial}{\partial \Gamma} = \sum_i \left(\mathbf{v}_i \cdot \frac{\partial}{\partial \mathbf{r}_i} + \mathbf{F}_i \cdot \frac{\partial}{\partial \mathbf{v}_i} \right) + \sum_i \left(-\frac{1}{2} \xi^2 \frac{\partial^2}{\partial \mathbf{v}_i^2} - \gamma(\mathbf{v}_i) \mathbf{v}_i \cdot \frac{\partial}{\partial \mathbf{v}_i} \right). \quad (5.13)$$

Doing the same for Eq. (5.8) we have

$$-i\mathcal{L}^\dagger = -\dot{\Gamma} \cdot \frac{\partial}{\partial \Gamma} - \left(\frac{\partial}{\partial \Gamma} \cdot \dot{\Gamma} \right) = \sum_i \left(-\mathbf{v}_i \cdot \frac{\partial}{\partial \mathbf{r}_i} - \mathbf{F}_i \cdot \frac{\partial}{\partial \mathbf{v}_i} \right) + \sum_i \left(\frac{1}{2} \xi^2 \frac{\partial^2}{\partial \mathbf{v}_i^2} + \gamma(\mathbf{v}_i) \mathbf{v}_i \cdot \frac{\partial}{\partial \mathbf{v}_i} \right) + \sum_i \left(\frac{\partial \gamma(\mathbf{v}_i)}{\partial \mathbf{v}_i} \cdot \mathbf{v}_i + \gamma(\mathbf{v}_i) \right). \quad (5.14)$$

The average of a phase variable at time $t > 0$ can be calculated with having the distribution function at time $t > 0$, and the phase variable at time $t = 0$. The result will be the same if one use the distribution at the time $t > 0$, and the phase variable at time $t = 0$. The time evolution operator for a phase variable is the $i\mathcal{L}$ expressed in Eq. (5.13). The first two terms in this equation corresponds to the equilibrium situation, while the other terms originates from the existence of the velocity-dependent friction. The time evolution operator for the distribution is shown with $-i\mathcal{L}^\dagger$ as declared in Eq. (5.14).

5.3. Distribution Function

Using the time evolution operator $-i\mathcal{L}^\dagger$ in Eq. (5.14), we can write the time evolution equation (5.6) for the distribution of one particle

$$\frac{\partial f}{\partial t} + \mathbf{v}_i \cdot \frac{\partial f}{\partial \mathbf{r}_i} + \mathbf{F}_i \cdot \frac{\partial f}{\partial \mathbf{v}_i} = \frac{\partial}{\partial \mathbf{v}_i} \left[\gamma(\mathbf{v}_i) \mathbf{v}_i f + \frac{1}{2} \xi^2 \frac{\partial f}{\partial \mathbf{v}_i} \right]. \quad (5.15)$$

This is a Fokker-Planck equation. So, starting from the Langevin equation with velocity dependent friction and using the Liouville or time evolution operators we end up with the Fokker-Planck equation of the distribution function. In case of constant friction $\gamma(\mathbf{v}_i) = \gamma_0 = -\alpha$, the stationary solution of the Fokker-Planck

equation is

$$f_0(\mathbf{\Gamma}) = C \exp\left(-\frac{U(\{\mathbf{r}_i\})}{k_B T}\right) \exp\left(-\frac{\gamma_0 \sum_i \mathbf{v}_i^2}{\xi^2}\right) \quad (5.16)$$

where $\xi^2 = 2k_B T \gamma_0$ according to the fluctuation-dissipation theorem [50].

When friction is velocity dependent, the stationary solution of Eq. (5.15) is only trivial when neglecting the interaction forces, $F_i = 0$. The stationary solution ($\frac{\partial f_s}{\partial t} = 0$) of Eq. (5.15) in the case of $F_i = 0$ for one particle is [55]

$$f_s(\mathbf{v}) = C \exp\left(-\frac{2}{\xi^2} \int^{\mathbf{v}} d\mathbf{v}' \gamma(\mathbf{v}') \mathbf{v}'\right). \quad (5.17)$$

In this case the fluctuation-dissipation relation does not hold which is consistent with the non-equilibrium situation.

5.3.1. Rayleigh-Type Model of Friction

We consider a Rayleigh-type model of friction

$$\gamma(\mathbf{v}) = -\alpha + \beta \mathbf{v}^2. \quad (5.18)$$

This model of velocity dependent friction (pumping of energy) was introduced by Rayleigh in the theory of sound [113]. The Rayleigh friction has been used before to model the nonequilibrium Brownian motion [55, 114]. We choose the Rayleigh friction because of its ability of modeling the pumping of energy to the system, through the slow particles, without any rotational or directional dependence. For simplicity of analytically calculating the distributions we consider $\beta = 1$, so that

$$\gamma(\mathbf{v}) = -\alpha + \mathbf{v}^2. \quad (5.19)$$

When the direction of the so-called dissipative force $-\gamma(\mathbf{v})\mathbf{v}$, is the same as the velocity, or in other words, when $\gamma(\mathbf{v})$ is negative the particle experiences additional mechanical energy pumped into the system. In the other hand, when $\gamma(\mathbf{v})$ is positive, the dissipative force results in dissipation of mechanical energy of the particle. We have shown in Fig. 5.1 the regions in the $\alpha, v = |\mathbf{v}|$ plane which leads to Brownian particles being active (pump of energy to the system) or passive (energy dissipation).

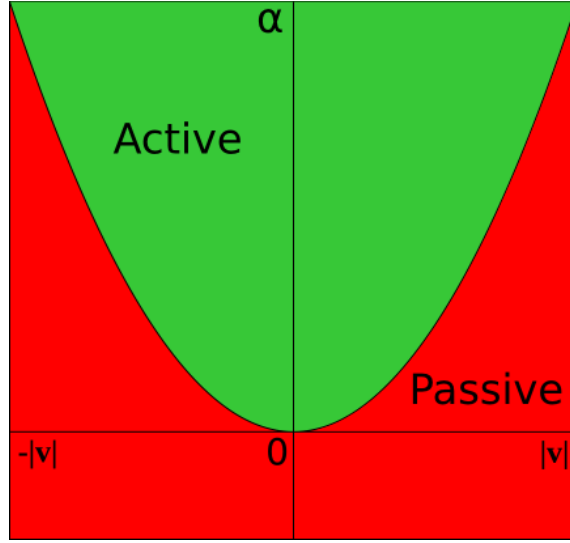


Figure 5.1.: Different regions in the α and $v = |\mathbf{v}|$ plane which leads to Brownian particles being active (pump of energy to the system) or passive (energy dissipation). What separates these two regions from each other is the curve $\mathbf{v}^2 = \alpha$ or $\gamma(\mathbf{v}) = -\alpha + \mathbf{v}^2 = 0$.

5.3.2. Distribution Function and Effective Temperature in Case of Rayleigh-Type Model of Friction

The stationary velocity distribution (Eq. (5.17)) using the Rayleigh model of friction in Eq. (5.19) in terms of $D_v = \xi^2/2$ can be written as

$$f_{SR}(\mathbf{v}) = C \exp\left(-\frac{2}{\xi^2}\left(\frac{\mathbf{v}^4}{4} - \alpha\frac{\mathbf{v}^2}{2}\right)\right). \quad (5.20)$$

In two-dimensions when $d\mathbf{v} = 2\pi v dv$, one can analytically obtain the value of C in terms of $D_v = \xi^2/2$, as it is also obtained in [114]

$$\begin{aligned} \frac{1}{C} &= 2\pi \int_0^\infty \exp\left(-\frac{2}{\xi^2}\left(\frac{\mathbf{v}^4}{4} - \alpha\frac{\mathbf{v}^2}{2}\right)\right) v dv \\ &= \pi\sqrt{\pi D_v} \exp\left(\frac{\alpha^2}{4D_v}\right) \left[1 + \operatorname{erf}\left(\frac{\alpha}{2\sqrt{D_v}}\right)\right]. \end{aligned} \quad (5.21)$$

In principle it should be possible to calculate this and the following integrals in 3D. But for matter of simplicity we stay with a two dimensional system. Fig. 5.3 shows the 2D normalized distribution $f_{SR}(\mathbf{v})$ for $\alpha = 1$ and different values of $\xi^2/2$. As it is visible from the figure 5.1, When $\alpha = 1$ the particles with the speed $v < 1$ are accelerated (show activity), while the particles who are faster are damped (show

passive behavior). The probability of finding particles with the velocity $|\mathbf{v}| < 1$ is proportional to the area under the velocity distribution curves in Fig. 5.3 in that interval. One can observe that with increasing the noise strength the probability of finding slower particles decreases, which indicates that for a constant α value, the active behavior of the system with increasing the noise strength, decreases.

The second, fourth and sixth moment of velocity in two-dimensions can be written as:

$$\begin{aligned}\langle \mathbf{v}^2 \rangle &= 2\pi \int_0^\infty f_{SR}(\mathbf{v}) v^2 v dv \\ &= \alpha + 2\sqrt{\frac{D_v}{\pi}} \exp\left(-\frac{\alpha^2}{4D_v}\right) \left[1 + \operatorname{erf}\left(\frac{\alpha}{2\sqrt{D_v}}\right)\right]^{-1}\end{aligned}\quad (5.22)$$

$$\langle \mathbf{v}^4 \rangle = 2D_v + \alpha \langle \mathbf{v}^2 \rangle = \xi^2 + \alpha \langle \mathbf{v}^2 \rangle \quad (5.23)$$

$$\langle \mathbf{v}^6 \rangle = 2\alpha D_v + (\alpha^2 + 4D_v) \langle \mathbf{v}^2 \rangle = \alpha \xi^2 + (\alpha^2 + 2\xi^2) \langle \mathbf{v}^2 \rangle \quad (5.24)$$

These equations have been derived in Appendix C where we have also explained the slight difference between $\langle \mathbf{v}^2 \rangle$, $\langle \mathbf{v}^4 \rangle$ and what has been shown in [114]. Since the velocity distribution is an even function, the odd moments of velocity are zero in any dimension. The velocity distribution function only contains \mathbf{v}^2 term, thus $\langle v_x^2 \rangle = \langle v_y^2 \rangle$ and in two dimensions: $\langle v_x^2 \rangle = \langle v_y^2 \rangle = \langle \mathbf{v}^2 \rangle / 2$. We define the effective temperature of the system as

$$k_B T_{\text{Eff}} = \langle v_x^2 \rangle = \langle v_y^2 \rangle = \frac{\langle \mathbf{v}^2 \rangle}{2}. \quad (5.25)$$

Fig. 5.4 demonstrates the relation between $\langle \mathbf{v}^2 \rangle$ and $\xi^2/2$ due to Eq. (5.22). In case of the normal Langevin equation with constant friction γ_0 , the fluctuation-dissipation relation holds and $\xi^2/2\gamma_0 = k_B T = \langle \mathbf{v}^2 \rangle / 2$, so that there is a linear relation between $\langle \mathbf{v}^2 \rangle$ and $\xi^2/2$. But as we can see in the Fig. 5.4, $\langle \mathbf{v}^2 \rangle$ and $\xi^2/2$ have a non-linear relation. This nonlinearity originates from the velocity dependent friction.

We assume that we can model the distribution of the particles with separating

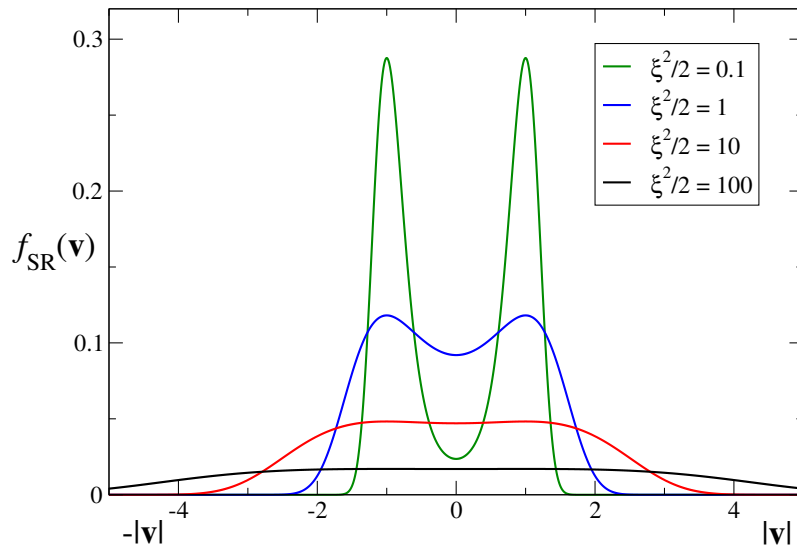


Figure 5.2.: The stationary velocity distribution for non-interacting Brownian particles shown in Eq. (5.20) for $\alpha = 1$ and different values of $D_v = \xi^2/2$.

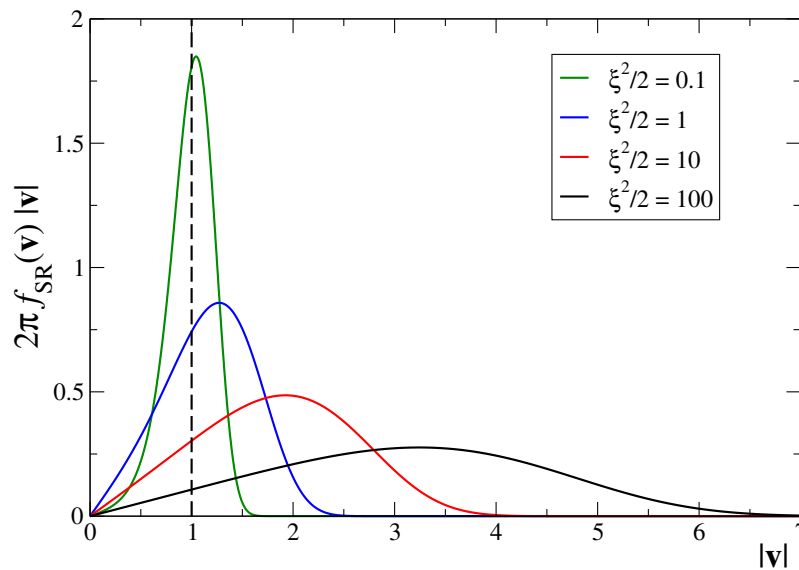


Figure 5.3.: The stationary velocity distribution for non-interacting Brownian particles (shown in Eq. (5.20)) multiplied by their speed, for $\alpha = 1$ and different values of $D_v = \xi^2/2$. When $\alpha = 1$ the particles with the speed $0 < |\mathbf{v}| < 1$ are accelerated (show activity). The probability of finding particles with the velocity $0 < |\mathbf{v}| < 1$ is equal to the area under the curves in that interval. With increasing the noise strength the probability of finding the particles which show activity decreases. This indicates that for a constant α value, the active behavior of the system with increasing the noise strength, decreases.

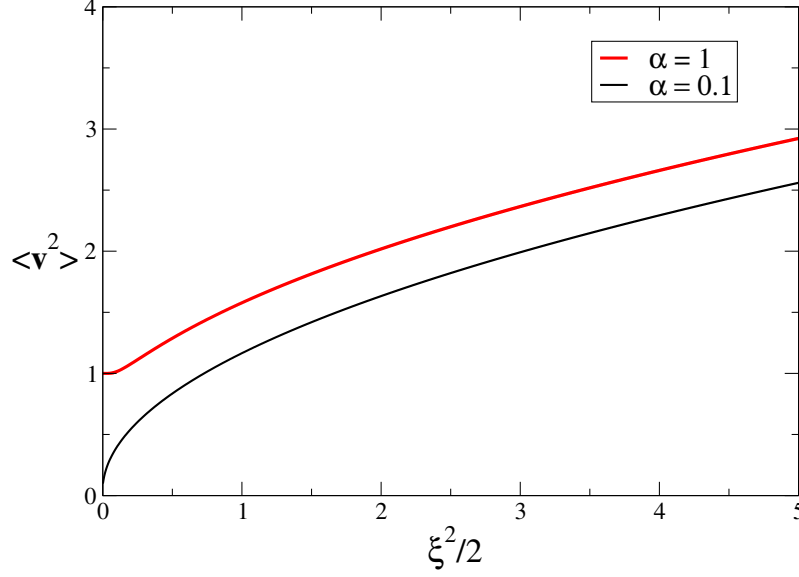


Figure 5.4.: Second moment of velocity proportional to the effective temperature against $D_v = \xi^2/2$ for different values of α . There exists a nonlinear relation between $\langle \mathbf{v}^2 \rangle$ and $\xi^2/2$ which originates from velocity dependent friction.

the position and velocity dependence part

$$f(\{\mathbf{r}_i\}, \{\mathbf{v}_i\}) = C \exp\left(-2\frac{U(\{\mathbf{r}_i\})}{\langle \mathbf{v}^2 \rangle}\right) \exp\left(-\frac{2}{\xi^2} \sum_i \int^{\mathbf{v}} d\mathbf{v}'_i \gamma(\mathbf{v}') \mathbf{v}'\right). \quad (5.26)$$

For the Rayleigh model of friction this will lead to

$$f(\{\mathbf{r}_i\}, \{\mathbf{v}_i\}) = C \exp\left(-2\frac{U(\{\mathbf{r}_i\})}{\langle \mathbf{v}^2 \rangle}\right) \exp\left(-\frac{2}{\xi^2} \sum_i \left(\frac{\mathbf{v}_i^4}{4} - \alpha \frac{\mathbf{v}_i^2}{2}\right)\right). \quad (5.27)$$

Replacing Eq. (5.26) in the Fokker Planck equation, Eq. (5.15), will result in

$$\begin{aligned} \frac{\partial f}{\partial t} &= \sum_i \left(-\frac{2}{\langle \mathbf{v}^2 \rangle} \mathbf{v}_i \cdot \mathbf{F}_i + \frac{2}{\xi^2} \mathbf{F}_i \cdot \mathbf{v}_i \gamma(\mathbf{v}_i) \right) f \\ &= \sum_i \left(-\frac{2}{\langle \mathbf{v}^2 \rangle} \mathbf{F}_i \cdot \mathbf{v}_i - \frac{2\alpha}{\xi^2} \mathbf{F}_i \cdot \mathbf{v}_i + \frac{2}{\xi^2} \mathbf{v}_i^2 \mathbf{F}_i \cdot \mathbf{v}_i \right) f. \end{aligned} \quad (5.28)$$

For understanding a little more about the term $\mathbf{F}_i \cdot \mathbf{v}_i$ we can multiply the nonlinear Langevin equation by \mathbf{v}_i

$$\mathbf{v}_i \cdot \frac{d\mathbf{v}_i}{dt} - \mathbf{F}_i \cdot \mathbf{v}_i = -\gamma(\mathbf{v}_i) \mathbf{v}_i^2 + \boldsymbol{\xi} R_i(t) \cdot \mathbf{v}_i \quad (5.29)$$

which can be representative of the mechanical energy loss or gain of one particle in

the system. For having the same equation in a more general form we use Eq. (5.5) and (5.13) to evaluate the time evolution of the variable $\sum_i \frac{\mathbf{v}_i^2}{2}$

$$\begin{aligned} \frac{d}{dt} \sum_i \frac{\mathbf{v}_i^2}{2} &= \sum_i \mathbf{v}_i \cdot \frac{d\mathbf{v}_i}{dt} \\ &= i\mathcal{L} \sum_i \frac{\mathbf{v}_i^2}{2} \\ &= \sum_i \mathbf{F}_i \cdot \mathbf{v}_i - \sum_i \gamma(\mathbf{v}_i) \mathbf{v}_i^2 + \sum_i \frac{\xi^2}{2} \end{aligned} \quad (5.30)$$

In an overdamped motion where $d\mathbf{v}_i/dt = 0$ we have

$$\begin{aligned} \sum_i \mathbf{F}_i \cdot \mathbf{v}_i &= \sum_i \gamma(\mathbf{v}_i) \mathbf{v}_i^2 - \sum_i \frac{\xi^2}{2} \\ &= - \sum_i \alpha \mathbf{v}_i^2 + \sum_i \mathbf{v}_i^4 - \sum_i \frac{\xi^2}{2}. \end{aligned} \quad (5.31)$$

Replacing this in Eq. (5.28) would lead to

$$\frac{\partial f}{\partial t} = \Lambda f, \quad (5.32)$$

where

$$\begin{aligned} \Lambda &= \left(\alpha N + \frac{N\xi^2}{\langle \mathbf{v}^2 \rangle} \right) + \left(\frac{2\alpha^2}{\xi^2} + \frac{2\alpha}{\langle \mathbf{v}^2 \rangle} - 1 \right) \sum_i \mathbf{v}_i^2 \\ &\quad + \left(-\frac{4\alpha}{\xi^2} - \frac{2}{\langle \mathbf{v}^2 \rangle} \right) \sum_i \mathbf{v}_i^4 + \frac{2}{\xi^2} \sum_i \mathbf{v}_i^6. \end{aligned} \quad (5.33)$$

5.3.3. Probability of Finding Particles with Negative Friction (Active Particles)

Following Eq. (5.19), particles who have the velocity value $v < \sqrt{\alpha}$, have negative friction. Negative friction means that these particles are accelerated or show activity. For every distribution function with specific value of α and D_v , which follows Eq. (5.20), the probability of finding particles which have the velocity less than $\sqrt{\alpha}$ is equal to

$$P_{\text{active}} = \int_0^{\sqrt{\alpha}} 2\pi f_{SR}(\mathbf{v}) v dv \quad (5.34)$$

The integral can be solved as

$$P_{\text{active}} = 2\pi C \int_0^{\sqrt{\alpha}} \exp\left(-\frac{1}{D_v}\left(\frac{\mathbf{v}^4}{4} - \alpha\frac{\mathbf{v}^2}{2}\right)\right) v \, dv = \frac{\text{erf}\left(\frac{\alpha}{2\sqrt{D_v}}\right)}{1 + \text{erf}\left(\frac{\alpha}{2\sqrt{D_v}}\right)}. \quad (5.35)$$

Therefore, to compare two systems which have different values of α and D_v , we can use Eq. (5.35). The larger the P_{active} , the larger the percentage of particles in the system with negative friction. As it is represented in Figure 5.5, for a constant temperature $\langle \mathbf{v} \rangle = 2k_{\text{B}}T_{\text{Eff}} = 3$, we choose three pairs of (α, D_v) . Using Eq. (5.35), we can obtain the probability of finding active particles in the systems which are determined by these three pairs. The P_{active} is equal to 0.021, 0.288 and 0.357 for $(\alpha = 0.1, D_v = 6.897)$, $(\alpha = 1, D_v = 5.315)$ and $(\alpha = 2, D_v = 3.415)$, respectively. The probability of finding active particles is equal to the area under the corresponding $2\pi f_{SR}(\mathbf{v})v$ curve between zero and $v = \sqrt{\alpha}$, see Figure 5.6. For a constant effective temperature, the larger the α is (or the smaller the D_v is), the probability of finding active particles is higher.

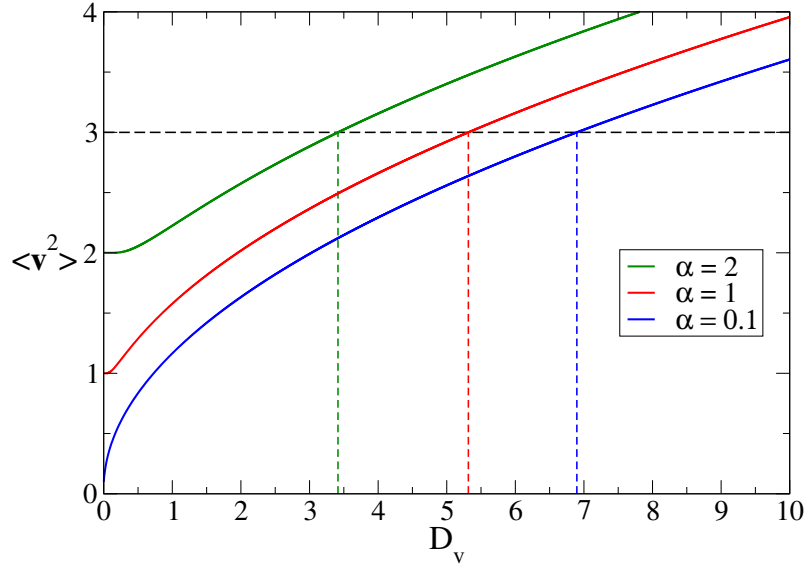


Figure 5.5.: Second moment of velocity proportional to the effective temperature against D_v for three different values of α according to Eq. (5.22). We choose three pairs of (α, D_v) with a constant temperature $\langle \mathbf{v} \rangle = 2k_{\text{B}}T_{\text{Eff}} = 3$.

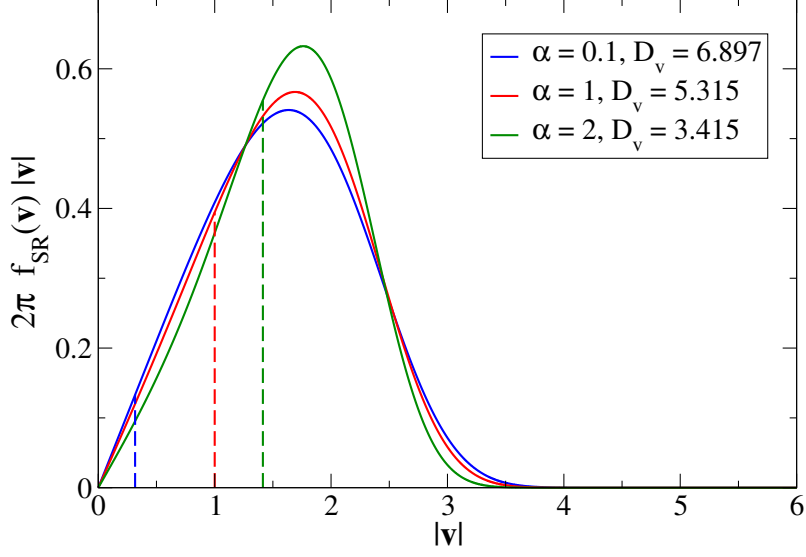


Figure 5.6.: The stationary velocity distribution for non-interacting Brownian particles (shown in Eq. (5.20)) multiplied by $2\pi v$, for different pairs of α and D_v . The (α, D_v) pairs are chosen as we have shown in Fig. (5.5). The particles with the speed $v < \sqrt{\alpha}$ are accelerated (show activity). The $\sqrt{\alpha}$ is shown in dashed for every curve. The probability of finding particles with the velocity between zero and $\sqrt{\alpha}$ is equal to the area under the curves in that interval. This area is 0.021, 0.288 and 0.357 for blue curve ($\alpha = 0.1, D_v = 6.897$), red curve ($\alpha = 1, D_v = 5.315$) and the green curve ($\alpha = 2, D_v = 3.415$), respectively. When temperature is constant, with increasing the α , the probability of finding the particles which show activity, increases. This indicates that the active behavior of the system with increasing α , increases.

5.4. Definition of the Averages

It will be useful for later sections to have a consistent definition of the ensemble averages of the product of the phase variables A and $i\mathcal{L}B$:

$$\langle A^* | i\mathcal{L}B \rangle = \int f A^* i\mathcal{L}B \, d\Gamma, \quad (5.36)$$

and

$$\langle -i\mathcal{L}^\dagger A^* | B \rangle = - \int (i\mathcal{L}^\dagger f A^*) B \, d\Gamma. \quad (5.37)$$

The effect of $i\mathcal{L}^\dagger$ on fA^* can be evaluated as [59]

$$\begin{aligned} i\mathcal{L}^\dagger f A^* &= \dot{\Gamma} \cdot \frac{\partial}{\partial \Gamma} (f A^*) + \left(\frac{\partial}{\partial \Gamma} \cdot \dot{\Gamma} \right) f A^* \\ &= f \dot{\Gamma} \cdot \frac{\partial A^*}{\partial \Gamma} + A^* \dot{\Gamma} \cdot \frac{\partial f}{\partial \Gamma} + A^* \left(\frac{\partial}{\partial \Gamma} \cdot \dot{\Gamma} \right) f \\ &= f i\mathcal{L}A^* + A^* i\mathcal{L}^\dagger f. \end{aligned} \quad (5.38)$$

When the distribution follows Eq. (5.16), the $i\mathcal{L}^\dagger f$ is zero according to the equations (5.14) and (5.15). So one can write

$$i\mathcal{L}^\dagger f_0 A^* = f_0 i\mathcal{L} A^* \quad (5.39)$$

and

$$\begin{aligned} \langle -i\mathcal{L}^\dagger A^* | B \rangle_0 &= - \int B i\mathcal{L}^\dagger f_0 A^* d\Gamma \\ &= - \int f_0 B i\mathcal{L} A^* d\Gamma, \end{aligned} \quad (5.40)$$

which leads to

$$\langle \exp(-i\mathcal{L}^\dagger t) A^* | B \rangle_0 = \int f_0 B \exp(-i\mathcal{L} t) A^* d\Gamma. \quad (5.41)$$

From Eq. (5.41) and also knowing that $\langle A^* | \exp(i\mathcal{L} t) B \rangle = \langle A^* | B(t) \rangle$ one can write

$$\langle \exp(-i\mathcal{L}^\dagger t) A^* | B \rangle_0 = \langle A^*(-t) | B \rangle_0. \quad (5.42)$$

If we assume $\langle A^* | B(t) \rangle = \langle A^*(-t) | B \rangle$ then

$$\langle A^* | \exp(i\mathcal{L} t) B \rangle_0 = \langle \exp(-i\mathcal{L}^\dagger t) A^* | B \rangle_0. \quad (5.43)$$

We should have in mind that as long as the distribution function is a stationary solution of the Fokker-Planck equation, the relations listed in Eq. (5.39) to (5.43) are valid.

In the following parts of this chapter we use the distribution function noted in Eq. (5.27). Since that is not the stationary solution of the Fokker-Planck equation, $i\mathcal{L}^\dagger f$ will not be zero. In that case

$$\begin{aligned} i\mathcal{L}^\dagger f A^* &= f i\mathcal{L} A^* + A^* i\mathcal{L}^\dagger f \\ &= f i\mathcal{L} A^* + A^* \Lambda f, \end{aligned} \quad (5.44)$$

where Λ is noted in Eq. (5.33). Consequently

$$\langle -i\mathcal{L}^\dagger A^* | B \rangle = - \int f B i\mathcal{L} A^* d\Gamma - \int A^* B \Lambda f d\Gamma. \quad (5.45)$$

5.5. Mori-Zwanzig Formalism

We consider two dynamical phase variables

$$\rho_{\mathbf{q}}(t) = \sum_k \exp(i\mathbf{q} \cdot \mathbf{r}_k(t)) \quad (5.46)$$

$$j_{\mathbf{q}}^L(t) = \sum_k v_k^L \exp(i\mathbf{q} \cdot \mathbf{r}_k(t)), \quad (5.47)$$

where $\mathbf{q} = (0, 0, q)$ and L is the longitudinal direction parallel to \mathbf{q} . The inner product of $\rho_{\mathbf{q}}(t=0)$ with itself in 2D is

$$\begin{aligned} \langle \rho_{\mathbf{q}}^* | \rho_{\mathbf{q}} \rangle &= \left\langle \sum_{i,j} \exp(i\mathbf{q} \cdot (\mathbf{r}_i - \mathbf{r}_j)) \right\rangle \\ &= \left\langle \sum_{i,j} \int \delta(\mathbf{r} - \mathbf{r}_i + \mathbf{r}_j) \exp(i\mathbf{q} \cdot \mathbf{r}) d^2\mathbf{r} \right\rangle \\ &= N \left(1 + \frac{1}{N} \int \sum_{i \neq j} \langle \delta(\mathbf{r} - \mathbf{r}_i + \mathbf{r}_j) \rangle \exp(i\mathbf{q} \cdot \mathbf{r}) d^2\mathbf{r} \right) = NS_q. \end{aligned} \quad (5.48)$$

For $j_{\mathbf{q}}^L(t=0)$ knowing that the odd moments of velocity are zero

$$\langle j_{\mathbf{q}}^{L*} | j_{\mathbf{q}}^L \rangle = N \langle v_i^{L2} \rangle = \frac{N}{2} \langle \mathbf{v}^2 \rangle, \quad (5.49)$$

where $\langle \mathbf{v}^2 \rangle$ follows Eq. (5.22). Here we have used the fact that the velocity distribution, Eq. (5.20), depends on the velocity merely through $|\mathbf{v}|$. So the average of the longitudinal component of the velocity is equal to the average of the transverse component and in two dimensions

$$\langle v^{L2} \rangle = \langle v^{T2} \rangle = \frac{1}{2} \langle \mathbf{v}^2 \rangle. \quad (5.50)$$

using Eq. (5.48) and (5.49) for normalization we define

$$\mathbf{A} = \begin{pmatrix} \frac{1}{\sqrt{NS_q}} \rho_{\mathbf{q}} \\ \sqrt{\frac{2}{N \langle \mathbf{v}^2 \rangle}} j_{\mathbf{q}}^L \end{pmatrix}. \quad (5.51)$$

In the following we use Mori-Zwanzig formalism [61], to project the phase variables in to two subspace of slow (relevant) and fast (irrelevant) variables. This is done

with the use of the projection operators

$$\begin{aligned}\mathcal{P} &= A_1 \langle A_1^* | \dots \rangle + A_2 \langle A_2^* | \dots \rangle \\ &= \frac{1}{NS_q} \rho_{\mathbf{q}} \langle \rho_{\mathbf{q}}^* | \dots \rangle + \frac{2}{N \langle \mathbf{v}^2 \rangle} j_{\mathbf{q}}^L \langle j_{\mathbf{q}}^{L*} | \dots \rangle.\end{aligned}\quad (5.52)$$

and $\mathcal{Q} = 1 - \mathcal{P}$. Then the equation of motion or time evolution equation for the correlation function can be written as (see Appendix E for derivation)

$$(z\mathbf{I} + \mathbf{\Omega} - \mathbf{M}) \mathbf{Y}(z) = -\mathbf{I}.\quad (5.53)$$

In this equation

$$Y_{nm}(z) = \langle A_n^* | \tilde{A}_m(z) \rangle\quad (5.54)$$

where $\tilde{A}_m(z) = i \int_0^\infty dt \exp(izt) A(t)$ is a Laplace transform of $A_m(t)$,

$$\Omega_{nm} = \langle A_n^* | \mathcal{L} A_m \rangle\quad (5.55)$$

and

$$M_{nm} = \langle A_n^* | \mathcal{L} \mathcal{Q} (z + \mathcal{Q} \mathcal{L} \mathcal{Q})^{-1} \mathcal{Q} \mathcal{L} A_m \rangle.\quad (5.56)$$

Now we calculate the Ω_{nm} :

$$\Omega_{11} = \frac{1}{NS_q} \langle \rho_{\mathbf{q}}^* | \mathcal{L} \rho_{\mathbf{q}} \rangle = \frac{1}{iNS_q} \langle \rho_{\mathbf{q}}^* | i \mathcal{L} \rho_{\mathbf{q}} \rangle = 0.\quad (5.57)$$

With use of Eq. (5.13), since $\langle v^L \rangle = 0$, $\Omega_{11} = 0$. From Eq. (5.36) and (5.13) we have

$$\begin{aligned}\Omega_{21} &= \frac{1}{iN \sqrt{S_q \langle \mathbf{v}^2 \rangle} / 2} \langle j_{\mathbf{q}}^{L*} | i \mathcal{L} \rho_{\mathbf{q}} \rangle \\ &= \frac{\sqrt{2}}{iN \sqrt{S_q \langle \mathbf{v}^2 \rangle}} \int d\Gamma f \sum_k v_k^L \exp(-i\mathbf{q} \cdot \mathbf{r}_k) \sum_i \mathbf{v}_i \cdot \frac{\partial}{\partial \mathbf{r}_i} \left(\sum_{k'} \exp(i\mathbf{q} \cdot \mathbf{r}_{k'}) \right) \\ &= \frac{Nq \langle \mathbf{v}^2 \rangle}{2N \sqrt{S_q \langle \mathbf{v}^2 \rangle} / 2} = q \sqrt{\frac{\langle \mathbf{v}^2 \rangle}{2S_q}}.\end{aligned}\quad (5.58)$$

Using Eq. (5.13) we obtain

$$\begin{aligned}
\Omega_{12} &= \frac{1}{iN\sqrt{S_q\langle\mathbf{v}^2\rangle/2}} \langle \rho_{\mathbf{q}}^* | i\mathcal{L} j_{\mathbf{q}}^L \rangle \\
&= \frac{1}{iN\sqrt{S_q\langle\mathbf{v}^2\rangle/2}} \int d\Gamma f \sum_k \exp(-i\mathbf{q}\cdot\mathbf{r}_k) \left(\sum_i \mathbf{v}_i \cdot \frac{\partial}{\partial \mathbf{r}_i} + \sum_i \mathbf{F}_i \cdot \frac{\partial}{\partial \mathbf{v}_i} \right. \\
&\quad \left. - \sum_i (-\alpha + \mathbf{v}_i^2) \mathbf{v}_i \cdot \frac{\partial}{\partial \mathbf{v}_i} \right) \sum_{k'} v_{k'}^L \exp(i\mathbf{q}\cdot\mathbf{r}_{k'}) \\
&= \Omega_{12}^1 + \Omega_{12}^2 + \Omega_{12}^3.
\end{aligned} \tag{5.59}$$

The operation of the third term inside the parentheses on the rest of the integral leads to the odd moments of velocity which is zero, so $\Omega_{12}^3 = 0$. Now we derive Ω_{12}^1 and Ω_{12}^2 separately:

$$\begin{aligned}
\Omega_{12}^1 &= \frac{1}{iN\sqrt{S_q\langle\mathbf{v}^2\rangle/2}} \int d\Gamma f \sum_k \exp(-i\mathbf{q}\cdot\mathbf{r}_k) \left(\sum_i \mathbf{v}_i \cdot \frac{\partial}{\partial \mathbf{r}_i} \right) \sum_{k'} v_{k'}^L \exp(i\mathbf{q}\cdot\mathbf{r}_{k'}) \\
&= \frac{iq}{iN\sqrt{S_q\langle\mathbf{v}^2\rangle/2}} \int d\Gamma f \sum_k \exp(-i\mathbf{q}\cdot\mathbf{r}_k) \sum_i v_i^{L2} \exp(i\mathbf{q}\cdot\mathbf{r}_i) \\
&= \frac{iq}{iN\sqrt{S_q\langle\mathbf{v}^2\rangle/2}} \int d\Gamma f \sum_{i,k} v_i^{L2} \exp(i\mathbf{q}\cdot(\mathbf{r}_i - \mathbf{r}_k)) \\
&= q\sqrt{\frac{\langle\mathbf{v}^2\rangle S_q}{2}},
\end{aligned} \tag{5.60}$$

and

$$\begin{aligned}
\Omega_{12}^2 &= \frac{1}{iN\sqrt{S_q\langle\mathbf{v}^2\rangle/2}} \int d\Gamma f \sum_k \exp(-i\mathbf{q}\cdot\mathbf{r}_k) \left(\sum_i \mathbf{F}_i \cdot \frac{\partial}{\partial \mathbf{v}_i} \right) \sum_{k'} v_{k'}^L \exp(i\mathbf{q}\cdot\mathbf{r}_{k'}) \\
&= \frac{1}{iN\sqrt{S_q\langle\mathbf{v}^2\rangle/2}} \int d\Gamma f \sum_k \exp(-i\mathbf{q}\cdot\mathbf{r}_k) \sum_i F_i^L \exp(i\mathbf{q}\cdot\mathbf{r}_i).
\end{aligned} \tag{5.61}$$

We use the method applied in [115] for a related case, to obtain the average in Eq. (5.61). According to Eq. (5.27)

$$\frac{\partial f}{\partial \mathbf{r}_i} = -\frac{2}{\langle\mathbf{v}^2\rangle} \frac{\partial U}{\partial \mathbf{r}_i} f = \frac{2}{\langle\mathbf{v}^2\rangle} \mathbf{F}_i f, \tag{5.62}$$

and also by means of partial integration

$$\int B \frac{\partial f}{\partial \mathbf{r}_i} d\Gamma = - \int f \frac{\partial B}{\partial \mathbf{r}_i} d\Gamma. \quad (5.63)$$

Therefore

$$\begin{aligned} \Omega_{12}^2 &= \frac{\langle \mathbf{v}^2 \rangle}{iN2\sqrt{S_q\langle \mathbf{v}^2 \rangle}/2} \sum_i \int d\Gamma \frac{\partial f}{\partial r_i^L} \exp(i\mathbf{q} \cdot \mathbf{r}_i) \sum_k \exp(-i\mathbf{q} \cdot \mathbf{r}_k) \\ &= -\frac{1}{iN} \sqrt{\frac{\langle \mathbf{v}^2 \rangle}{2S_q}} \sum_i \int d\Gamma f \frac{\partial}{\partial r_i^L} \left(\exp(i\mathbf{q} \cdot \mathbf{r}_i) \sum_k \exp(-i\mathbf{q} \cdot \mathbf{r}_k) \right) \\ &= -\frac{1}{iN} \sqrt{\frac{\langle \mathbf{v}^2 \rangle}{2S_q}} \sum_i \int d\Gamma f i\mathbf{q} \left(\exp(i\mathbf{q} \cdot \mathbf{r}_i) \sum_k \exp(-i\mathbf{q} \cdot \mathbf{r}_k) - 1 \right) \\ &= -q \sqrt{\frac{\langle \mathbf{v}^2 \rangle}{2S_q}} (S_q - 1). \end{aligned} \quad (5.64)$$

So we would conclude from $\Omega_{12} = \Omega_{12}^1 + \Omega_{12}^2$ that

$$\Omega_{12} = \Omega_{21} = q \sqrt{\frac{\langle \mathbf{v}^2 \rangle}{2S_q}}. \quad (5.65)$$

This is the same as in equilibrium.

Now we calculate the Ω_{22}

$$\begin{aligned} \Omega_{22} &= \frac{2}{iN\langle \mathbf{v}^2 \rangle} \langle j_{\mathbf{q}}^{L*} | i\mathcal{L} j_{\mathbf{q}}^L \rangle \\ &= \frac{2}{iN\langle \mathbf{v}^2 \rangle} \int d\Gamma f \sum_k v_k^L \exp(-i\mathbf{q} \cdot \mathbf{r}_k) \left(- \sum_i (-\alpha + \mathbf{v}_i^2) \mathbf{v}_i \cdot \frac{\partial}{\partial \mathbf{v}_i} \right. \\ &\quad \left. + \sum_i \mathbf{F}_i \cdot \frac{\partial}{\partial \mathbf{v}_i} \right) \sum_{k'} v_{k'}^L \exp(i\mathbf{q} \cdot \mathbf{r}_{k'}) \\ &= \frac{1}{i\langle \mathbf{v}^2 \rangle} (\alpha \langle \mathbf{v}^2 \rangle - \langle \mathbf{v}^4 \rangle) + \frac{2}{iN\langle \mathbf{v}^2 \rangle} \int d\Gamma f \sum_k v_k^L F_k^L. \end{aligned} \quad (5.66)$$

We can recall from Eq. (5.23) that $\alpha \langle \mathbf{v}^2 \rangle - \langle \mathbf{v}^4 \rangle = -2D_v = -\xi^2$. Knowing that $\sum_k v_k^L F_k^L = \frac{1}{2} \sum_k \mathbf{v}_k \cdot \mathbf{F}_k$, from Eq. (5.31) we will have

$$\int d\Gamma f \sum_k v_k^L F_k^L = \frac{N}{2} \left(-\alpha \langle \mathbf{v}^2 \rangle + \langle \mathbf{v}^4 \rangle - \frac{\xi^2}{2} \right). \quad (5.67)$$

Therefore

$$\Omega_{22} = \frac{iD_v}{\langle \mathbf{v}^2 \rangle} = \frac{i\xi^2}{2\langle \mathbf{v}^2 \rangle}. \quad (5.68)$$

So the existence of a the velocity dependent friction term in the Langevin equation leads to the $\langle j_{\mathbf{q}}^{L*} | i\mathcal{L}j_{\mathbf{q}}^L \rangle = iND_v/2$, Where the D_v is related to the second and forth moment of velocity through Eq. (5.22). But $\langle \rho_{\mathbf{q}}^* | i\mathcal{L}\rho_{\mathbf{q}} \rangle$ is still zero since the odd moments of velocity are zero. We can write the elements of the Ω matrix as

$$\Omega = \begin{pmatrix} 0 & q\sqrt{\frac{\langle \mathbf{v}^2 \rangle}{2S_q}} \\ q\sqrt{\frac{\langle \mathbf{v}^2 \rangle}{2S_q}} & \frac{i\xi^2}{2\langle \mathbf{v}^2 \rangle} \end{pmatrix}. \quad (5.69)$$

In Appendix D we show that in case of normal Brownian motion (equilibrium case) the $\sum_i \mathbf{F}_i \cdot \mathbf{v}_i = 0$ and $\Omega_{22} = i\gamma_0$.

5.6. Mode-Coupling Approximation

For writing the complete equation of motion, Eq. (5.53), we still need to know the elements of the memory kernel M_{nm} . We recall that From Eq. (5.58), $\mathcal{L}A_1 = q\sqrt{\frac{\langle \mathbf{v}^2 \rangle}{2S_q}}A_2$ so $\mathcal{Q}\mathcal{L}A_1 = 0$ and $M_{11} = M_{21} = 0$. M_{22} can be written as

$$\begin{aligned} M_{22} &= \langle A_2^* | \mathcal{L}\mathcal{Q}(z + \mathcal{Q}\mathcal{L}\mathcal{Q})^{-1} \mathcal{Q}\mathcal{L}A_2 \rangle \\ &= \langle A_2^* | \mathcal{L}\mathcal{Q} \exp(it\mathcal{Q}\mathcal{L}\mathcal{Q}) \mathcal{Q}\mathcal{L}A_2 \rangle. \end{aligned} \quad (5.70)$$

For separating the remaining fast decaying fluctuation from the memory kernel we use the projection operator $\mathcal{P}_M = \mathcal{P}_M^1 + \mathcal{P}_M^2 + \mathcal{P}_M^3$ to project on to the pair modes of density and currents:

$$\begin{aligned} \mathcal{P}_M &= \sum_{\mathbf{k} < \mathbf{p}} \rho_{\mathbf{k}} \rho_{\mathbf{p}} \frac{\langle \rho_{\mathbf{k}}^* \rho_{\mathbf{p}}^* | \dots \rangle}{\langle \rho_{\mathbf{k}}^* \rho_{\mathbf{p}}^* | \rho_{\mathbf{k}} \rho_{\mathbf{p}} \rangle} + \sum_{\mathbf{k} < \mathbf{p}} j_{\mathbf{k}}^L \rho_{\mathbf{p}} \frac{\langle j_{\mathbf{k}}^{L*} \rho_{\mathbf{p}}^* | \dots \rangle}{\langle j_{\mathbf{k}}^{L*} \rho_{\mathbf{p}}^* | j_{\mathbf{k}}^L \rho_{\mathbf{p}} \rangle} \\ &\quad + \sum_{\mathbf{k} < \mathbf{p}} j_{\mathbf{k}}^L j_{\mathbf{p}}^L \frac{\langle j_{\mathbf{k}}^{L*} j_{\mathbf{p}}^{L*} | \dots \rangle}{\langle j_{\mathbf{k}}^{L*} j_{\mathbf{p}}^{L*} | j_{\mathbf{k}}^L j_{\mathbf{p}}^L \rangle}. \end{aligned} \quad (5.71)$$

In a sense by projecting the kernel on to the pair modes of density and current, the slowly decaying parts of the memory kernel remain which have the longest relaxation times [66]. As mode coupling theory assumes the decay of the correlation functions

at the long time scales is dominated by those slowly decaying part of the memory kernel. We will show later in section 5.8 that, projection on $|j_{\mathbf{k}}^L \rho_{\mathbf{p}}\rangle$ and $|j_{\mathbf{k}}^L j_{\mathbf{p}}^L\rangle$ would involve the current correlation functions $\langle j_{\mathbf{q}}^{L*} | j_{\mathbf{q}}^L(t) \rangle$ which are negligible in an overdamped Brownian motion, and also that the projections on both $|j_{\mathbf{k}}^L \rho_{\mathbf{p}}\rangle$ and $|j_{\mathbf{k}}^L j_{\mathbf{p}}^L\rangle$ result in zero for our model. Here we remain with the projection to the pair density modes and M_{22}^1 . We use the first mode-coupling approximation [6], and replace $\exp(it\mathcal{Q}\mathcal{L}\mathcal{Q})$ with $\mathcal{P}_M \exp(i\mathcal{L}t)\mathcal{P}_M$:

$$\begin{aligned} M_{22}^1 &\approx \langle A_2^* | \mathcal{L}\mathcal{Q}\mathcal{P}_M^1 \exp(i\mathcal{L}t)\mathcal{P}_M^1 \mathcal{Q}\mathcal{L}A_2 \rangle \\ &= \frac{2}{N\langle \mathbf{v}^2 \rangle} \sum_{\mathbf{k} < \mathbf{p}, \mathbf{k}' < \mathbf{p}'} \frac{\langle j_{\mathbf{q}}^{L*} | \mathcal{L}\mathcal{Q}\rho_{\mathbf{k}'}\rho_{\mathbf{p}'} \rangle \langle \rho_{\mathbf{k}'}^* \rho_{\mathbf{p}'}^* | \exp(i\mathcal{L}t)\rho_{\mathbf{k}}\rho_{\mathbf{p}} \rangle \langle \rho_{\mathbf{k}}^* \rho_{\mathbf{p}}^* | \mathcal{Q}\mathcal{L}j_{\mathbf{q}}^L \rangle}{\langle \rho_{\mathbf{k}}^* \rho_{\mathbf{p}}^* | \rho_{\mathbf{k}}\rho_{\mathbf{p}} \rangle \langle \rho_{\mathbf{k}'}^* \rho_{\mathbf{p}'}^* | \rho_{\mathbf{k}'}\rho_{\mathbf{p}'} \rangle} \end{aligned} \quad (5.72)$$

Also according to the factorization ansatz

$$\langle \rho_{\mathbf{k}}^* \rho_{\mathbf{p}}^* | \rho_{\mathbf{k}}\rho_{\mathbf{p}} \rangle \approx \langle \rho_{\mathbf{k}}^* | \rho_{\mathbf{k}} \rangle \langle \rho_{\mathbf{p}}^* | \rho_{\mathbf{p}} \rangle \quad (5.73)$$

and

$$\begin{aligned} &\langle \rho_{\mathbf{k}'}^* \rho_{\mathbf{p}'}^* | \exp(i\mathcal{L}t)\rho_{\mathbf{k}}\rho_{\mathbf{p}} \rangle \\ &\approx \langle \rho_{\mathbf{k}'}^* | \exp(i\mathcal{L}t)\rho_{\mathbf{k}} \rangle \langle \rho_{\mathbf{p}'}^* | \exp(i\mathcal{L}t)\rho_{\mathbf{p}} \rangle \delta_{\mathbf{k},\mathbf{k}'} \delta_{\mathbf{p},\mathbf{p}'} \\ &= \delta_{\mathbf{k},\mathbf{k}'} \delta_{\mathbf{p},\mathbf{p}'} N^2 S_k S_p \phi_{\mathbf{k}}(t) \phi_{\mathbf{p}}(t), \end{aligned} \quad (5.74)$$

where $\phi_{\mathbf{k}}(t) = \langle \rho_{\mathbf{k}}^* | \exp(i\mathcal{L}t)\rho_{\mathbf{k}} \rangle / N S_k$. We need to calculate two terms, first one:

$$\begin{aligned} \langle j_{\mathbf{q}}^{L*} | \mathcal{L}\mathcal{Q}\rho_{\mathbf{k}}\rho_{\mathbf{p}} \rangle &= \langle j_{\mathbf{q}}^{L*} | \mathcal{L}\rho_{\mathbf{k}}\rho_{\mathbf{p}} \rangle - \langle j_{\mathbf{q}}^{L*} | \mathcal{L}\rho_{\mathbf{q}} \rangle \frac{\langle \rho_{\mathbf{q}}^* | \rho_{\mathbf{k}}\rho_{\mathbf{p}} \rangle}{N S_q} \\ &= \langle j_{\mathbf{q}}^{L*} | (\mathcal{L}\rho_{\mathbf{k}})\rho_{\mathbf{p}} \rangle + \langle j_{\mathbf{q}}^{L*} | \rho_{\mathbf{k}}(\mathcal{L}\rho_{\mathbf{p}}) \rangle - \frac{q\langle \mathbf{v}^2 \rangle}{2S_q} \langle \rho_{\mathbf{q}}^* | \rho_{\mathbf{k}}\rho_{\mathbf{p}} \rangle \\ &= \frac{\langle \mathbf{v}^2 \rangle}{2} k_3 \langle \rho_{\mathbf{q}-\mathbf{k}}^* | \rho_{\mathbf{p}} \rangle + \frac{\langle \mathbf{v}^2 \rangle}{2} p_3 \langle \rho_{\mathbf{q}-\mathbf{p}}^* | \rho_{\mathbf{k}} \rangle - \frac{q\langle \mathbf{v}^2 \rangle}{2S_q} \langle \rho_{\mathbf{q}}^* | \rho_{\mathbf{k}}\rho_{\mathbf{p}} \rangle \\ &= N \frac{\langle \mathbf{v}^2 \rangle}{2} \delta_{\mathbf{q},\mathbf{k}+\mathbf{p}} (k S_p + p S_k - q S_k S_p), \end{aligned} \quad (5.75)$$

where we used the convolution approximation $\langle \rho_{\mathbf{q}}^* | \rho_{\mathbf{k}}\rho_{\mathbf{p}} \rangle = N \delta_{\mathbf{q},\mathbf{k}+\mathbf{p}} S_q S_k S_p$. Above and in the following equations, k and p are the longitudinal components of \mathbf{k} and \mathbf{p} respectively.

The second term is

$$\langle \rho_{\mathbf{k}}^* \rho_{\mathbf{p}}^* | \mathcal{Q}\mathcal{L}j_{\mathbf{q}}^L \rangle = \frac{1}{i} \langle \rho_{\mathbf{k}}^* \rho_{\mathbf{p}}^* | i\mathcal{L}j_{\mathbf{q}}^L \rangle - \langle \rho_{\mathbf{k}}^* \rho_{\mathbf{p}}^* | \rho_{\mathbf{q}} \rangle \frac{1}{N S_q} \langle \rho_{\mathbf{q}}^* | \mathcal{L}j_{\mathbf{q}}^L \rangle. \quad (5.76)$$

In equilibrium or the stationary state, $\langle \rho_{\mathbf{k}}^* \rho_{\mathbf{p}}^* | i\mathcal{L} j_{\mathbf{q}}^L \rangle = \langle (-i\mathcal{L}^\dagger \rho_{\mathbf{k}}^*) \rho_{\mathbf{p}}^* | j_{\mathbf{q}}^L \rangle + \langle \rho_{\mathbf{k}}^* (-i\mathcal{L}^\dagger \rho_{\mathbf{p}}^*) | j_{\mathbf{q}}^L \rangle$ as a result of Eq. (5.43). But here we need to leave the operator \mathcal{L} to operate on the variable $j_{\mathbf{q}}^L$

$$\begin{aligned} \frac{1}{i} \langle \rho_{\mathbf{k}}^* \rho_{\mathbf{p}}^* | i\mathcal{L} j_{\mathbf{q}}^L \rangle &= \frac{1}{i} \langle \rho_{\mathbf{k}}^* \rho_{\mathbf{p}}^* | \sum_i \mathbf{v}_i \cdot \frac{\partial}{\partial \mathbf{r}_i} j_{\mathbf{q}}^L \rangle \\ &+ \frac{1}{i} \langle \rho_{\mathbf{k}}^* \rho_{\mathbf{p}}^* | \sum_i \mathbf{F}_i \cdot \frac{\partial}{\partial \mathbf{v}_i} j_{\mathbf{q}}^L \rangle \\ &- \frac{1}{i} \langle \rho_{\mathbf{k}}^* \rho_{\mathbf{p}}^* | \sum_i (-\alpha + \mathbf{v}_i^2) \mathbf{v}_i \cdot \frac{\partial}{\partial \mathbf{v}_i} j_{\mathbf{q}}^L \rangle. \end{aligned} \quad (5.77)$$

The third term is zero since the odd moments of velocity are zero. The first term can be written as

$$\begin{aligned} \frac{1}{i} \langle \rho_{\mathbf{k}}^* \rho_{\mathbf{p}}^* | \sum_i \mathbf{v}_i \cdot \frac{\partial}{\partial \mathbf{r}_i} j_{\mathbf{q}}^L \rangle &= \frac{1}{i} \langle \rho_{\mathbf{k}}^* \rho_{\mathbf{p}}^* | \sum_i \left(\mathbf{v}_i \cdot \frac{\partial}{\partial \mathbf{r}_i} \right) \sum_m v_m^L \exp(i\mathbf{q} \cdot \mathbf{r}_m) \rangle \\ &= \frac{q \langle \mathbf{v}^2 \rangle}{2} \langle \rho_{\mathbf{k}}^* \rho_{\mathbf{p}}^* | \rho_{\mathbf{q}} \rangle. \end{aligned} \quad (5.78)$$

With the use of Eq. (5.62) and (5.63) the second term of Eq. (5.77) can be written as

$$\begin{aligned} &\frac{1}{i} \langle \rho_{\mathbf{k}}^* \rho_{\mathbf{p}}^* | \sum_i \mathbf{F}_i \cdot \frac{\partial}{\partial \mathbf{v}_i} j_{\mathbf{q}}^L \rangle \\ &= \frac{1}{i} \langle \rho_{\mathbf{k}}^* \rho_{\mathbf{p}}^* | \sum_i F_i^L \exp(i\mathbf{q} \cdot \mathbf{r}_i) \rangle \\ &= \frac{\langle \mathbf{v}^2 \rangle}{2i} \sum_i \int d\Gamma \frac{\partial f}{\partial r_i^L} \exp(i\mathbf{q} \cdot \mathbf{r}_i) \rho_{\mathbf{k}}^* \rho_{\mathbf{p}}^* \\ &= -\frac{\langle \mathbf{v}^2 \rangle}{2i} \sum_i \int d\Gamma f \frac{\partial}{\partial r_i^L} [\exp(i\mathbf{q} \cdot \mathbf{r}_i) \rho_{\mathbf{k}}^* \rho_{\mathbf{p}}^*] \\ &= -\frac{\langle \mathbf{v}^2 \rangle}{2i} \sum_i \int d\Gamma f [iq \exp(i\mathbf{q} \cdot \mathbf{r}_i) \rho_{\mathbf{k}}^* \rho_{\mathbf{p}}^* - ik \exp(i(\mathbf{q} - \mathbf{k}) \cdot \mathbf{r}_i) \rho_{\mathbf{p}}^* \\ &\quad - ip \exp(i(\mathbf{q} - \mathbf{p}) \cdot \mathbf{r}_i) \rho_{\mathbf{k}}^*] \\ &= -\frac{\langle \mathbf{v}^2 \rangle}{2} [q \langle \rho_{\mathbf{k}}^* \rho_{\mathbf{p}}^* | \rho_{\mathbf{q}} \rangle - \delta_{\mathbf{q}, \mathbf{k} + \mathbf{p}} N k S_p - \delta_{\mathbf{q}, \mathbf{k} + \mathbf{p}} N p S_k]. \end{aligned} \quad (5.79)$$

By adding up the Eq. (5.79) to Eq. (5.78) we have

$$\frac{1}{i} \langle \rho_{\mathbf{k}}^* \rho_{\mathbf{p}}^* | i\mathcal{L} j_{\mathbf{q}}^L \rangle = N \frac{\langle \mathbf{v}^2 \rangle}{2} \delta_{\mathbf{q}, \mathbf{k} + \mathbf{p}} (k S_p + p S_k), \quad (5.80)$$

so

$$\langle \rho_{\mathbf{k}}^* \rho_{\mathbf{p}}^* | \mathcal{Q} \mathcal{L} j_{\mathbf{q}}^L \rangle = N \frac{\langle \mathbf{v}^2 \rangle}{2} \delta_{\mathbf{q}, \mathbf{k} + \mathbf{p}} (k S_p + p S_k - q S_k S_p). \quad (5.81)$$

Placing Eq. (5.73), (5.74), (5.75) and (5.81) in Eq. (5.72) leads to

$$M_{22}^1 = \frac{\langle \mathbf{v}^2 \rangle}{2N} \sum_{\mathbf{k} < \mathbf{p}} \delta_{\mathbf{q}, \mathbf{k} + \mathbf{p}} \left(\frac{k S_p + p S_k - q S_k S_p}{S_k S_p} \right)^2 S_k S_p \phi_{\mathbf{k}}(t) \phi_{\mathbf{p}}(t). \quad (5.82)$$

The expression for the kernel is the same as the MCT kernel for conventional liquids [6] with the only difference that here we have the effective temperature $k_B T_{\text{Eff}} = \langle \mathbf{v}^2 \rangle / 2$ instead of the $k_B T$. $\langle \mathbf{v}^2 \rangle / 2$ depends on the α and D_v through Eq. (5.22). The effective temperature will drop out by defining

$$m_q^{mc} = \frac{1}{\Omega_{12}^2} M_{22}^1. \quad (5.83)$$

Therefore the activity does not have any effect on the MCT kernel. Later in section 5.9 we show that it is possible to introduce some activity effects into the structure factor.

m_q^{mc} can be written in the integral form. The $\sum_{\mathbf{k} < \mathbf{p}}$ can be written as $\frac{1}{2} \sum_{\mathbf{k}, \mathbf{p}}$ in the thermodynamic limit. In two dimensions

$$L^{-2} \sum_{\mathbf{k}} \rightarrow \frac{1}{(2\pi)^2} \int d^2 k, \quad (5.84)$$

where $L^{-2} = \rho / N$ and ρ is the average density for N particles in an area L^2 . Thus the kernel in two dimensions can be written as

$$m_q^{\text{mct}} = \int \frac{d^2 k}{(2\pi)^2} \frac{\rho S_q S_p S_k}{2q^4} [\mathbf{q} \cdot \mathbf{k} c_k + \mathbf{p} \cdot \mathbf{q} c_p]^2 \delta(\mathbf{q} - \mathbf{k} - \mathbf{p}) \phi_k(t) \phi_p(t), \quad (5.85)$$

where $S_k = \frac{1}{1 - \rho c_k}$. The kernel is the same as the two dimensional case in [41].

5.7. Equation of Motion for Density Auto-Correlation Function

One can write the equation of motion following Eq. (5.53), (5.69) and (5.85) as:

$$\partial_t^2 \phi_{\mathbf{q}}(t) + \frac{D_v}{\langle \mathbf{v}^2 \rangle} \partial_t \phi_{\mathbf{q}}(t) + \Omega_q^2 \phi_{\mathbf{q}}(t) + \Omega_q^2 \int_0^t \partial_{t'} \phi_{\mathbf{q}}(t') m_q^{\text{mct}}(t-t') dt' = 0 \quad (5.86)$$

where $\phi_{\mathbf{q}}(t) = \phi_{11}(t)$ and $\Omega_q^2 = \Omega_{12}^2 = q^2 \langle \mathbf{v}^2 \rangle / (2S_q)$. Here the kernel is only the MCT part and we did not consider any regular or white noise term. For the overdamped case the equation of motion can be written as

$$\frac{D_v}{\langle \mathbf{v}^2 \rangle \Omega_q^2} \partial_t \phi_{\mathbf{q}}(t) + \phi_{\mathbf{q}}(t) + \int_0^t \partial_{t'} \phi_{\mathbf{q}}(t') m_q^{\text{mct}}(t-t') dt' = 0. \quad (5.87)$$

One should have in mind that the equation of motion presented as Eq. (5.86), contains one more approximation in comparison to the overdamped case in Eq. (5.87). The reason is that in calculating Ω_{22} in Eq. (5.66), we have used the property of the Langevin equation with overdamped motion in Eq. (5.31).

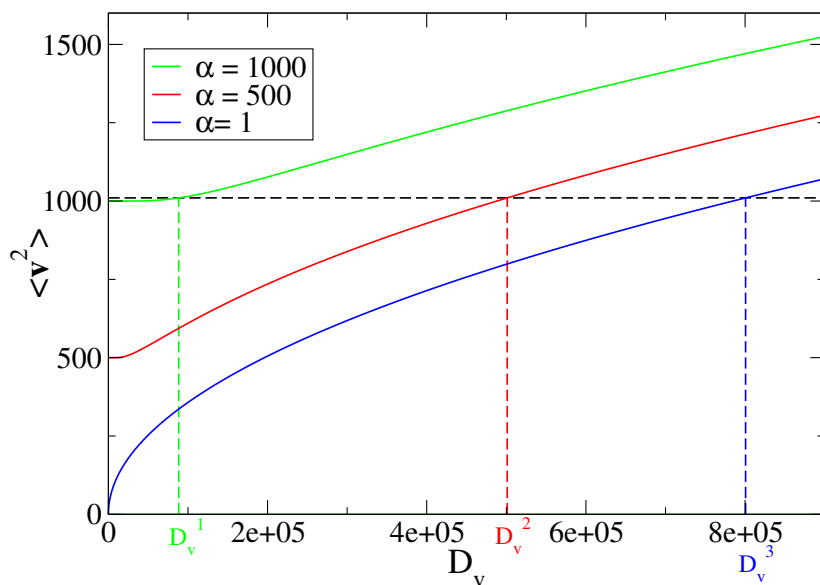


Figure 5.7.: Second moment of velocity against noise strength D_v according to Eq. (5.22) for different values of α . When $\langle \mathbf{v}^2 \rangle = 2k_B T_{\text{Eff}} = 1010$, the noise strength $D_v^1 = 88385.66$, $D_v^2 = 501096.48$ and $D_v^3 = 800608.13$ for $\alpha = 1000$, 500 and 1 correspondingly. The smaller the D_v the higher is the activity of the system.

Since the m_q^{mct} here is the same as the kernel in case of normal Brownian motion, the glass transition packing fraction will also not change. But the damping coefficient

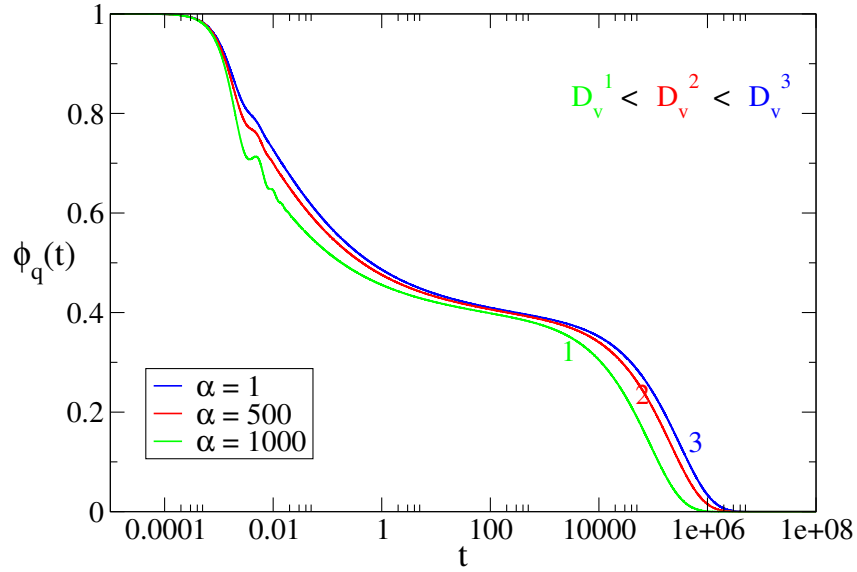


Figure 5.8.: The density correlation function $\phi_q(t)$ according to Eq. (5.86) for $q = 4.2$ and packing fraction $\varphi = 0.73370$ equivalent to $\varepsilon = (\varphi - \varphi_c)/\varphi_c \simeq 0.0002$, when $\langle \mathbf{v}^2 \rangle = 2k_B T_{\text{Eff}} = 1010$ and $D_v^1 = 88385.66$, $D_v^2 = 501096.48$ and $D_v^3 = 800608.13$. The higher the activity of the system (larger α and smaller D_v) the faster the correlation function decays.

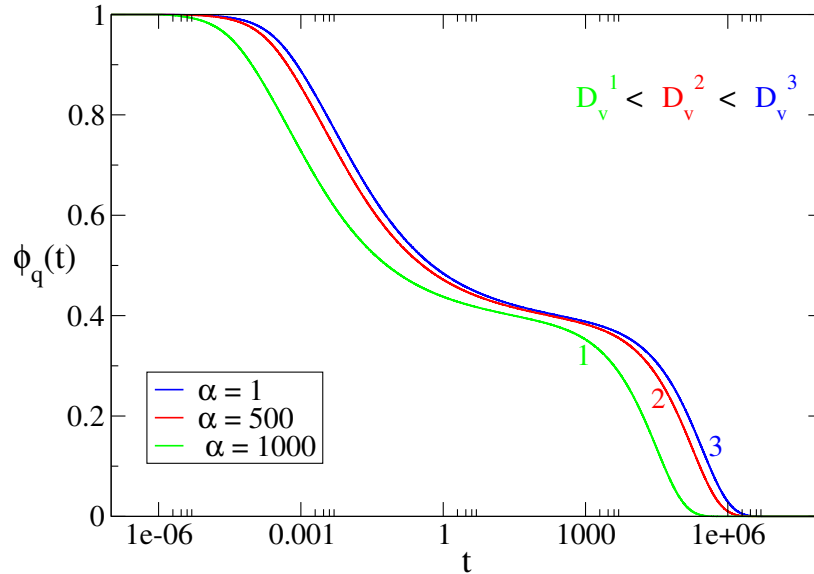


Figure 5.9.: The density correlation function $\phi_q(t)$ according to Eq. (5.87) for overdamped motion for $q = 4.2$ and packing fraction $\varphi = 0.73370$ equivalent to $\varepsilon = (\varphi - \varphi_c)/\varphi_c \simeq 0.0002$, when $\langle \mathbf{v}^2 \rangle = 2k_B T_{\text{Eff}} = 1010$ and $D_v^1 = 88385.66$, $D_v^2 = 501096.48$ and $D_v^3 = 800608.13$. The higher the activity of the system (larger α and smaller D_v) the faster the correlation function decays.

in both Eq. (5.86) and (5.87) is different from the equilibrium case. We use the Baus-Colot [41, 116] analytical expression for the structure factor of the hard-sphere system in two dimensions to solve the equations of motion. The glass transition happens at the critical packing fraction $\varphi_c = 0.73382$. We have used 100 grid points in the range $q_{\min} = 0.2$ to $q_{\max} = 39.8$ to solve the integral equations.

We show in Fig. 5.7 that the constant value of the effective temperature or $\langle \mathbf{v}^2 \rangle$ can result in different values of D_v corresponding to different values of α . In Fig. 5.7, we choose the temperature $\langle \mathbf{v}^2 \rangle = 2k_B T_{\text{Eff}} = 1010$ and we consider three pairs of parameters $(\alpha, D_v) = (1000, 88385.66), (500, 501096.48), (1, 800608.13)$ with the mentioned temperature. As we discussed in section 5.3.3, the particles with smaller velocity than $\sqrt{\alpha}$, have negative friction and are active. We use Eq. (5.35) to obtain the probability of finding active particle in the system for these three different pair of parameters. The resulting value are $P_{\text{active}} = 0.0006, 0.2767$ and 0.4956 for $(\alpha = 1, D_v = 800608.13)$, $(\alpha = 500, D_v = 501096.48)$ and $(\alpha = 1000, D_v = 88385.66)$ respectively. For a constant temperature the larger the α (or the smaller is the D_v), the higher the probability of finding active particles in the system. In Fig. 5.8 the solution of the Eq. (5.86) for $\phi_q(t)$ with the packing fraction $\varphi_c = 0.73370$ in the liquid state and close to transition is presented for the three pairs of (α, D_v) . The higher the probability of finding active particles in the system, the smaller the time that the correlation function decay to zero. The same thing happens in the overdamped case. Fig. 5.9 shows the same result for the Brownian (overdamped) motion in Eq. (5.87).

In summery, since the memory kernel does not change in the presented model, the activity does not effect the glass transition packing fraction which means; activity does not melt the glass. But it can shift the correlation function in the way that for a constant temperature and below the glass transition packing fraction, the higher is the probability of finding active particles in the system, the smaller is the time that the correlation function decays to zero. For a better comparison we use the second scaling law (α -scaling) [6]. We scale the time in the correlation functions shown in Fig. 5.8, in a way that all three correlations fall on top each other in the long time regime. The scaling follows

$$\phi_q(\tilde{t}) = \phi_q\left(\frac{t}{\tau(D_v)}\right), \quad (5.88)$$

where $\tau(D_v)$ is the scaling time dependent on D_v . For the correlation function corresponding to $(\alpha = 1000, D_v = 88385.66)$ the $\tau(D_v) = 0.282$, for $(\alpha = 500, D_v =$

501096.48) the $\tau(D_v) = 0.681$ and for $(\alpha = 1, D_v = 800608.13)$ the $\tau(D_v) = 1$. The scaled correlation functions are shown in Fig. 5.10. Except the short time dynamic the rest of the correlation function falls on top of each other. One should have in mind that the scaling time $\tau(D_v)$ will not diverge, since the glass transition packing fraction is not dependent on activity and in any case in the packing fraction below φ_c , the correlation function will always decay to zero.

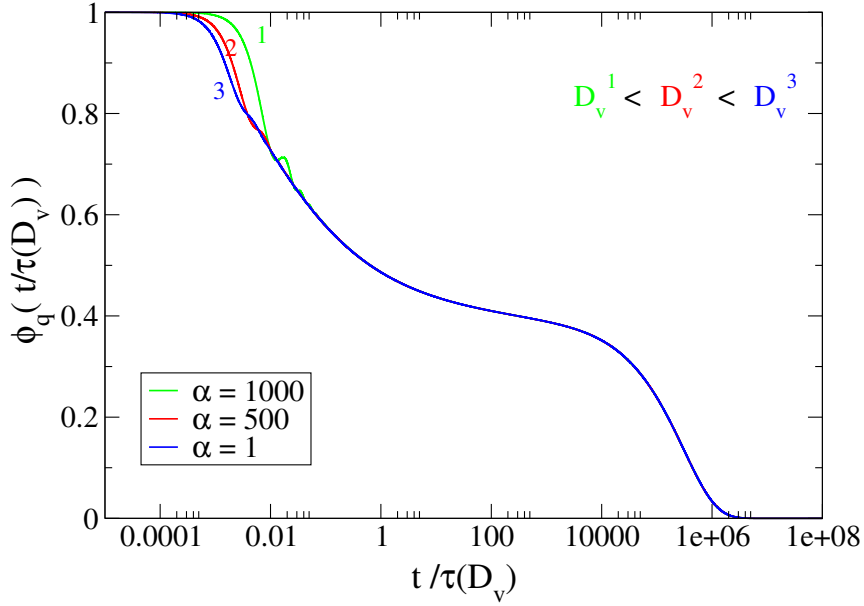


Figure 5.10.: The scaled density correlation function $\phi_q(\tilde{t})$ according to Eq. (5.88) for $q = 4.2$ and packing fraction $\varphi = 0.73370$ equivalent to $\varepsilon = (\varphi - \varphi_c)/\varphi_c \simeq 0.0002$, when $\langle \mathbf{v}^2 \rangle = 2k_B T_{\text{Eff}} = 1010$. For $(\alpha = 1, D_v^3 = 800608.13)$ the $\tau(D_v) = 1$, for $(\alpha = 500, D_v^2 = 501096.48)$ the $\tau(D_v) = 0.681$ and for $(\alpha = 1000, D_v^1 = 88385.66)$ the $\tau(D_v) = 0.282$. The scaling time $\tau(D_v)$ will not diverge, since the glass transition packing fraction is not dependent on activity and in any case in the packing fraction below φ_c , the correlation function will always decay to zero.

5.8. Kernel Projection on Density-Current and Current-Current Pairs

In this section we calculate the projection of the memory kernel on to the current-density $|j_{\mathbf{k}}^L \rho_{\mathbf{p}}\rangle$, and current-current $|j_{\mathbf{k}}^L j_{\mathbf{p}}^L\rangle$ pairs, related to second and third term in Eq. (5.71). As we show in the following, in both of these projections the correlation function $\langle j_{\mathbf{k}}^{L*} | j_{\mathbf{k}}^L(t) \rangle$ appears. Via the continuity equation, $\langle j_{\mathbf{k}}^{L*} | j_{\mathbf{k}}^L(t) \rangle$ is proportional to the second derivative of density correlation function which vanishes in the overdamped Brownian motion. Therefore we expect these projection not to

play an important role in the equation of motion. Still, the calculated M_{22}^2 and M_{22}^3 is presented in this section since we want to show that their values are zero within the mode-coupling approximation. The projection of the memory kernel M_{22} on the current-density pair results in

$$M_{22}^2 \approx \langle A_2^* | \mathcal{L} \mathcal{Q} \mathcal{P}_M^2 \exp(i\mathcal{L}t) \mathcal{P}_M^2 \mathcal{Q} \mathcal{L} A_2 \rangle$$

$$= \frac{2}{N \langle \mathbf{v}^2 \rangle} \sum_{\mathbf{k} < \mathbf{p}, \mathbf{k}' < \mathbf{p}'} \frac{\langle j_{\mathbf{q}}^{L*} | \mathcal{L} \mathcal{Q} j_{\mathbf{k}'}^L \rho_{\mathbf{p}'} \rangle \langle j_{\mathbf{k}'}^{L*} \rho_{\mathbf{p}'}^* | \exp(i\mathcal{L}t) j_{\mathbf{k}}^L \rho_{\mathbf{p}} \rangle \langle j_{\mathbf{k}}^{L*} \rho_{\mathbf{p}}^* | \mathcal{Q} \mathcal{L} j_{\mathbf{q}}^L \rangle}{\langle j_{\mathbf{k}}^{L*} \rho_{\mathbf{p}}^* | j_{\mathbf{k}}^L \rho_{\mathbf{p}} \rangle \langle j_{\mathbf{k}'}^{L*} \rho_{\mathbf{p}'}^* | j_{\mathbf{k}'}^L \rho_{\mathbf{p}'} \rangle}. \quad (5.89)$$

According to the factorization ansatz

$$\langle j_{\mathbf{k}}^{L*} \rho_{\mathbf{p}}^* | j_{\mathbf{k}}^L \rho_{\mathbf{p}} \rangle \approx \langle j_{\mathbf{k}}^{L*} | j_{\mathbf{k}}^L \rangle \langle \rho_{\mathbf{p}}^* | \rho_{\mathbf{p}} \rangle$$

$$= N^2 \frac{\langle \mathbf{v}^2 \rangle}{2} S_p, \quad (5.90)$$

and

$$\langle j_{\mathbf{k}'}^{L*} \rho_{\mathbf{p}'}^* | \exp(i\mathcal{L}t) j_{\mathbf{k}}^L \rho_{\mathbf{p}} \rangle \approx \langle j_{\mathbf{k}'}^{L*} | \exp(i\mathcal{L}t) j_{\mathbf{k}}^L \rangle \langle \rho_{\mathbf{p}'}^* | \exp(i\mathcal{L}t) \rho_{\mathbf{p}} \rangle \delta_{\mathbf{k}, \mathbf{k}'} \delta_{\mathbf{p}, \mathbf{p}'}$$

$$= \delta_{\mathbf{k}, \mathbf{k}'} \delta_{\mathbf{p}, \mathbf{p}'} N^2 \frac{\langle \mathbf{v}^2 \rangle}{2} S_p \psi_{\mathbf{k}}(t) \phi_{\mathbf{p}}(t), \quad (5.91)$$

where $\psi_{\mathbf{k}}(t) = 2 \langle j_{\mathbf{k}}^{L*} | \exp(i\mathcal{L}t) j_{\mathbf{k}}^L \rangle / N \langle \mathbf{v}^2 \rangle$. From Eq. (5.53) one can conclude

$$\psi = \frac{z}{\Omega_{\mathbf{k}}^2} (1 + z\phi). \quad (5.92)$$

If we assume $\partial_t \phi_{\mathbf{k}}(t=0) = 0$ and $\phi_{\mathbf{k}}(t=0) = 1$ in the time domain, as it is normally used to solve the MCT equations [6], we have

$$\psi_{\mathbf{k}}(t) = -\frac{1}{\Omega_{\mathbf{k}}^2} \frac{\partial^2 \phi_{\mathbf{k}}(t)}{\partial t^2}, \quad (5.93)$$

which is a form of the continuity equation for the density auto correlation function. In a Brownian over damped motion the second time derivative of the density auto correlation vanishes, thus we expect M_{22}^2 to vanish too. We still calculate M_{22}^2 , to show that M_{22}^2 is zero irrespective of that fact.

$$\langle j_{\mathbf{q}}^{L*} | \mathcal{L} \mathcal{Q} j_{\mathbf{k}}^L \rho_{\mathbf{p}} \rangle = \langle j_{\mathbf{q}}^{L*} | \mathcal{L} j_{\mathbf{k}}^L \rho_{\mathbf{p}} \rangle - \langle j_{\mathbf{q}}^{L*} | \mathcal{L} \rho_{\mathbf{q}} \rangle \frac{\langle \rho_{\mathbf{q}}^* | j_{\mathbf{k}}^L \rho_{\mathbf{p}} \rangle}{N S_q} - \langle j_{\mathbf{q}}^{L*} | \mathcal{L} j_{\mathbf{q}}^L \rangle \frac{\langle j_{\mathbf{q}}^{L*} | j_{\mathbf{k}}^L \rho_{\mathbf{p}} \rangle}{N \langle \mathbf{v}^2 \rangle / 2}$$

$$= \langle j_{\mathbf{q}}^{L*} | (\mathcal{L} j_{\mathbf{k}}^L) \rho_{\mathbf{p}} \rangle - \langle j_{\mathbf{q}}^{L*} | \mathcal{L} j_{\mathbf{q}}^L \rangle \frac{\langle j_{\mathbf{q}}^{L*} | j_{\mathbf{k}}^L \rho_{\mathbf{p}} \rangle}{N \langle \mathbf{v}^2 \rangle / 2}. \quad (5.94)$$

The terms $\langle j_{\mathbf{q}}^{L*} | j_{\mathbf{k}}^L(\mathcal{L}\rho_{\mathbf{p}}) \rangle$ and $\langle j_{\mathbf{q}}^{L*} | \mathcal{L}\rho_{\mathbf{q}} \rangle \langle \rho_{\mathbf{q}}^* | j_{\mathbf{k}}^L \rho_{\mathbf{p}} \rangle / NS_{\mathbf{q}}$ are considered zero since the odd moments of velocity are zero. The first term in the right hand side of Eq. (5.94) can be written as follows using Eq. (5.13),

$$\begin{aligned} \frac{1}{i} \langle j_{\mathbf{q}}^{L*} | (i\mathcal{L}j_{\mathbf{k}}^L) \rho_{\mathbf{p}} \rangle &= \frac{1}{i} \langle j_{\mathbf{q}}^{L*} | \left(\sum_i \mathbf{v}_i \cdot \frac{\partial}{\partial \mathbf{r}_i} j_{\mathbf{k}}^L \right) \rho_{\mathbf{p}} \rangle \\ &+ \frac{1}{i} \langle j_{\mathbf{q}}^{L*} | \left(\sum_i \mathbf{F}_i \cdot \frac{\partial}{\partial \mathbf{v}_i} j_{\mathbf{k}}^L \right) \rho_{\mathbf{p}} \rangle \\ &- \frac{1}{i} \langle j_{\mathbf{q}}^{L*} | \left(\sum_i (-\alpha + \mathbf{v}_i^2) \mathbf{v}_i \cdot \frac{\partial}{\partial \mathbf{v}_i} j_{\mathbf{k}}^L \right) \rho_{\mathbf{p}} \rangle. \end{aligned} \quad (5.95)$$

In the last equation again the first term is zero because it contains the average of the first power of velocity. The second term of Eq. (5.95), in case of constant friction and equilibrium can be written as

$$\begin{aligned} &\frac{1}{i} \langle j_{\mathbf{q}}^{L*} | \left(\sum_i \mathbf{F}_i \cdot \frac{\partial}{\partial \mathbf{v}_i} j_{\mathbf{k}}^L \right) \rho_{\mathbf{p}} \rangle \\ &= \frac{1}{i} \langle j_{\mathbf{q}}^{L*} | \sum_i F_i^L \exp(i\mathbf{k} \cdot \mathbf{r}_i) \rho_{\mathbf{p}} \rangle \\ &= \frac{\langle \mathbf{v}^2 \rangle}{2i} \sum_i \int d\Gamma \frac{\partial f}{\partial r_i^L} \exp(i\mathbf{k} \cdot \mathbf{r}_i) j_{\mathbf{q}}^{L*} \rho_{\mathbf{p}} \\ &= -\frac{\langle \mathbf{v}^2 \rangle}{2i} \sum_i \int d\Gamma f \frac{\partial}{\partial r_i^L} [\exp(i\mathbf{k} \cdot \mathbf{r}_i) j_{\mathbf{q}}^{L*} \rho_{\mathbf{p}}] \\ &= -\frac{\langle \mathbf{v}^2 \rangle}{2i} \sum_i \int d\Gamma [ik \exp(i\mathbf{k} \cdot \mathbf{r}_i) j_{\mathbf{q}}^{L*} \rho_{\mathbf{p}} - iqv_i^L \exp(i(\mathbf{k} - \mathbf{q}) \cdot \mathbf{r}_i) \rho_{\mathbf{p}} \\ &\quad + ip \exp(i(\mathbf{k} + \mathbf{p}) \cdot \mathbf{r}_i) j_{\mathbf{q}}^{L*}] \\ &= -\frac{\langle \mathbf{v}^2 \rangle}{2} [k \langle \rho_{\mathbf{k}} j_{\mathbf{q}}^{L*} | \rho_{\mathbf{p}} \rangle - q \langle j_{\mathbf{k}-\mathbf{q}}^L | \rho_{\mathbf{p}} \rangle + p \langle j_{\mathbf{q}}^{L*} | \rho_{\mathbf{k}+\mathbf{p}} \rangle] = 0, \end{aligned} \quad (5.96)$$

where we used Eq. (5.62) and Eq. (5.63). The fact that we obtained zero here as the answer is due to the fact that in case of equilibrium $\sum_i \mathbf{F}_i \cdot \mathbf{v}_i = 0$. According

to the Eq. (5.31) and (5.67) for the nonlinear Langevin equation we can write:

$$\begin{aligned}
& \frac{1}{i} \langle j_{\mathbf{q}}^{L*} | (\sum_i \mathbf{F}_i \cdot \frac{\partial}{\partial \mathbf{v}_i} j_{\mathbf{k}}^L) \rho_{\mathbf{p}} \rangle \\
&= \frac{1}{i} \langle j_{\mathbf{q}}^{L*} | \sum_i F_i^L \exp(i\mathbf{k} \cdot \mathbf{r}_i) \rho_{\mathbf{p}} \rangle \\
&= -i \langle \sum_i v_i^L F_i^L \exp(-i(\mathbf{q} - \mathbf{k})) \rho_{\mathbf{p}} \rangle \\
&= -i \langle v^L F^L \rangle \langle \rho_{\mathbf{q}-\mathbf{k}}^* | \rho_{\mathbf{p}} \rangle = -iN \frac{D_v}{2} S_p \delta_{\mathbf{q}, \mathbf{k}+\mathbf{p}}.
\end{aligned} \tag{5.97}$$

Therefore $\frac{1}{i} \langle j_{\mathbf{q}}^{L*} | (\sum_i \mathbf{F}_i \cdot \frac{\partial}{\partial \mathbf{v}_i} j_{\mathbf{k}}^L) \rho_{\mathbf{p}} \rangle$ in our system is actually not zero.

The third term of Eq. (5.95) is

$$\begin{aligned}
& -\frac{1}{i} \langle j_{\mathbf{q}}^{L*} | (\sum_i (-\alpha + \mathbf{v}_i^2) \mathbf{v}_i \cdot \frac{\partial}{\partial \mathbf{v}_i} j_{\mathbf{k}}^L) \rho_{\mathbf{p}} \rangle \\
&= -\frac{1}{i} \langle j_{\mathbf{q}}^{L*} | \sum_i (-\alpha + \mathbf{v}_i^2) v_i^L \exp(i\mathbf{k} \cdot \mathbf{r}_i) \rho_{\mathbf{p}} \rangle \\
&= -\frac{1}{i} \langle \sum_m (-\alpha) v_m^{L2} \exp(-i(\mathbf{q} - \mathbf{k}) \cdot \mathbf{r}_m) \rho_{\mathbf{p}} \rangle \\
&\quad - \frac{1}{i} \langle \sum_m v_m^{L2} \mathbf{v}_m^2 \exp(-i(\mathbf{q} - \mathbf{k}) \cdot \mathbf{r}_m) \rho_{\mathbf{p}} \rangle \\
&= \frac{\alpha}{i} \langle v^{L2} \rangle \langle \rho_{\mathbf{q}-\mathbf{k}}^* | \rho_{\mathbf{p}} \rangle - \frac{1}{i} \langle \mathbf{v}^2 v^{L2} \rangle \langle \rho_{\mathbf{q}-\mathbf{k}}^* | \rho_{\mathbf{p}} \rangle \\
&= \frac{-i}{2} (\alpha \langle \mathbf{v}^2 \rangle - \langle \mathbf{v}^4 \rangle) N S_p \delta_{\mathbf{q}, \mathbf{k}+\mathbf{p}} = i D_v N S_p \delta_{\mathbf{q}, \mathbf{k}+\mathbf{p}}.
\end{aligned} \tag{5.98}$$

Also

$$\langle j_{\mathbf{q}}^{L*} | j_{\mathbf{k}}^L \rho_{\mathbf{p}} \rangle = N \frac{\langle \mathbf{v}^2 \rangle}{2} \langle \rho_{\mathbf{q}-\mathbf{k}}^* | \rho_{\mathbf{p}} \rangle = N \frac{\langle \mathbf{v}^2 \rangle}{2} S_p \delta_{\mathbf{q}, \mathbf{k}+\mathbf{p}}. \tag{5.99}$$

Therefore by substitution of Eq. (5.97) and (5.98) in (5.95) and Eq. (5.95), (5.99) and (5.68) in Eq. (5.94) we have

$$\langle j_{\mathbf{q}}^{L*} | \mathcal{L} Q j_{\mathbf{k}}^L \rho_{\mathbf{p}} \rangle = 0, \tag{5.100}$$

which shows that M_{22}^2 , the projection of the kernel on the current-density pair, is zero.

Now we start with calculating M_{22}^3 , the projected component of M_{22} on the

current-current pair $|j_p^L j_k^L\rangle$.

$$\begin{aligned} M_{22}^3 &\approx \langle A_2^* | \mathcal{L} \mathcal{Q} \mathcal{P}_M^3 \exp(i\mathcal{L}t) \mathcal{P}_M^3 \mathcal{Q} \mathcal{L} A_2 \rangle \\ &= \frac{2}{N \langle \mathbf{v}^2 \rangle} \sum_{\mathbf{k} < \mathbf{p}, \mathbf{k}' < \mathbf{p}'} \frac{\langle j_{\mathbf{q}}^{L*} | \mathcal{L} \mathcal{Q} j_{\mathbf{k}}^L j_{\mathbf{p}'}^L \rangle \langle j_{\mathbf{k}'}^{L*} j_{\mathbf{p}'}^{L*} | \exp(i\mathcal{L}t) j_{\mathbf{k}}^L j_{\mathbf{p}}^L \rangle \langle j_{\mathbf{k}}^{L*} j_{\mathbf{p}}^{L*} | \mathcal{Q} \mathcal{L} j_{\mathbf{q}}^L \rangle}{\langle j_{\mathbf{k}}^{L*} j_{\mathbf{p}}^{L*} | j_{\mathbf{k}}^L j_{\mathbf{p}}^L \rangle \langle j_{\mathbf{k}'}^{L*} j_{\mathbf{p}'}^{L*} | j_{\mathbf{k}'}^L j_{\mathbf{p}'}^L \rangle}, \end{aligned} \quad (5.101)$$

where

$$\langle j_{\mathbf{k}}^{L*} j_{\mathbf{p}}^{L*} | j_{\mathbf{k}}^L j_{\mathbf{p}}^L \rangle \approx \langle j_{\mathbf{k}}^{L*} | j_{\mathbf{k}}^L \rangle \langle j_{\mathbf{p}}^{L*} | j_{\mathbf{p}}^L \rangle = N^2 \frac{\langle \mathbf{v}^2 \rangle^2}{4}, \quad (5.102)$$

and

$$\begin{aligned} &\langle j_{\mathbf{k}'}^{L*} j_{\mathbf{p}'}^{L*} | \exp(i\mathcal{L}t) j_{\mathbf{k}}^L j_{\mathbf{p}}^L \rangle \\ &\approx \langle j_{\mathbf{k}'}^{L*} | \exp(i\mathcal{L}t) j_{\mathbf{k}}^L \rangle \langle j_{\mathbf{p}'}^{L*} | \exp(i\mathcal{L}t) j_{\mathbf{p}}^L \rangle \delta_{\mathbf{k}, \mathbf{k}'} \delta_{\mathbf{p}, \mathbf{p}'} \\ &= \delta_{\mathbf{k}, \mathbf{k}'} \delta_{\mathbf{p}, \mathbf{p}'} N^2 \frac{\langle \mathbf{v}^2 \rangle^2}{4} \psi_{\mathbf{k}}(t) \psi_{\mathbf{p}}(t). \end{aligned} \quad (5.103)$$

We need to calculate

$$\langle j_{\mathbf{q}}^{L*} | \mathcal{L} \mathcal{Q} j_{\mathbf{k}}^L j_{\mathbf{p}}^L \rangle = \frac{1}{i} \langle j_{\mathbf{q}}^{L*} | (i\mathcal{L} j_{\mathbf{k}}^L) j_{\mathbf{p}}^L \rangle + \frac{1}{i} \langle j_{\mathbf{q}}^{L*} | j_{\mathbf{k}}^L (i\mathcal{L} j_{\mathbf{p}}^L) \rangle - \frac{1}{N S_{\mathbf{q}}} \langle j_{\mathbf{q}}^{L*} | \mathcal{L} \rho_{\mathbf{q}} \rangle \langle \rho_{\mathbf{q}}^* | j_{\mathbf{k}}^L j_{\mathbf{p}}^L \rangle, \quad (5.104)$$

where we already ignored the term which is zero because of the average of the odd moment of the velocity.

$$\begin{aligned} \frac{1}{i} \langle j_{\mathbf{q}}^{L*} | (i\mathcal{L} j_{\mathbf{k}}^L) j_{\mathbf{p}}^L \rangle &= \frac{1}{i} \langle j_{\mathbf{q}}^{L*} | \left(\sum_i \mathbf{v}_i \cdot \frac{\partial}{\partial \mathbf{r}_i} j_{\mathbf{k}}^L \right) j_{\mathbf{p}}^L \rangle \\ &+ \frac{1}{i} \langle j_{\mathbf{q}}^{L*} | \left(\sum_i \mathbf{F}_i \cdot \frac{\partial}{\partial \mathbf{v}_i} j_{\mathbf{k}}^L \right) j_{\mathbf{p}}^L \rangle \\ &- \frac{1}{i} \langle j_{\mathbf{q}}^{L*} | \left(\sum_i (-\alpha + \mathbf{v}_i^2) \mathbf{v}_i \cdot \frac{\partial}{\partial \mathbf{v}_i} j_{\mathbf{k}}^L \right) j_{\mathbf{p}}^L \rangle. \end{aligned} \quad (5.105)$$

The third term in the last equation is zero. The first term can be written as

$$\frac{1}{i} \langle j_{\mathbf{q}}^{L*} | \left(\sum_i \mathbf{v}_i \cdot \frac{\partial}{\partial \mathbf{r}_i} j_{\mathbf{k}}^L \right) j_{\mathbf{p}}^L \rangle = k \langle v^{L2} \rangle^2 \langle \rho_{\mathbf{q}-\mathbf{p}}^* | \rho_{\mathbf{k}} \rangle = N \delta_{\mathbf{q}, \mathbf{k}+\mathbf{p}} \frac{\langle \mathbf{v}^2 \rangle^2}{4} k S_{\mathbf{k}}. \quad (5.106)$$

The second term using the same method as in Eq. (5.79) will result in

$$\begin{aligned}
& + \frac{1}{i} \langle j_{\mathbf{q}}^{L*} | (\sum_i \mathbf{F}_i \cdot \frac{\partial}{\partial \mathbf{v}_i} j_{\mathbf{k}}^L) j_{\mathbf{p}}^L \rangle \\
& = -\frac{\langle \mathbf{v}^2 \rangle}{2} (k \frac{\langle \mathbf{v}^2 \rangle}{2} \langle \rho_{\mathbf{q}-\mathbf{p}}^* | \rho_{\mathbf{k}} \rangle - qN \frac{\langle \mathbf{v}^2 \rangle}{2} \delta_{\mathbf{q}, \mathbf{k}+\mathbf{p}} + pN \frac{\langle \mathbf{v}^2 \rangle}{2} \delta_{\mathbf{q}, \mathbf{k}+\mathbf{p}}) \\
& = -N \frac{\langle \mathbf{v}^2 \rangle^2}{4} \delta_{\mathbf{q}, \mathbf{k}+\mathbf{p}} (k S_k - q + p),
\end{aligned} \tag{5.107}$$

therefore

$$\frac{1}{i} \langle j_{\mathbf{q}}^{L*} | (i \mathcal{L} j_{\mathbf{k}}^L) j_{\mathbf{p}}^L \rangle = N \frac{\langle \mathbf{v}^2 \rangle^2}{4} \delta_{\mathbf{q}, \mathbf{k}+\mathbf{p}} (q - p). \tag{5.108}$$

With the same method

$$\frac{1}{i} \langle j_{\mathbf{q}}^{L*} | j_{\mathbf{k}}^L (i \mathcal{L} j_{\mathbf{p}}^L) \rangle = N \frac{\langle \mathbf{v}^2 \rangle^2}{4} \delta_{\mathbf{q}, \mathbf{k}+\mathbf{p}} (q - k). \tag{5.109}$$

We also know

$$-\frac{1}{NS_q} \langle j_{\mathbf{q}}^{L*} | \mathcal{L} \rho_{\mathbf{q}} \rangle \langle \rho_{\mathbf{q}}^* | j_{\mathbf{k}}^L j_{\mathbf{p}}^L \rangle = -Nq \frac{\langle \mathbf{v}^2 \rangle^2}{4} \delta_{\mathbf{q}, \mathbf{k}+\mathbf{p}}. \tag{5.110}$$

Replacing Eq. (5.108), (5.109) and (5.110) in Eq. (5.104) we get

$$\langle j_{\mathbf{q}}^{L*} | \mathcal{L} \mathcal{Q} j_{\mathbf{k}}^L j_{\mathbf{p}}^L \rangle = 0. \tag{5.111}$$

Which shows that M_{22}^3 , the projection of the kernel on the current-current pair, is also zero.

5.9. Integration Through Transients (ITT)

T. F. F. Farage *et al.* [57] have used ITT to calculate the structure factor of an active system using the Smoluchowski operator.

As we have mentioned before, the distribution function f following Eq. (5.27), is not a general solution of the Fokker-Planck equation (5.15). Replacing f in the Fokker-Planck equation would yield $\partial f / \partial t = \mathbf{\Lambda} f$ where $\mathbf{\Lambda}$ follows Eq. (5.33). The velocity dependent part of the f is the solution of the Fokker-Planck equation when the interaction forces are neglected or switched off. This means that the complete f , consisting of the velocity and the position dependent parts, is also a solution of the

Fokker-Planck equation with neglected interaction forces, $\mathbf{F}_i = 0$. We can assume that at $t < 0$ the interaction forces are switched off and at $t = 0$ we switch on the interaction forces \mathbf{F}_i , therefore

$$f(\mathbf{\Gamma}, t) = \begin{cases} f(\mathbf{\Gamma}), & t \leq 0 \\ e^{\Lambda t} f(\mathbf{\Gamma}), & t > 0. \end{cases} \quad (5.112)$$

We write [65]

$$e^{\Lambda t} = 1 + \int_0^t dt' e^{\Lambda t'} \Lambda. \quad (5.113)$$

Therefore when $t \rightarrow \infty$

$$\begin{aligned} \int d\mathbf{\Gamma} f(\mathbf{\Gamma}, t) \rho_{\mathbf{q}}^* \rho_{\mathbf{q}} &= \int d\mathbf{\Gamma} f(\mathbf{\Gamma}, 0) \rho_{\mathbf{q}}^* \rho_{\mathbf{q}} + \int d\mathbf{\Gamma} \int_0^\infty dt \rho_{\mathbf{q}}^* \rho_{\mathbf{q}} e^{\Lambda t} \Lambda f(\mathbf{\Gamma}, 0) \\ NS_q^s &= NS_q + \int_0^\infty dt \int d\mathbf{\Gamma} \Lambda f(\mathbf{\Gamma}, 0) e^{-\Lambda t} \rho_{\mathbf{q}}^* \rho_{\mathbf{q}}. \end{aligned} \quad (5.114)$$

Here S_q^s is the structure factor at the stationary state which is reached at $t \rightarrow \infty$. Since as we calculated, Λ is the actual time evolution operator for f , $-\Lambda$ is the time evolution operator for dynamic variables. Therefore $-\Lambda$ is equivalent to $i\mathcal{L}$. Thus

$$e^{-\Lambda t} \rho_{\mathbf{q}}^* \rho_{\mathbf{q}} = e^{i\mathcal{L}t} \rho_{\mathbf{q}}^* \rho_{\mathbf{q}}. \quad (5.115)$$

Using the projection operator $\mathcal{Q} = 1 - \sum_{\mathbf{q}} \rho_{\mathbf{q}} \langle \rho_{\mathbf{q}}^* | \dots \rangle / NS_q$, from Eq. (5.114) and (5.115) we get

$$NS_q^s = NS_q + \int_0^\infty dt \langle \Lambda \mathcal{Q} e^{i\mathcal{L}\mathcal{Q}t} \mathcal{Q} \rho_{\mathbf{q}}^* \rho_{\mathbf{q}} \rangle. \quad (5.116)$$

Here we use the mode coupling approximation to calculate

$$\begin{aligned} \langle \Lambda \mathcal{Q} \mathcal{P} e^{i\mathcal{L}t} \mathcal{P} \mathcal{Q} \rho_{\mathbf{q}}^* \rho_{\mathbf{q}} \rangle &= \\ \sum_{\mathbf{k} < \mathbf{p}} \frac{\langle \Lambda \mathcal{Q} | \rho_{\mathbf{k}} \rho_{\mathbf{p}} \rangle \langle \rho_{\mathbf{k}}^* \rho_{\mathbf{p}}^* | \exp(i\mathcal{L}t) \rho_{\mathbf{k}} \rho_{\mathbf{p}} \rangle \langle \rho_{\mathbf{k}}^* \rho_{\mathbf{p}}^* | \mathcal{Q} \rho_{\mathbf{q}}^* \rho_{\mathbf{q}} \rangle}{\langle \rho_{\mathbf{k}}^* \rho_{\mathbf{p}}^* | \rho_{\mathbf{k}} \rho_{\mathbf{p}} \rangle^2}. \end{aligned} \quad (5.117)$$

From Eq. (5.33) for one particle

$$\begin{aligned} \langle \Lambda \rangle &= \int d\mathbf{\Gamma} f(\mathbf{\Gamma}, 0) \Lambda = \left(3 \langle \mathbf{v}^2 \rangle - \frac{\xi^2}{\langle \mathbf{v}^2 \rangle} - \alpha \right) \\ &= \left(3 \langle \mathbf{v}^2 \rangle - \frac{2D_v}{\langle \mathbf{v}^2 \rangle} - \alpha \right) \end{aligned} \quad (5.118)$$

where $f(\mathbf{\Gamma}, 0)$ follows Eq. (5.27).

Also

$$\langle \Lambda \mathcal{Q} | \rho_{\mathbf{k}} \rho_{\mathbf{p}} \rangle = N \delta_{-\mathbf{k}, \mathbf{p}} \langle \Lambda \rangle S_k, \quad (5.119)$$

and

$$\begin{aligned} \langle \rho_{\mathbf{k}}^* \rho_{\mathbf{p}}^* | \mathcal{Q} \rho_{\mathbf{q}}^* \rho_{\mathbf{q}} \rangle &= \langle \rho_{\mathbf{k}}^* \rho_{\mathbf{p}}^* | \rho_{\mathbf{q}}^* \rho_{\mathbf{q}} \rangle - \sum_{\mathbf{q}} \frac{\langle \rho_{\mathbf{k}}^* \rho_{\mathbf{p}}^* | \rho_{\mathbf{q}} \rangle \langle \rho_{\mathbf{q}}^* | \rho_{\mathbf{q}}^* \rho_{\mathbf{q}} \rangle}{\langle \rho_{\mathbf{q}} | \rho_{\mathbf{q}}^* \rangle} \\ &= \delta_{-\mathbf{k}, \mathbf{p}} \delta_{\mathbf{q}, \mathbf{k} + \mathbf{p}} N^2 S_k S_q - \sum_{\mathbf{q}} \frac{N^2 \delta_{\mathbf{q}, \mathbf{k} + \mathbf{p}} \delta_{\mathbf{q}, \mathbf{q} + \mathbf{q}} S_k S_p S_q S_q^3}{N S_q} \\ &= \delta_{-\mathbf{k}, \mathbf{p}} \delta_{\mathbf{q}, \mathbf{k} + \mathbf{p}} N^2 S_k (1 - S_k). \end{aligned} \quad (5.120)$$

Substitution of Eq. (5.119) and (5.120) in (5.117) would result in

$$\langle \Lambda \mathcal{Q} \mathcal{P} e^{i\mathcal{L}t} \mathcal{P} \mathcal{Q} \rho_{\mathbf{q}}^* \rho_{\mathbf{q}} \rangle = \frac{1}{2} \langle \Lambda \rangle N (1 - S_k) \phi_k^2(t). \quad (5.121)$$

Therefore

$$S_q^s = S_q + \frac{1}{2} \langle \Lambda \rangle (1 - S_q) \int_0^\infty \phi_q^2(t) dt. \quad (5.122)$$

$$S_q^s = S_q + \frac{1}{2} \left(3 \langle \mathbf{v}^2 \rangle - \frac{2D_v}{\langle \mathbf{v}^2 \rangle} - \alpha \right) (1 - S_q) \int_0^\infty \phi_q^2(t) dt. \quad (5.123)$$

By substituting the correlation function $\phi_q(t)$, which is the solution of Eq. (5.87), in Eq. (5.123) we can calculate the S_q^s . The integral $\int_0^\infty \phi_q^2(t) dt$ becomes infinitely large at the glass transition, therefore Eq. (5.123) result in a reasonable S_q^s only when we are sufficiently away from the glass transition and inside the liquid state. The other necessity for Eq. (5.123) to result in a reasonable S_q^s is that the effective temperature should be sufficiently low.

For $\varepsilon = (\varphi_c - \varphi)/\varphi_c \simeq 0.0215$ and $\langle \mathbf{v}^2 \rangle = 2k_B T_{\text{Eff}} = 0.1$ we have solved Eq. (5.87) for three pairs of $(\alpha, D_v) = (0.08, 0.00284)$, $(0.05, 0.004881)$ and $(0.02, 0.06697)$. As we discussed in section 5.3.3, the higher the α (the smaller the D_v), the higher is the probability of finding active particles in the system. For solving Eq. (5.87) we use the Baus-Colot [41, 116] analytical expression for the structure factor S_q of the hard-sphere system in two dimensions. For every q value, replacing $\phi_q(t)$ in Eq. (5.123) and calculating the integral $\int_0^\infty \phi_q^2(t) dt$ results in the S_q^s . We show the S_q^s values around the first peak, in Fig. 5.11. The squares are the Baus-Colot S_q values. We can observe that with decreasing the α equivalent to decreasing the probability of finding active particles in the system, the peak value of the S_q^s decreases too. This is different from [57]. Here we model the activity with velocity dependent friction which is isotropic and does not have any rotational or directional dependence. But

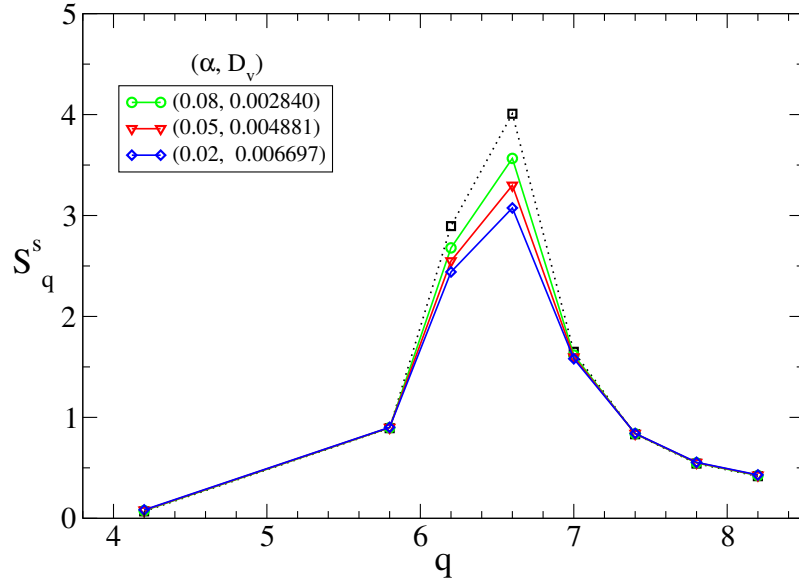


Figure 5.11.: The S_q^s values around the first peak, calculated via Eq. (5.123), for three pairs of (α, D_v) as indicated in the legends. The Baus-Colot equilibrium structure factor S_q is shown with squares. $\varepsilon = (\varphi_c - \varphi)/\varphi_c \simeq 0.0215$ and $\langle \mathbf{v}^2 \rangle = 2k_B T_{\text{Eff}} = 0.1$.

we are adding an additional constraint to the system; D_v related to the probability of finding active particles in the system. The higher is that probability (the smaller is the D_v), the more ordered the system becomes and the higher is the peak value of the structure factor. However in general the structure factors S_q^s are less pronounced than the equilibrium Baus-Colot structure factor.

Chapter 6

Summary and Conclusion

In this thesis we investigated the glass transition and dynamics of suspended charged particles. We started in chapter 2, with obtaining the mode coupling glass transition curve of a single and double Yukawa potential models in three dimensions. The glass transition curve follows the same qualitative behavior as the melting curve. The analytical formulas for both single and double Yukawa glass transition curves are discussed. The transition properties of a Yukawa potential system varies between two limits of the potential; one-component plasma and hard sphere. The nonergodicity parameter in the limit of one-component plasma (Coulombic potential) has a qualitatively different behavior compared to the hard sphere system in the small wave length regime. The nonergodicity parameter approaches zero with q^2 behavior, q being the wave number. We derived the asymptotic of the non-ergodicity parameters in vanishing wave number regime using the structure factor asymptotic and the mode coupling kernel relation.

In chapter 3, we looked at charged particles in two dimensional confinement. We investigated the glass transition of 2D monolayers with a Yukawa potential and another more realistic potential between dust particles in complex plasma derived by Kompaneets *et al.* [31]. Glass transition curves are obtained by a MCT-T/2-HNC approximation in a plane of screening parameter and coupling strength. While glass transition curves of Yukawa and Kompaneets monolayers are qualitatively the same, the transition temperature of the Kompaneets monolayer increases with increase of the collision parameter ζ . Both potentials reduce to a Coulombic potential in the limit of infinite λ_Y and λ_K , therefore all transition curves join at the same point in that limit. The Kompaneets transition curve is monotonous considering its three relevant parameter. However the transition curve can appear non-monotonous

corresponding to a fallacious re-entrant state sequence, if the pair interactions are misinterpreted as Yukawa interactions. We investigated the small wave number dependence of the nonergodicity parameters f_q of both Yukawa and Kompaneets potential. In the OCP limit the small wave number part of the f_q approaches zero with a linear behavior. When the screening parameter increases, the small wave number asymptotic of the f_q approaches a finite number.

A future generalization of the results, would be to investigate the binary mixtures. one could look at the case when one sort of particles are point like and the other sort have a finite diameter.

The long range potentials, such as the Coulomb potential, can suppress the structure factor asymptotic in the small wave number regime. In chapter 4, we have used this fact, for modifying the structure factor obtained from liquid state theory to create a jammed state structure factor. According to simulations, the jammed state structure factor has a linear behavior $S(k) \propto k$ at small k [46]. We added a long range potential of the form $1/r^2$ to the harmonic short range potential to introduce this linear behavior into the hypernetted chain structure factor. Without the long range potential, the structure factor has the behavior $S(k) \simeq S(0) + \alpha k^2$ which is different from the jammed state structure factor. We also used the random phase approximation to introduce the $1/r^2$ potential into the system as a perturbation for creating the linear behavior in the structure factor. The emergence of a $1/r^2$ potential can be rationalized if one assumes that perturbations are propagating with a spherical wave front $\propto r^2$ in a jammed state.

Since in complex plasma the dust particles can absorb some charges from the surrounding particles, the momentum transfer becomes unbalanced. This can lead to negative friction and active behavior in some regions of the phase space. In chapter 5, we start from a nonlinear Langevin equation which has a velocity dependent friction. The velocity dependent friction allows pumping of the energy into the system of Brownian particles in some regions of the phase space. We model the velocity dependence of the friction with a Rayleigh-type friction. The Rayleigh friction $\gamma(\mathbf{v}) = -\alpha + \mathbf{v}^2$, does not have any rotational dependence and only depends on the velocity magnitude. In this case the slow particles $v < \sqrt{\alpha}$ are accelerated (active), when faster particles $v > \sqrt{\alpha}$ are damped. Using the nonlinear Langevin equation the (Liouville) time evolution operators for the distribution function and the phase variables are calculated. The time evolution of the distribution function is a Fokker-Planck equation with a velocity dependent friction term. If the interaction

forces are negligible, the Fokker-Planck equation can be solved and the solution is non-Gaussian and only velocity dependent. Neglecting the hydrodynamic interactions, we assume that we can use the product of the Boltzmann position distribution and the velocity dependent part as the distribution function of our system. A two dimensional system is assumed, to explicitly calculate the velocity distribution. The Mori-Zwanzig formalism and the mode coupling approximation are used to obtain the equation of motion for the density auto-correlation function. The obtained memory kernel is the same as the memory kernel of the normal Brownian motion. Since the fluctuation-dissipation relation does not hold the relation between the effective temperature and the noise strength is nonlinear. We showed that for a constant effective temperature, the larger is the α (or the smaller is the noise strength), the probability of finding particles which are active increases. The MCT equation of the motion for the density auto-correlation functions for HSS in 2D is solved. Since the memory kernel does not change in the presented model, the activity does not effect the glass transition packing fraction. It can however shift the correlation function in the way that for a constant temperature and below the glass transition packing fraction, the higher is the probability of finding active particles in the system, the smaller is the time that the correlation function decays to zero. The relative time scales of the auto-correlation functions are calculated using the α -scaling.

We have estimated the distribution function of the system as a Boltzmann position distribution multiplied by the non-Gaussian velocity distribution resulted from non-interacting Fokker-Planck equation. Therefore, we use ITT to relate the structure factor in the interacting stationary state to the hard sphere structure factor in the state with our estimated distribution function. We find that since in our model introducing activity will put additional constraint on the system, with increasing the activity the height of structure factor peak increases.

A future investigation in this direction is to expand the results to the complex plasma by using a Yukawa potential interaction instead of hard sphere potential.

Appendix A

Derivation of the Yukawa Potential

The Poisson equation (in the SI units) for a test charge Q at the origin surrounded by plasma, can be written as

$$\nabla^2\phi(\mathbf{r}) = \frac{e}{\epsilon_0}(n_+(\mathbf{r}) - n_e(\mathbf{r})) + \frac{Q}{\epsilon_0}\delta(\mathbf{r}), \quad (\text{A.1})$$

where the n_+ and n_e are respectively the density of the ions and the electrons of the plasma. In the equilibrium condition ions and the electrons follow the Boltzmann distribution

$$\begin{aligned} n_+(\mathbf{r}) &= n_0 e^{e\phi(\mathbf{r})/k_B T_+} \\ n_e(\mathbf{r}) &= n_0 e^{-e\phi(\mathbf{r})/k_B T_e}, \end{aligned} \quad (\text{A.2})$$

where T_+ is the ion and T_e is the electron temperature. In the high temperature plasma it is possible to Taylor expand the distributions as

$$\begin{aligned} n_+(\mathbf{r}) &= n_0(1 + e\phi(\mathbf{r})/k_B T_+) \\ n_e(\mathbf{r}) &= n_0(1 - e\phi(\mathbf{r})/k_B T_e). \end{aligned} \quad (\text{A.3})$$

Replacing this in the Poisson equation results in

$$\nabla^2\phi(\mathbf{r}) = \frac{1}{\lambda^2}\phi(\mathbf{r}), \quad (\text{A.4})$$

where

$$\frac{1}{\lambda} = \sqrt{\frac{n_0 e^2}{k_B \epsilon_0} \left(\frac{1}{T_+} + \frac{1}{T_e} \right)}, \quad (\text{A.5})$$

for any position except the origin. Normally in the equilibrium situation $T_+ \ll T_e$, therefore $\lambda = \sqrt{\epsilon_0 k_B T_+ / (n_0 e^2)}$. Thus normally λ depends only on the ions

temperature. In three dimensions, Eq. (A.4) can be written as

$$\frac{1}{r^2} \frac{\partial}{\partial r} \left(r^2 \frac{\partial \phi}{\partial r} \right) = \frac{1}{\lambda^2} \phi. \quad (\text{A.6})$$

The function $\frac{\alpha}{r} \exp(-r/\lambda)$ where $r = |\mathbf{r}|$ is a solution of this equation. α should be determined from the boundary condition. Here when $r \rightarrow \infty$ the potential should be a Coulomb potential. Therefore $\alpha = Q/(4\pi\epsilon_0)$. This potential is called screened Coulomb or Yukawa potential

$$\phi(r) = \frac{Q}{4\pi\epsilon_0 r} \exp(-r/\lambda). \quad (\text{A.7})$$

A two dimensional Yukawa potential is derived from solving the Poisson equation in 3D and then considering a vanishing vertical distance from the 2D plane.

Appendix B

Fourier Transform Integral of $1/r^{n-\epsilon}$ in 3D

For calculating the integral in Eq. (4.5), we first start with

$$I = \int_0^\infty \frac{\sin r \exp(-\gamma r)}{r^{m-\epsilon}} dr = \text{Im} \int_0^\infty \exp((i - \gamma)r) r^{-m+\epsilon} dr. \quad (\text{B.1})$$

Taking $y = (\gamma - i)r$

$$I = \text{Im} \left((\gamma - i)^{m-\epsilon-1} \int_0^\infty \exp(-y) y^{-m+\epsilon} dy \right). \quad (\text{B.2})$$

Using $\Gamma(s) = \int_0^\infty \exp(-y)y^{s-1}dy$ and taking $\gamma = 0$

$$I = -\sin\left(\frac{m-1-\epsilon}{2}\pi\right)\Gamma(1-m+\epsilon). \quad (\text{B.3})$$

From Eq. (B.1) and Eq. (B.3) while taking $r = kx$ and $m = n - 1$

$$\int_0^\infty \frac{\sin(kx)}{x^{n-1-\epsilon}} dx = -\sin\left(\frac{n-2-\epsilon}{2}\pi\right)\Gamma(2-n+\epsilon)k^{n-2-\epsilon}. \quad (\text{B.4})$$

Appendix C

Normalization Constant and Different Moments of the Velocity Distribution

Here we calculate the Integrals in Eq. (5.21), (5.22), (5.23) and (5.24):

$$\begin{aligned}
\frac{1}{C} &= 2\pi \int_0^\infty e^{-\left(\frac{v^4}{4D_v} - \frac{\alpha v^2}{2D_v}\right)} v dv \\
&= 2\pi e^{\frac{\alpha^2}{4D_v}} \int_0^\infty e^{-\left(\frac{v^2}{2\sqrt{D_v}} - \frac{\alpha}{2\sqrt{D_v}}\right)^2} v dv \\
&= 2\pi \sqrt{D_v} e^{\frac{\alpha^2}{4D_v}} \int_{\frac{-\alpha}{2\sqrt{D_v}}}^\infty e^{-U^2} dU
\end{aligned} \tag{C.1}$$

where $U = \frac{v^2}{2\sqrt{D_v}} - \frac{\alpha}{2\sqrt{D_v}}$. Therefore

$$\begin{aligned}
\frac{1}{C} &= 2\pi \sqrt{D_v} e^{\frac{\alpha^2}{4D_v}} \left[\int_{\frac{-\alpha}{2\sqrt{D_v}}}^0 e^{-U^2} dU + \int_0^\infty e^{-U^2} dU \right] \\
&= \pi \sqrt{\pi D_v} \exp\left(\frac{\alpha^2}{4D_v}\right) \left[1 + \operatorname{erf}\left(\frac{\alpha}{2\sqrt{D_v}}\right) \right],
\end{aligned} \tag{C.2}$$

using the definition of the error function $\operatorname{erf}(x) = \frac{2}{\sqrt{\pi}} \int_0^x e^{-t^2} dt$ and the integral $\int_0^\infty e^{-t^2} dt = \sqrt{\pi}/2$. Also

$$\begin{aligned}
\langle \mathbf{v}^2 \rangle &= 2\pi C e^{\frac{\alpha^2}{4D_v}} \int_0^\infty e^{-\left(\frac{v^2}{2\sqrt{D_v}} - \frac{\alpha}{2\sqrt{D_v}}\right)^2} v^2 v dv \\
&= 2\pi \sqrt{D_v} e^{\frac{\alpha^2}{4D_v}} \int_{\frac{-\alpha}{2\sqrt{D_v}}}^\infty e^{-U^2} 2\sqrt{D_v} \left(U + \frac{\alpha}{2\sqrt{D_v}}\right) dU \\
&= 4\pi D_v e^{\frac{\alpha^2}{4D_v}} \left[\int_{\frac{-\alpha}{2\sqrt{D_v}}}^\infty \frac{\alpha}{2\sqrt{D_v}} e^{-U^2} dU + \int_{\frac{-\alpha}{2\sqrt{D_v}}}^\infty U e^{-U^2} dU \right].
\end{aligned} \tag{C.3}$$

the first integral is proportional to $1/C$ and the second integral can be calculated easily

$$\int_{\frac{-\alpha}{2\sqrt{D_v}}}^{\infty} U e^{-U^2} dU = \frac{1}{2} e^{\frac{-\alpha^2}{4D_v}}. \quad (\text{C.4})$$

Therefore

$$\langle \mathbf{v}^2 \rangle = \alpha + 2\sqrt{\frac{D_v}{\pi}} \exp\left(-\frac{\alpha^2}{4D_v}\right) \left[1 + \operatorname{erf}\left(\frac{\alpha}{2\sqrt{D_v}}\right)\right]^{-1} \quad (\text{C.5})$$

this is different from what Erdmann et al. [114] calculated by one minus in the power in the $\exp\left(-\frac{\alpha^2}{4D_v}\right)$. We go ahead and use the same method as [114, 117] to obtain $\langle \mathbf{v}^4 \rangle$. At the end we also calculate $\langle \mathbf{v}^6 \rangle$ which we need to use later.

$$\langle \mathbf{v}^4 \rangle = \frac{4D_v^2}{C^{-1}} \frac{\partial^2}{\partial \alpha^2} (C^{-1}) \quad (\text{C.6})$$

where C^{-1} follows Eq. (C.2). And

$$\langle \mathbf{v}^6 \rangle = \frac{8D_v^3}{C^{-1}} \frac{\partial^3}{\partial \alpha^3} (C^{-1}). \quad (\text{C.7})$$

So

$$\langle \mathbf{v}^4 \rangle = 2D_v + \alpha \langle \mathbf{v}^2 \rangle, \quad (\text{C.8})$$

and

$$\langle \mathbf{v}^6 \rangle = 2\alpha D_v + (\alpha^2 + 4D_v) \langle \mathbf{v}^2 \rangle. \quad (\text{C.9})$$

Appendix D

Ω_{22} for Normal Brownian Motion

Here we calculate Ω_{22} for normal Brownian motion to compare with Brownian motion with velocity dependent friction. For normal Brownian motion following the linear Langevin Eq. (5.1), the time evolution operator is written as

$$\begin{aligned}
 i\mathcal{L} = \dot{\Gamma} \cdot \frac{\partial}{\partial \Gamma} &= \sum_i \left(\mathbf{v}_i \cdot \frac{\partial}{\partial \mathbf{r}_i} + \mathbf{F}_i \cdot \frac{\partial}{\partial \mathbf{v}_i} \right) \\
 &+ \sum_i \left(-\frac{1}{2} \xi^2 \frac{\partial^2}{\partial \mathbf{v}_i^2} - \gamma_0 \mathbf{v}_i \cdot \frac{\partial}{\partial \mathbf{v}_i} \right).
 \end{aligned} \tag{D.1}$$

Therefore

$$\begin{aligned}
 \Omega_{22} &= \frac{1}{iNk_B T} \langle j_{\mathbf{q}}^{L*} | i\mathcal{L} j_{\mathbf{q}}^L \rangle \\
 &= \frac{1}{iNk_B T} \int d\Gamma f \sum_k v_k^L \exp(-i\mathbf{q} \cdot \mathbf{r}_k) \left(-\sum_i \gamma_0 \mathbf{v}_i \cdot \frac{\partial}{\partial \mathbf{v}_i} \right. \\
 &\quad \left. + \sum_i \mathbf{F}_i \cdot \frac{\partial}{\partial \mathbf{v}_i} \right) \sum_{k'} v_{k'}^L \exp(i\mathbf{q} \cdot \mathbf{r}_{k'}) \\
 &= i\gamma_0 + \frac{1}{ik_B T} \int d\Gamma f \sum_k v_k^L F_k^L,
 \end{aligned} \tag{D.2}$$

where the distribution function follows Eq. (5.16). Eq. (5.31) in case of linear Langevin equation can be written as

$$\sum_i \mathbf{F}_i \cdot \mathbf{v}_i = \sum_i \gamma_0 \mathbf{v}_i^2 - \sum_i \frac{\xi^2}{2} = 0, \tag{D.3}$$

since the fluctuation-dissipation relation, $\xi^2 = 2k_B T \gamma_0$, is valid for normal Brownian motion. Replacing this in Eq. (D.2) one has

$$\Omega_{22} = i\gamma_0 \tag{D.4}$$

This is consistent with what is calculated in [118].

Appendix E

Mori-Zwanzig Formalism

Here we derive Eq. (5.53) following the procedure in [119] but using the Laplace transform

$$f(z) = i \int_0^{\infty} e^{izt} \varphi(t) dt \quad t > 0, \quad \text{Re}(z) < 0, \quad \text{Im}(z) > 0. \quad (\text{E.1})$$

For a phase variable $A(\Gamma(t)) \equiv A(t)$ one can write Eq. (5.5)

$$\frac{dA(t)}{dt} = i\mathcal{L}A(t), \quad (\text{E.2})$$

taking the Laplace transform from both side of the equation would give

$$i \int_0^{\infty} e^{izt} \frac{dA(t)}{dt} dt = -\mathcal{L} \int_0^{\infty} A(t) e^{izt} dt \quad (\text{E.3})$$

where

$$i \int_0^{\infty} e^{izt} \frac{dA(t)}{dt} dt = -iA(0) + Z \int_0^{\infty} e^{izt} A(t) dt. \quad (\text{E.4})$$

This would leads to

$$z\tilde{A}(z) + \mathcal{L}\tilde{A}(z) = -A. \quad (\text{E.5})$$

Multiplying Eq. (E.5) from right with projector operator \mathcal{P} and using $\mathcal{Q}^2 = \mathcal{Q}$, $\mathcal{P}^2 = \mathcal{P}$ and $\mathcal{Q} + \mathcal{P} = 1$ leads to

$$z\mathcal{P}\tilde{A}(z) + \mathcal{P}\mathcal{L}\mathcal{P}\tilde{A}(z) + \mathcal{P}\mathcal{L}\mathcal{Q}\mathcal{Q}\tilde{A}(z) = -A. \quad (\text{E.6})$$

Also multiplying Eq. (E.5) from right with \mathcal{Q} ends with

$$z\mathcal{Q}\tilde{A}(z) + \mathcal{Q}\mathcal{L}\mathcal{Q}\tilde{A}(z) + \mathcal{Q}\mathcal{L}\mathcal{P}\tilde{A}(z) = 0. \quad (\text{E.7})$$

Replacing $\mathcal{Q}\tilde{A}(z)$ from Eq. (E.7) into Eq. (E.6), we have

$$(z + \mathcal{P}\mathcal{L}\mathcal{P} - \mathcal{P}\mathcal{L}\mathcal{Q}(z + \mathcal{Q}\mathcal{L}\mathcal{Q})^{-1}\mathcal{Q}\mathcal{L}\mathcal{P})\mathcal{P}\tilde{A}(z) = -A. \quad (\text{E.8})$$

Thus for every matrix element A_n

$$(z + \mathcal{P}\mathcal{L}\mathcal{P} - \mathcal{P}\mathcal{L}\mathcal{Q}(z + \mathcal{Q}\mathcal{L}\mathcal{Q})^{-1}\mathcal{Q}\mathcal{L}\mathcal{P})\mathcal{P}\tilde{A}_n(z) = -A_n. \quad (\text{E.9})$$

Assuming $\mathcal{P} = \sum_m A_m \langle A_m^* | \dots \rangle$ where $\langle A_m^* | A_m \rangle = 1$, Eq. (E.9) can be written as

$$\begin{aligned} \sum_m z \langle A_m^* | \tilde{A}_n(z) \rangle A_m + \sum_{m,l} \langle A_m^* | \mathcal{L}A_l \rangle \langle A_l^* | \tilde{A}_n(z) \rangle A_m \\ - \sum_{m,l} \langle A_m^* | \mathcal{L}\mathcal{Q}(z + \mathcal{Q}\mathcal{L}\mathcal{Q})^{-1}\mathcal{Q}\mathcal{L}A_l \rangle \langle A_l^* | \tilde{A}_n(z) \rangle A_m = -A_n. \end{aligned} \quad (\text{E.10})$$

Therefore

$$\begin{aligned} \sum_m z \delta_{k,m} \langle A_m^* | \tilde{A}_n(z) \rangle + \sum_l \langle A_k^* | \mathcal{L}A_l \rangle \langle A_l^* | \tilde{A}_n(z) \rangle \\ - \sum_l \langle A_k^* | \mathcal{L}\mathcal{Q}(z + \mathcal{Q}\mathcal{L}\mathcal{Q})^{-1}\mathcal{Q}\mathcal{L}A_l \rangle \langle A_l^* | \tilde{A}_n(z) \rangle = -\delta_{k,n}, \end{aligned} \quad (\text{E.11})$$

or

$$\begin{aligned} \sum_l z \delta_{k,l} \langle A_l^* | \tilde{A}_n(z) \rangle + \sum_l \langle A_k^* | \mathcal{L}A_l \rangle \langle A_l^* | \tilde{A}_n(z) \rangle \\ - \sum_l \langle A_k^* | \mathcal{L}\mathcal{Q}(z + \mathcal{Q}\mathcal{L}\mathcal{Q})^{-1}\mathcal{Q}\mathcal{L}A_l \rangle \langle A_l^* | \tilde{A}_n(z) \rangle = -\delta_{k,n}. \end{aligned} \quad (\text{E.12})$$

which is called Mori-Zwanzig equation of motion. The matrix form of Eq. (E.12) is written as

$$(z\mathbf{I} + \mathbf{\Omega} - \mathbf{M})\mathbf{Y}(z) = -\mathbf{I}. \quad (\text{E.13})$$

where

$$Y_{nm}(z) = \langle A_n^* | \tilde{A}_m(z) \rangle, \quad (\text{E.14})$$

$$\Omega_{nm} = \langle A_n^* | \mathcal{L}A_m \rangle, \quad (\text{E.15})$$

and

$$M_{nm} = \langle A_n^* | \mathcal{L}\mathcal{Q}(z + \mathcal{Q}\mathcal{L}\mathcal{Q})^{-1}\mathcal{Q}\mathcal{L}A_m \rangle. \quad (\text{E.16})$$

Bibliography

- [1] D. Turnbull, *Contemp. Phys.* **10**, 473 (1969).
- [2] R. Brüning and K. Samwer, *Phys. Rev. B* **46**, 11318 (1992).
- [3] P. G. Debenedetti and F. H. Stillinger, *Nature* **410**, 259 (2001).
- [4] F. H. Stillinger and T. A. Weber, *Science* **225**, 983 (1983).
- [5] U. Bengtzelius, W. Götze, and A. Sjölander, *J. Phys. C* **17**, 5915 (1984).
- [6] W. Götze, *Complex Dynamics of Glass-Forming Liquids: A Mode-Coupling Theory* (Oxford University Press, Oxford, 2009).
- [7] Y. Singh, J. P. Stoessel, and P. G. Wolynes, *Phys. Rev. Lett.* **54**, 1059 (1985).
- [8] T. R. Kirkpatrick and P. G. Wolynes, *Phys. Rev. A* **35**, 3072 (1987).
- [9] K. Ngai, *J. Non-Cryst. Solids* **275**, 7 (2000).
- [10] A. Cavagna, *Phys. Rep.* **476**, 51 (2009).
- [11] G. Tarjus, arXiv:1010.2938 [cond-mat.stat-mech] (2010).
- [12] W. Kob and H. C. Andersen, *Phys. Rev. E* **51**, 4626 (1995).
- [13] W. Kob, *J. Phys.: Condens. Matter* **11**, R85 (1999).
- [14] W. Götze, *J. Phys.: Condens. Matter* **11**, A1 (1999).
- [15] A. Ivlev, H. Löwen, G. Morfill, and C. P. Royall, *Complex Plasmas and Colloidal Dispersions: Particle-Resolved Studies of Classical Liquids and Solids* (World Scientific, Singapore, 2012).
- [16] E. Allahyarov and H. Löwen, *J. Phys.: Condens. Matter* **13**, L277 (2001).

-
- [17] J.-P. Hansen and I. R. McDonald, *Theory of Simple Liquids* (Academic Press, London, 1986), 3rd ed.
- [18] H. Löwen, Phys. Rep. **237**, 249 (1994).
- [19] M. Heinen, P. Holmqvist, A. J. Banchio, and G. Nägele, J. Chem. Phys. **134**, 044532 (2011).
- [20] J. Thakur and J. Bosse, J. Non-Cryst. Solids **117**, 898 (1990).
- [21] J. Bosse and S. D. Wilke, Phys. Rev. Lett. **80**, 1260 (1998).
- [22] J. Bosse and K. Kubo, Phys. Rev. A **18**, 2337 (1978).
- [23] S. D. Wilke and J. Bosse, Phys. Rev. E **59**, 1968 (1999).
- [24] G. Szamel and H. Löwen, Phys. Rev. A **44**, 8215 (1991).
- [25] P. Pieranski, L. Strzelecki, and B. Pansu, Phys. Rev. Lett. **50**, 900 (1983).
- [26] E. Chang and D. W. Hone, Europhys. Lett. **5**, 635 (1988).
- [27] H. Thomas, G. E. Morfill, V. Demmel, J. Goree, B. Feuerbacher, and D. Möhlmann, Phys. Rev. Lett. **73**, 652 (1994).
- [28] V. Fortov, A. Ivlev, S. Khrapak, A. Khrapak, and G. Morfill, Phys. Rep. **421**, 1 (2005).
- [29] V. E. Fortov and G. E. Morfill, *Complex and dusty plasmas: from laboratory to space* (CRC Press, Boca Raton, 2010).
- [30] U. Konopka, G. E. Morfill, and L. Ratke, Phys. Rev. Lett. **84**, 891 (2000).
- [31] R. Kompaneets, U. Konopka, A. V. Ivlev, V. Tsytovich, and G. Morfill, Phys. Plasmas **14**, 052108 (2007).
- [32] S. V. Vladimirov and M. Nambu, Phys. Rev. E **52**, R2172 (1995).
- [33] S. V. Vladimirov and O. Ishihara, Phys. Plasmas **3**, 444 (1996).
- [34] O. Ishihara and S. V. Vladimirov, Phys. Plasmas **4**, 69 (1997).
- [35] B. S. Xie, K. F. He, and Z. Q. Huang, Phys. Lett. A **253**, 83 (1999).
- [36] D. S. Lemons, M. S. Murillo, W. Daughton, and D. Winske, Phys. Plasmas **7**, 2306 (2000).

-
- [37] G. Lapenta, Phys. Rev. E **62**, 1175 (2000).
- [38] V. A. Schweigert, Plasma Phys. Rep. **27**, 997 (2001).
- [39] R. Kompaneets, S. V. Vladimirov, A. V. Ivlev, and G. E. Morfill, New J. Phys. **10**, 063018 (2008).
- [40] T. B. Röcker, A. V. Ivlev, R. Kompaneets, and G. E. Morfill, Phys. Plasmas **19**, 033708 (2012).
- [41] M. Bayer, J. M. Brader, F. Ebert, M. Fuchs, E. Lange, G. Maret, R. Schilling, M. Sperl, and J. P. Wittmer, Phys. Rev. E **76**, 011508 (2007).
- [42] S. Lang, R. Schilling, and T. Franosch, Phys. Rev. E **90**, 062126 (2014).
- [43] S. Lang, T. Franosch, and R. Schilling, J. Chem. Phys. **140**, 104506 (2014).
- [44] T. Franosch, S. Lang, and R. Schilling, Phys. Rev. Lett. **109**, 240601 (2012).
- [45] A. Donev, F. H. Stillinger, and S. Torquato, Phys. Rev. Lett. **95**, 090604 (2005).
- [46] L. E. Silbert and M. Silbert, Phys. Rev. E **80**, 041304 (2009).
- [47] S. Torquato and F. H. Stillinger, Phys. Rev. E **68**, 041113 (2003).
- [48] A. B. Hopkins, F. H. Stillinger, and S. Torquato, Phys. Rev. E **86**, 021505 (2012).
- [49] J. H. Nixon and M. Silbert, J. Phys. C **15**, L165 (1982).
- [50] R. Kubo, Rep. Prog. Phys. **29**, 255 (1966).
- [51] J. K. G. Dhont, *An Introduction to Dynamics of Colloids* (Elsevier Science, Amsterdam, 1996).
- [52] J. Dunkel, W. Ebeling, and S. A. Trigger, Phys. Rev. E **70**, 046406 (2004).
- [53] J. Bialké, T. Speck, and H. Löwen, Phys. Rev. Lett. **108**, 168301 (2012).
- [54] R. Ni, M. A. C. Stuart, and M. Dijkstra, Nature Communications **4**, 2704 (2013).
- [55] P. Romanczuk, M. Bär, W. Ebeling, B. Lindner, and L. Schimansky-Geier, Eur. Phys. J. Special Topics **202**, 1 (2012).

-
- [56] L. Berthier and J. Kurchan, *Nat. Phys.* **9**, 310 (2013).
- [57] T. F. F. Farage and J. M. Brader, arXiv:1403.0928 [cond-mat.soft] (2014).
- [58] G. Szamel, E. Flenner, and L. Berthier, arXiv:1501.01333 [cond-mat.soft] (2015).
- [59] D. J. Evans and G. P. Morriss, *Statistical Mechanics of Nonequilibrium Liquids* (Academic Press, London, 1991), 1st ed.
- [60] H. Mori, *Prog. Theor. Phys.* **33**, 423 (1965).
- [61] R. Zwanzig, *J. Chem. Phys.* **33**, 1338 (1960).
- [62] M. Fuchs, *Structural relaxation in simple liquids* (PhD Thesis, TU München, 1993).
- [63] T. Gleim, W. Kob, and K. Binder, *Phys. Rev. Lett.* **81**, 4404 (1998).
- [64] M. Fuchs and M. E. Cates, *Phys. Rev. Lett.* **89**, 248304 (2002).
- [65] M. Fuchs and M. E. Cates, *J. Rheol.* **53**, 957 (2009).
- [66] S.-H. Chong and B. Kim, *Phys. Rev. E* **79**, 021203 (2009).
- [67] K. Suzuki and H. Hayakawa, *Phys. Rev. E* **87**, 012304 (2013).
- [68] W. T. Kranz, M. Sperl, and A. Zippelius, *Phys. Rev. Lett.* **104**, 225701 (2010).
- [69] W. T. Kranz, M. Sperl, and A. Zippelius, *Phys. Rev. E* **87**, 022207 (2013).
- [70] A. Yazdi, A. Ivlev, S. Khrapak, H. Thomas, G. E. Morfill, H. Löwen, A. Wysocki, and M. Sperl, *Phys. Rev. E* **89**, 063105 (2014).
- [71] P. Debye and E. Hückel, *Physikalische Zeitschrift* **24**, 185 (1923).
- [72] F. Melandsø, *Phys. Plasmas* **3**, 3890 (1996).
- [73] S. A. Khrapak, A. V. Ivlev, and G. E. Morfill, *Phys. Plasmas* **17**, 042107 (2010).
- [74] H. Ikezi, *Phys. Fluids* **29**, 1764 (1986).
- [75] F. Bitzer, T. Palberg, H. Löwen, R. Simon, and P. Leiderer, *Phys. Rev. E* **50**, 2821 (1994).
- [76] C. Beck, W. Härtl, and R. Hempelmann, *J. Chem. Phys.* **111**, 8209 (1999).

-
- [77] M. Heinen, A. J. Banchio, and G. Nägele, *J. Chem. Phys.* **135**, 154504 (2011).
- [78] T. Franosch, M. Fuchs, W. Götze, M. R. Mayr, and A. P. Singh, *Phys. Rev. E* **55**, 7153 (1997).
- [79] M. Sperl, *Glass Transition in Colloids with Attractive Interactions* (Diploma thesis, TU München, 2000).
- [80] M. Fuchs, W. Götze, and M. R. Mayr, *Phys. Rev. E* **58**, 3384 (1998).
- [81] K. Ng, *J. Chem. Phys.* **61**, 2680 (1974).
- [82] F. Lado, *J. Comput. Phys.* **8**, 417 (1971).
- [83] J. K. Percus and G. J. Yevick, *Phys. Rev.* **110**, 1 (1958).
- [84] O. S. Vaulina and S. A. Khrapak, *JETP* **90**, 287 (2000).
- [85] O. Vaulina, S. Khrapak, and G. Morfill, *Phys. Rev. E* **66**, 016404 (2002).
- [86] S. Hamaguchi, R. T. Farouki, and D. H. E. Dubin, *Phys. Rev. E* **56**, 4671 (1997).
- [87] F. A. Lindemann, *Phys. Z.* **11**, 609 (1910).
- [88] G. Nägele, *The Physics of Colloidal Soft Matter: Lecture Notes 14* (Institute of Fundamental Technical Research, Warsaw, 2004).
- [89] S. A. Khrapak, M. Chaudhuri, and G. E. Morfill, *J. Chem. Phys.* **134**, 241101 (2011).
- [90] M. Sperl, *Phys. Rev. E* **71**, 060401 (2005).
- [91] W. van Megen, *Transp. Theory Stat. Phys.* **24**, 1017 (1995).
- [92] M. Baus and J. P. Hansen, *Phys. Rep.* **59**, 1 (1980).
- [93] *From discussion with A. Ivlev.*
- [94] A. V. Filippov, A. G. Zagorodny, A. F. Pal', and A. N. Starostin, *JETP Lett.* **81**, 146 (2005).
- [95] M. Chaudhuri, S. A. Khrapak, and G. E. Morfill, *Phys. Plasmas* **15**, 053703 (2008).

- [96] A. Yazdi, M. Heinen, A. Ivlev, H. Löwen, and M. Sperl, *Phys. Rev. E* **91**, 052301 (2015).
- [97] M. Heinen, E. Allahyarov, and H. Löwen, *J. Comput. Chem.* **35**, 275 (2014).
- [98] H. Totsuji, T. Kishimoto, and C. Totsuji, *Phys. Rev. Lett.* **78**, 3113 (1997).
- [99] R. V. Kennedy and J. E. Allen, *J. Plasma Phys.* **69**, 485 (2003).
- [100] H. Löwen, *J. Phys.: Condens. Matter* **4**, 10105 (1992).
- [101] A. Barreira Fontecha, H. J. Schöpe, H. König, T. Palberg, R. Messina, and H. Löwen, *J. Phys.: Condens. Matter* **17**, S2779 (2005).
- [102] V. E. Fortov, A. G. Khrapak, S. A. Khrapak, V. I. Molotkov, and O. F. Petrov, *Phys. Usp.* **47**, 447 (2004).
- [103] L. Chen, A. B. Landon, and M. A. Lieberman, *J. Plasma Phys.* **9**, 311 (1973).
- [104] P. C. Stangeby and J. E. Allen, *J. Plasma Phys.* **6**, 19 (1971).
- [105] G. B. Arfken and H. J. Weber, *Mathematical Methods for Physicists* (Elsevier Academic Press, New York, 2005).
- [106] D. Hajnal, M. Oettel, and R. Schilling, *J. Non-Cryst. Solids* **357**, 302 (2011).
- [107] P. Hartmann, G. J. Kalman, Z. Donkó, and K. Kutasi, *Phys. Rev. E* **72**, 026409 (2005).
- [108] R. J. F. Leote de Carvalho, R. Evans, and Y. Rosenfeld, *Phys. Rev. E* **59**, 1435 (1999).
- [109] J. L. Barrat and J. P. Hansen, *Basic Concepts for Simple and Complex Liquids* (Cambridge University Press, Cambridge, 2003).
- [110] W. H. Press, S. A. Teukolsky, W. T. Vetterling, and B. P. Flannery, *Numerical Recipes in C: The Art of Scientific Computing* (Cambridge University Press, New York, 1992), 2nd ed.
- [111] G. E. Uhlenbeck and L. S. Ornstein, *Phys. Rev.* **36**, 823 (1930).
- [112] R. Kubo, M. Toda, and N. Hashitsume, *Statistical Physics II - Nonequilibrium Statistical Mechanics* (Springer, Heidelberg, 1991), 2nd ed.

-
- [113] J. W. S. Rayleigh, *The Theory of Sound*, vol. I (Dover, New York, 1945), 2nd ed.
- [114] U. Erdmann, W. Ebeling, L. Schimansky-Geier, and F. Schweitzer, *Eur. Phys. J. B* **15**, 105 (2000).
- [115] I. Gazuz and M. Fuchs, *Phys. Rev. E* **87**, 032304 (2013).
- [116] M. Baus and J.-L. Colot, *J. Phys. C: Solid state Phys.* **19**, L643 (1986).
- [117] R. L. Stratonovich, *Topics in the Theory of Random Noise*, vol. II (Gordon and Breach, London, 1967).
- [118] W. Hess and R. Klein, *Adv. Phys.* **32**, 173 (1983).
- [119] H. Hayakawa and M. Otsuki, *Prog. Theor. Phys.* **119**, 381 (2008).

Acknowledgment

I want to thank PD Dr. Alexei Ivlev and Prof. Dr. Hartmut Löwen for their great supervision and interesting discussions which brought me many new ideas.

I thank Dr. Matthias Sperl for many interesting scientific discussions, and for answering my questions. He guided me through my thesis and gave me many helpful suggestions.

I thank Dr. Marco Heinen for supporting me with his structure factor program and helping me with many technical or scientific problems. He also kindly answered some of my questions. I also thank Dr. Adam Wysocki for letting me use his structure factor code. I thank Prof. Dr. Leonardo E. Silbert for introducing me to a new scientific problem, and initiating many interesting discussions which later helped me during writing my thesis.

I thank Dr. Peidong Yu, Dr. Philip Born, Dr. Stefan Frank-Richter, Dr. Hideyuki Mizuno, Ting Wang, Sebastian Pitikaris, Alexandre Meurisse, Jan Haeberle and Steffen Reinhold for creating a good atmosphere with interesting discussions during lunch breaks and Dr. Madhu Priya for accompanying me during tea breaks with some nice scientific discussions.

Finally I want to thank my husband, for proof reading some parts of my thesis and helping me with some technical problems, and more importantly, for being there for me. I thank my family which, although being far away, they have been near all along. I also thank my friends and my husband's family for their moral support.

Eidesstattliche Versicherung

Ich versichere an Eides Statt, dass die Dissertation von mir selbständig und ohne unzulässige fremde Hilfe unter Beachtung der Grundsätze zur Sicherung guter wissenschaftlicher Praxis an der Heinrich-Heine-Universität Düsseldorf erstellt worden ist.

Düsseldorf, den 11.08.2015

Anoosheh Yazdi